ENHANCED ACTIVE COOLING OF HIGH POWER LED LIGHT SOURCES BY UTILIZING SHROUDS AND RADIAL FINS

A Thesis
Presented to
The Academic Faculty

by

Mark Gleva

In Partial Fulfillment
of the Requirements for the Degree
Masters of Science in Mechanical Engineering
George W. Woodruff School of Mechanical Engineering

Georgia Institute of Technology
August, 2009

ENHANCED ACTIVE COOLING OF HIGH POWER LED LIGHT SOURCES BY UTILIZING SHROUDS AND RADIAL FINS

Approved by:

Dr. Samuel Graham, Advisor
School of Mechanical Engineering
Georgia Institute of Technology

Dr. Yogendra Joshi
School of Mechanical Engineering
Georgia Institute of Technology

Dr. Satish Kumar
School of Mechanical Engineering
Georgia Institute of Technology

Date Approved: May 4, 2009

ACKNOWLEDGEMENTS

I am extremely grateful to everyone who has had a role in my education, although I would like to specifically thank Dr. Samuel Graham for being a wonderful adviser. His patience, insight, availability, and flexibility have all been crucial to my success and enjoyment at Georgia Tech. His guidance has played a major role in strengthening my engineering skill set and enhancing my confidence.

I am also thankful for the other faculty members that have been involved with my research efforts. During my first year, I was very fortunate to be provided with the expertise of Dr. Yogendra Joshi, Dr. Andrei Fedorov, Dr. Marc Weissburg, and Dr. Jeannette Yen. The productive results of our initial efforts on biomimetic heat transfer are ascribed to their contributions in our meetings. I also appreciate the counseling and time provided by my committee members, Dr. Yogendra Joshi and Dr. Satish Kumar.

The graduate students in my research group have been wonderful coworkers and an outstanding support network. I cherish my friendships with them and am obliged for the academic, societal, political, and personal enlightenment they have provided. Adam Christensen has been an outstanding mentor who is destined to be an excellent professor. Roderick Jackson and Thomas Beechem have been extraordinary office-mates. The other members of my terrific research group include Abe Greenstein, Minseok Ha, Robert Cross, Namsu Kim, Prem Nagarathnam, Sukwon Choi, Yongjin Kim, Fernando Reiter, Steven Walker, Ashante Petty, James Ford, and Yeny Hudiono.

Finally I would like to thank my entire family, but especially my parents for raising me well. All of my relatives have been very supportive, caring, and interested in my pursuits. I am thoroughly grateful for the wonderful family and friends in my life.

TABLE OF CONTENTS

Page

LIST OF TABLES

LIST OF FIGURES

SUMMARY

Technological developments in the area of high power LED light sources have enabled their utilization in general illumination applications. Along with this advancement comes the need for progressive thermal management strategies in order to ensure device performance and reliability.

Minimizing an LED’s junction temperature is done by minimizing the total system’s thermal resistance. For actively cooled systems, this may essentially be achieved by simultaneously engineering the conduction through the heat sink and creating a well-designed flow pattern over suitable convective surface area. While such systems are routinely used in cooling microelectronics, their use in LED lighting systems encounter additional constraints which must be accounted for in the design of the cooling system. These are typically driven by the size, shape, and building codes involved with the lighting industry, and thus influence the design of drop-in replacement LED fixtures. Employing LED systems for customary down-lighting applications may require shrouded radial fin heat sinks to increase the heat transfer while reducing the space requirement for active cooling.

Most lighting is already in some form of housing, and the ability to concurrently optimize these housings for thermal and optical performance could accelerate the widespread implementation of cost-efficient, environmentally-friendly solid-state lighting. In response, this research investigated the use of conical, cylindrical, square, and pyramidal shrouds with pin/radial fin heat sink designs for the thermal management of high power LED sources. Numerical simulations using FLUENT were executed in order to account for details of the air flow, pressure drop, and pumping power, as well as the heat transfer and temperature distributions throughout the system. The LEDs were modeled as a distributed heat source of 25 – 75 W on a central portion of the various heat sinks. Combinations of device junction temperature and pumping power were used to assess the performance of shrouded heat sink designs for their use in air-cooled, down-lighting LED fixtures.

In general, circular heat sinks with conical/cylindrical shrouds outperformed square heat sinks with pyramidal/square shrouds, despite the circular sinks having only 86.7% of the square sink's surface area. For a pumping power of 5 W and an ambient temperature of 300 K, the transition to pin fin circular sinks reduced the best-shroud-case thermal resistance from 0.40 K/W to 0.35 K/W. The best-case shroud inclination angle went from 71.8° to 65.3° during this transition.

While maintaining the same surface area as the pin fin circular sink, a circular sink with only straight radial fins was created. Its thermal resistance for the same pumping power and ambient temperature as above was 0.32 K/W. Likewise, a hybrid sink with both pin fins and straight radial fins had a thermal resistance of 0.33 K/W for those conditions. The best-case shroud geometries for these two cases were cylindrical. Along with the slightly lower thermal resistance, the 'straight radial fin only' configurations would be preferable to the hybrid fin configurations because of manufacturing considerations and compactness. By increasing the surface area, straight radial fin aluminum heat sinks in cylindrical shrouds were shown to be capable of thermal resistances as low as 0.19 K/W for the established conditions.

CHAPTER 1

INTRODUCTION

1.1 Motivation for Research

1.1.1 Conservation and Reduction of Electrical Energy Usage

Projections of the future demands for energy have become a vital concern for scientists, engineers, and our society in general. While it is not clear how good these projections are, most state that the global energy demand will rise from 14 TW in 2003 to about 30 TW in 2050. As shown in Figure 1, approximately 10 TW of new energy sources will be needed to meet the global energy demand by 2050 [1, 2]. It is expected that these new sources of energy will have to come from renewables, which at present are not ready to contribute to the growing energy demand on such a large scale.

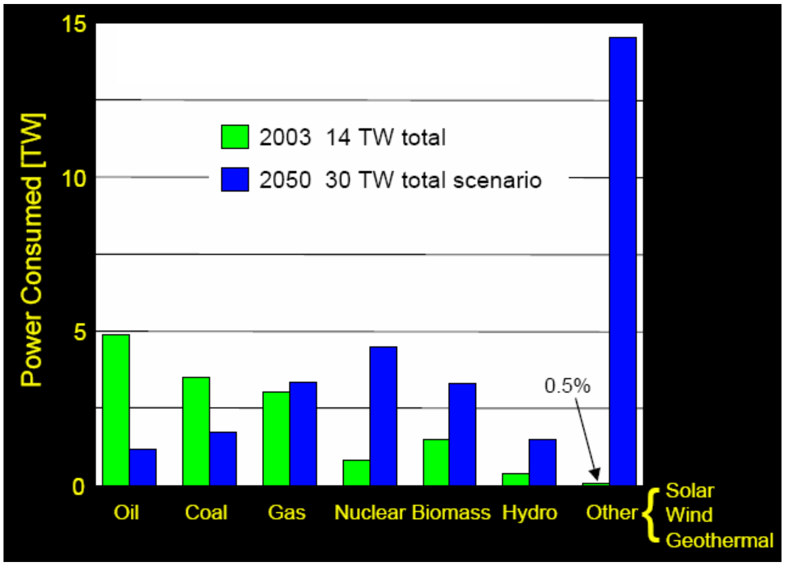

Figure 1. Global rate of primary energy consumption [3].

Estimates indicate that solar photovoltaics with an 8% conversion efficiency could provide as much as 18 TW of power while covering only 0.25% of the earth's surface [4]. However, this technology is not yet viable because of high costs. While there is much on-going research to make technologies like solar photovoltaics, wind energy, and solar thermal viable on a grid parity basis ($0.10/kWh), calls for energy efficiency will also be necessary to curb the future energy demand. This latter effort includes improving the efficiencies of electrical devices.

Approximately 20% of the world's electricity is used for lighting and annually accounts for over 1.5 trillion tons of carbon dioxide [5]. As Figure 2 shows, around 30% of the electricity in the United States is used for lighting [6]. Conventional lighting methodologies provide significant opportunities to improve illumination efficacy. For example, using a coal power plant to energize residential incandescent lighting is only about 3% efficient. This small efficiency reflects the limitations of incandescent bulbs much more so than those of coal power [7]. By increasing the efficiency of just the illumination devices as anticipated by the U. S. Department of Energy, a $20 billion annual energy savings could be realized in the U. S. by 2025 [8].

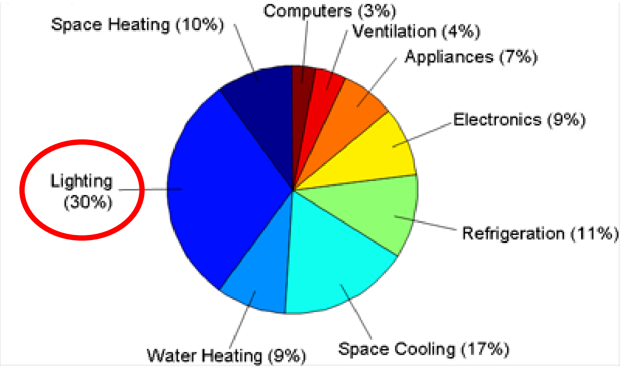

Figure 2. U.S. electricity consumption distribution [6].

Public policy has recently begun to play a crucial role in the lighting industry. The United States' Congress passed an energy bill that will prohibit incandescent bulbs by 2014 [9, 10]. Also, the European Union is initiating a ban of incandescent bulbs in 2010 to hasten the transition to more efficient lighting [11]. Other countries, such as Australia and Canada, have similar impending litigation [12].

1.1.2 Comparison of General Illumination Sources

The primary substitutions for the incandescent bulb as a general lighting source are the high-intensity discharge lamp (HID), compact fluorescent lamp (CFL), and light-emitting diode (LED). Incandescent lights function by passing electric current through a thin tungsten filament, such that the high temperature causes light-producing radiation. Filling incandescent bulbs with halogen improves their efficiency and lifetime. HIDs generate light by sustaining an electric arc between electrodes in a plasma. CFLs stimulate mercury vapor to create ultraviolet light, which is converted into visible light by phosphor. LEDs are semiconductors that utilize electroluminescence, which is the production of light upon electrons and holes recombining within a material.

Luminous efficiency (lumens per watt) and device lifetime are the key metrics for light sources. A lumen is the international standard unit of perceived light by an ideal human eye, and it provides a quantitative value for the visible portion of a radiant flux. The three characteristics of optical performance for illumination are brightness (total lumen output), chromaticity (color temperature), and beam distribution. Other general lighting considerations include cost, environmental impact, application versatility, footprint, and weight.

A 65W incandescent bulb produces about 1,000 lumens, which can presently be achieved with a 26W CFL lamp or a 12–15W LED array [13-16]. The use of solid-state lighting requires arrays because a single LED is incapable of producing that much light output. High power LEDs, defined as those that consume at least 1 W, are the type of LEDs being considered for general illumination.

The recent lighting trend has been the changeover from incandescent bulbs to CFLs, since this transition increases efficiency by five times and lifetime by up to ten times. Lately, there has been little improvement in efficiency for all light sources except LEDs, as shown in Figure 3. Typical LEDs have an efficiency of around 75 lumens/watt, although prototypes are already capable of up to 150 lumens/watt [17, 18]. Because solid-state lighting is on course to be the source type with the best luminous efficiency, there is substantial motivation for using them in general lighting applications.

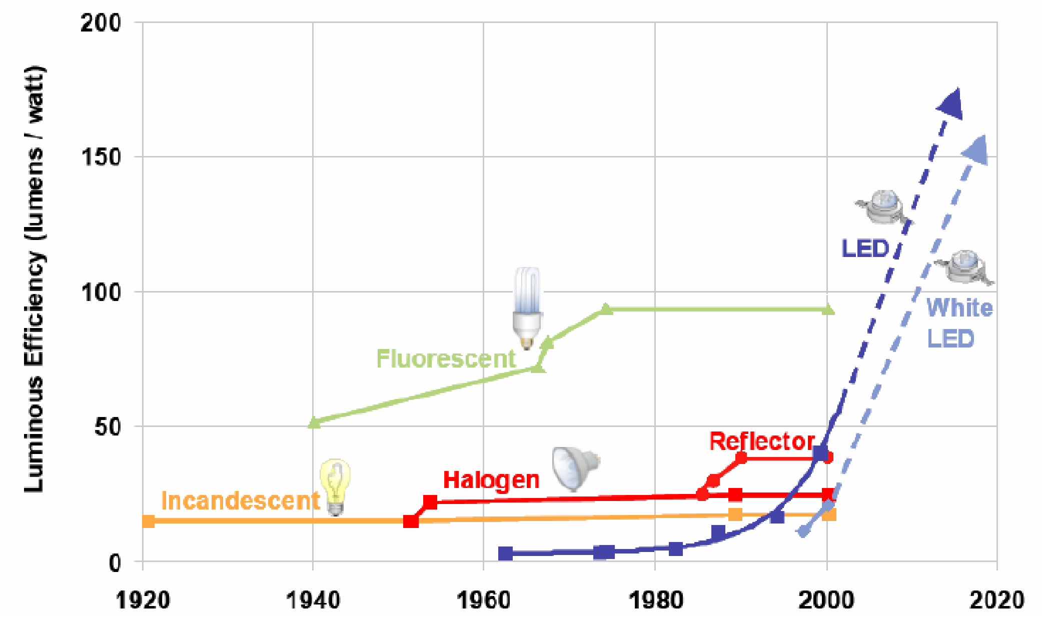

Figure 3. Luminous efficiency timeline for general illumination sources [18].

Solid-state lighting technology is on pace to outperform the other light source types for other characteristics as well. As Figure 4 indicates, LEDs are on course to be the option with the highest device lifetime and lowest ownership cost. Because they are solid-state devices, they are generally more durable than alternative light sources. Furthermore, the main competition is CFL lighting, which contains toxic mercury and has been criticized for the aesthetic quality of their light output and the long time it takes for the bulbs to reach full luminous output. Also, CFL lifespan is often severely reduced as its operation becomes more cyclical due to fatigue effects [19].

Moore's law for electronics refers to the exponential increase of cost-effective transistor density in the integrated circuit industry since 1958. Similarly, Haitz's law for solid-state lighting, as shown in Figure 5, refers to the exponential increase of efficiency and the exponential decrease of cost for LEDs since 1968 [20]. While these trends are promising, Figure 4 shows that LED cost is still over twice that of CFLs or HIDs. The other remaining major obstacle to LED commercialization is thermal management. Solid-state lighting must also address issues associated with a mature industrial infrastructure and established consumer expectations, such as the Edison screw mount.

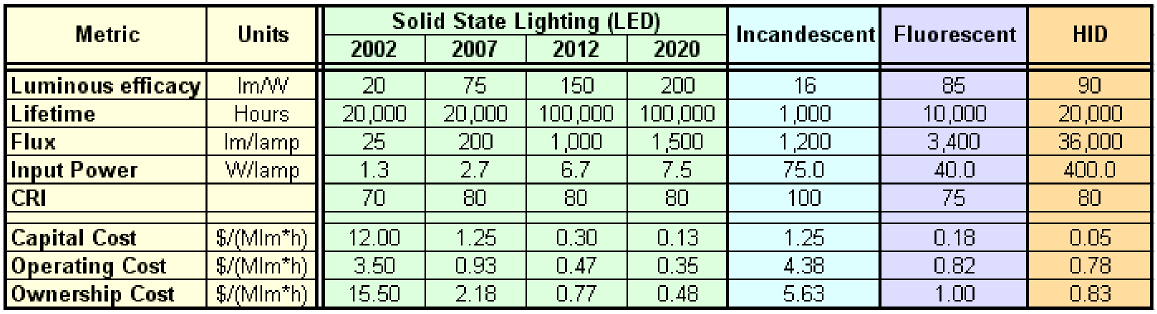

Metric	Units	Solid State Lighting (LED)				Incandescent	Fluorescent	HID
		2002	2007	2012	2020			
Luminous efficacy	lm/W	20	75	150	200	16	85	90
Lifetime	Hours	20,000	20,000	100,000	100,000	1,000	10,000	20,000
Flux	lm/lamp	25	200	1,000	1,500	1,200	3,400	36,000
Input Power	W/lamp	1.3	2.7	6.7	7.5	75.0	40.0	400.0
CRI		70	80	80	80	100	75	80
Capital Cost	$/(Mlm*h)	12.00	1.25	0.30	0.13	1.25	0.18	0.05
Operating Cost	$/(Mlm*h)	3.50	0.93	0.47	0.35	4.38	0.82	0.78
Ownership Cost	$/(Mlm*h)	15.50	2.18	0.77	0.48	5.63	1.00	0.83

Figure 4. U. S. Department of Energy roadmap for LED technology, compared to relatively stagnant performances of incandescent, fluorescent, and HID lights [21].

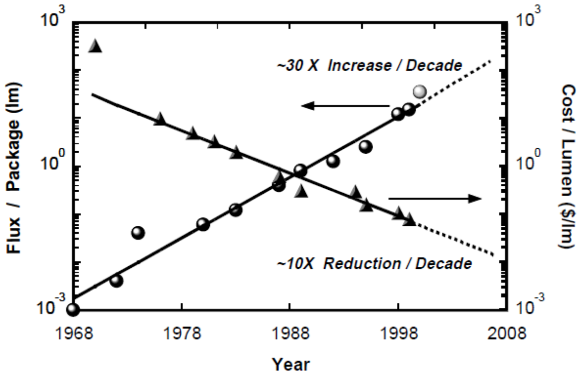

Figure 5. Haitz's law: a timeline of efficiency and cost for LEDs [20].

Since economies of scale have a considerable impact on the pricing of lighting devices, cost is not a crucial focus of this report. As an example, the capital cost of CFLs has been reduced by between 80% – 90% since 1983, while the annual production has scaled up to over a billion units [7]. On the other hand, innovative engineering is needed to provide robust cooling methodologies that can allow LED lighting applications to persevere. Thermal management has remained a major hindrance to the widespread implementation of solid-state lighting technology due to the limited thermal dissipation mechanisms and the strong dependence of performance and reliability on temperature. This relationship is better understood with a more detailed description of LED functionality, as depicted in Figure 6 and explained in the following subsection.

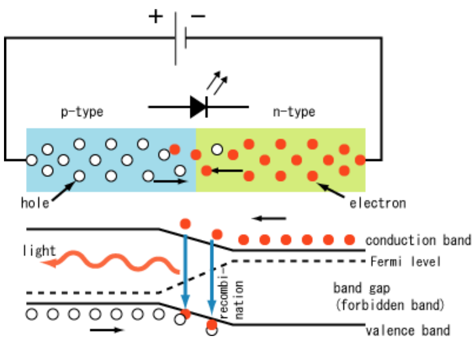

Figure 6. Schematic diagram of LED functionality [22].

1.1.3 Importance of Thermal Management for Solid-State Lighting

An LED is a semiconductor diode with a p-n junction, in which electrons and holes are able to recombine due to a supplied electrical current. Upon recombining, electrons jump from the conduction energy band to the valence band, and by crossing the Fermi level may emit light. The chromaticity of the light output is directly related to the emitted light's wavelength, which depends on the energy band gap that is dictated by the p-n junction materials and the junction temperature. Thus, the color of LED lighting is tunable without the usage of filters. More importantly, the luminous efficiency decreases as junction temperature increases because a smaller percentage of the electrons recombining with holes will emit light. This efficiency dependency is shown for various colors of LED lights in Figure 7.

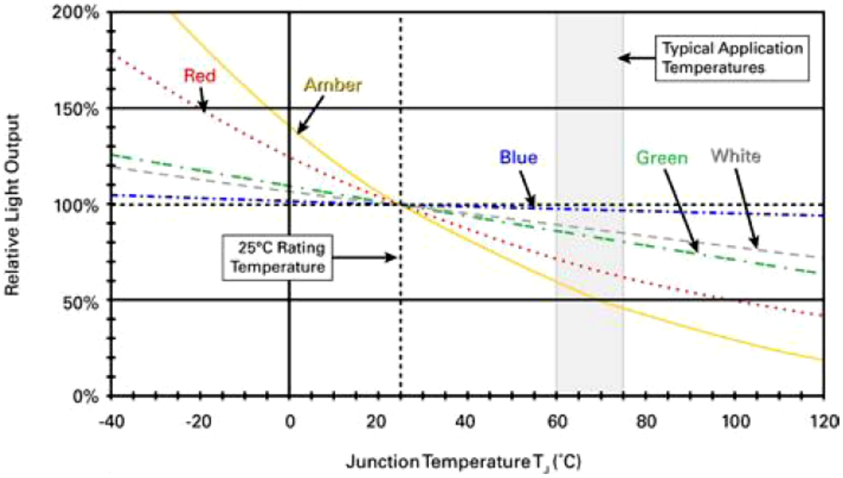

Figure 7. Light output variation of LEDs due to junction temperature [23].

Solid-state lighting device lifetimes are also highly dependent on junction temperature, as shown in Figure 8. Operating 10ºC above the specified temperature will reduce the average time-to-failure by approximately 50% for most LED applications [24]. In some instances, a high junction temperature may be a side effect rather than the root cause of failure. For instance, failure may occur due to electrostatic discharge, electrical overstress, high current densities, package stresses, or electrical shorts caused by threading dislocations or insufficient passivation [25]. Still, many LED devices are generally prescribed to be maintained below 100ºC – 185ºC, and the junction temperature's impact on device lifetime is illustrated by the Arrhenius equation [26-28]:

$$MTF = MTF_{ref} \exp\left({}^{E_a}\!\big/_{k_B T} \right) \tag{1}$$

MTF is the mean time to failure, which is commonly signified by the lumen output being reduced to 70% of the original output [28, 29]. MTF_{ref} is the reference mean time to failure, E_a is the activation energy, k_B is the Boltzmann constant, and T is the steady state temperature. One-watt high power LEDs have been shown to have activation energies as high as 1.5 eV [28].

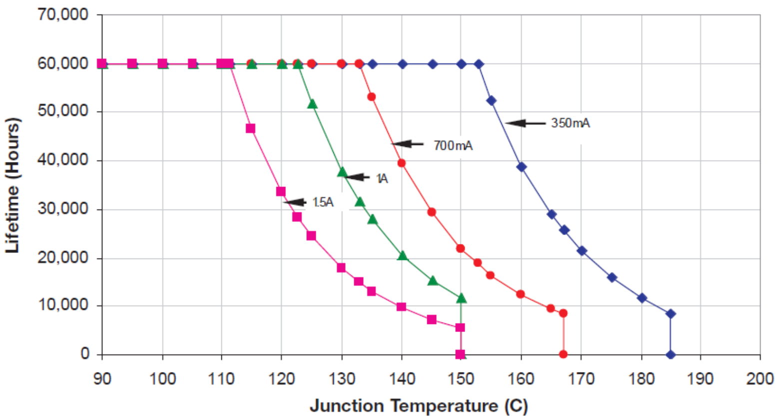

Figure 8. Lifetime vs. junction temperature for Luxeon K2 Lumileds [30].

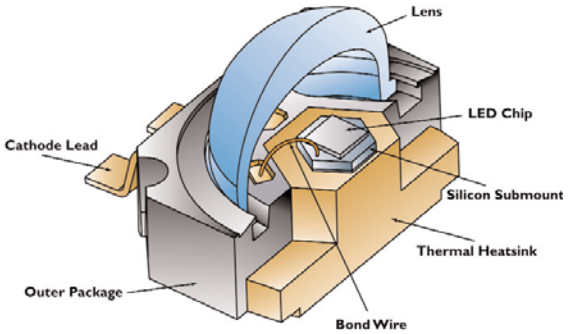

Figure 9. Luxeon K2 Lumiled schematic [30].

Operating LEDs at excessive temperatures can be detrimental for aspects other than those related to the solid-state lighting physics. A typical LED package is shown in Figure 9, which would have an encapsulation material under the lens to protect the die and bond wires. This encapsulant may discolor due to high temperatures, which would affect lumen output and color temperature [31]. Furthermore, thermal stresses caused by CTE mismatches may hasten fatigue failure because they can cause degradation and deficiencies within ohmic contacts [28]. Wire bonds are also susceptible to failure due to thermal stresses [32]. For LED technology to prosper despite severe thermal loads and limited space allocation, effective thermal management strategies are called for.

As lighting technology transitions from arcs/filaments to semiconductors, the thermal engineering approach becomes more closely related to compact electronics than traditional lighting. While most other types of lighting dissipate approximately 85–95% of their heat as direct convection or radiation heat transfer, those modes are insignificant for solid-state lighting. Meanwhile, the evolution of LEDs from indicator lights to general illumination applications has greatly increased power densities and enhanced the need for novel thermal management schemes. Around 70–90% of the energy supplied to LEDs becomes heat, virtually all of which must be conducted from the die [19].

1.1.4 LED Commercialization

LEDs and organic LEDs have penetrated various commercial sectors, as shown in Figure 10. Examples include architectural lighting, flexible electronic displays, traffic signals, street lighting, biomedical applications, automobile headlights, televisions, computers, cameras, digital photo frames, flashlights, and fiber scopes.

Figure 10. LED commercialization examples [33-39].

The financial incentives of installing down-lighting LEDs can be estimated with an energy savings calculator, as shown in Figure 11. For the example in this figure, the \$130 Cree LR6 LED light does not have financial break-even with incandescent lighting until 9,135 hours of operation, although lifetime savings are around \$4,250 [40]. In Figure 12, the optical performance of these LR6 LED lamps is contrasted with that of incandescent lighting for down-lighting in a restaurant. For other down-lighting applications, especially industrial ones, more total lumen output may be desired. This would require a higher power load, and thus more powerful thermal dissipation.

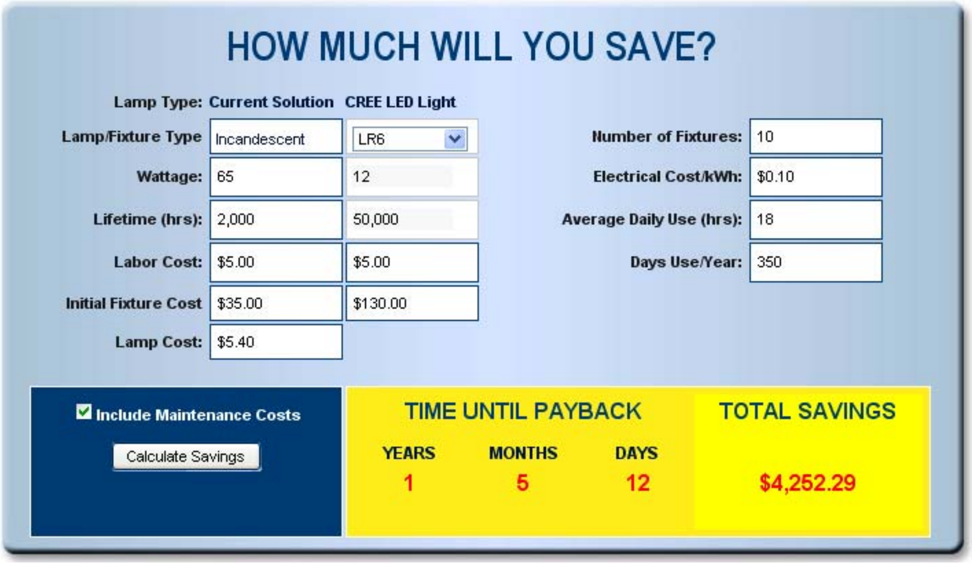

HOW MUCH WILL YOU SAVE?

Lamp Type:	Current Solution	CREE LED Light
Lamp/Fixture Type	Incandescent	LR6
Wattage:	65	12
Lifetime (hrs):	2,000	50,000
Labor Cost:	$5.00	$5.00
Initial Fixture Cost	$35.00	$130.00
Lamp Cost:	$5.40	

Number of Fixtures: 10
Electrical Cost/kWh: $0.10
Average Daily Use (hrs): 18
Days Use/Year: 350

☑ Include Maintenance Costs

TIME UNTIL PAYBACK

YEARS	MONTHS	DAYS
1	5	12

TOTAL SAVINGS
$4,252.29

Figure 11. Energy savings calculator for installing LED down-lighting [40].

65W Incandescent Bulbs
Total Power = 5,135W

12W LED Bulbs
Total Power = 948W

Figure 12. Friendly's Restaurant shown with incandescent vs. LED lighting [41].

1.1.5 Motivation Summary

Solid-state lighting potentially provides a durable, long-lasting, efficient, and cost-effective improvement over all other general illumination sources. However, the technological developments of LEDs have driven the need for innovative cooling methodologies in order to ensure sufficient device efficiency, lifetime, and chromaticity. The motivation for this project was the call to minimize the LED junction temperature for down-lighting applications by appropriately designing the forced convection flow pattern and heat sink geometry. To address this objective, the total system's thermal resistance was minimized by simultaneously engineering the active cooling flow, the convective surface area, and the conduction resistance within the heat sink. Consideration was given to the required energy input represented as the pumping power, as well as the aspects of manufacturing, footprint, and cost.

1.2 Thesis Overview

This numerical study investigated the thermal performance and pumping power requirements of forced convection on heat sinks with various fin and shroud geometries. Due to the interest in the thermal management of high power LED arrays, the largest heat sink considered had a base area of 101.6 mm by 101.6 mm, and the LEDs were modeled as distributed heat sources of 25–75 W. By using Fluent to parametrically explore the design space, this work discovered general trends and established guidelines for future designs. Specifically, this research addressed the following goals:

- Accurately predict the impact of confined space constraints on thermal performance and pumping power requirements for the active cooling of LED-scale heat sink systems with various pin fin and radial fin arrangements in pyramidal, square, conical, and circular shrouds.

- Develop heat sink and shroud optimization methodology that maximizes the overall thermal conductance by simultaneously considering thermal resistances, convective surface area, and flow field characteristics.
- Generate a framework for future system design and laboratory experiments.

Chapter 2 serves as an introduction to the thermal challenges related to LEDs by discussing thermal loading, characterization, and pathways. Also, an overview on the general thermal management of LEDs is provided. Chapter 3 reviews background information and publications about shrouded heat sinks and radial fins. The sections about shrouds are divided based on the flow type, and subsections are used to categorize heat sink fin types. An independent section is used to discuss studies focused on radial fins. Chapter 4 details the computer modeling used in this study by explaining the applied assumptions, geometry and mesh creation, procedure for a simulation run, and results validation. Chapter 5 reports the results of the parametric analyses and reveals trends in the design space. Lastly, Chapter 6 summarizes this study and proposes future work to further develop shrouded heat sink technology.

CHAPTER 2

BACKGROUND OF THERMAL ENGINEERING OF LEDS

2.1 Overview

2.1.1 LED Thermal Loading

LEDs are typically operated as DC constant-current light sources, and their luminous efficiency is often given at a certain drive current. This drive current is generally between 0.35 and 1.5 amps. Regardless of the architecture, a DC to DC driver or an AC to DC converter is necessary, with the former usually being more efficient than the latter. Nonetheless, only about 5% – 20% of the total power dissipation is from the driver electronics, which indicates that the thermal loading in an LED system is primarily caused by the LED dies themselves [42].

In order to achieve sufficient total lumen output for general illumination purposes, solid-state lighting often requires arrays. This compounds the thermal loading because LEDs placed in close proximity will often have thermal sources that interact with each other. At the very least, LED spacing in an array should be at least 4 – 5 mm [43].

The heat fluxes in LED packages can be as high as 1000 W/cm^2, although common packages usually have heat fluxes around 500 W/cm^2 [44-46]. This highly-concentrated heat generation is because high power LEDs are up to 5 W and have die areas as small as 1 mm^2 [29, 47]. Some GaN LED junctions have a maximum allowed temperature of 60ºC in order to achieve their rated efficiency, lifetime, and chromaticity [48]. However, most modern high power LEDs are designed to have junction temperatures in the 100ºC – 185ºC range [30, 49, 50].

2.1.2 Thermal Characterization

A system's thermal performance may be characterized by numerical techniques and experimental studies. Analytical solutions, resistor networks, and numerical solutions can be utilized for combined mode heat transfer modeling, which relies on the governing differential equations based on the conservation laws of energy, mass, and momentum. For the thermal characterization of general illumination applications, steady-state operation is typically considered.

Computational fluid dynamic (CFD) programs provide a preprocessor, solver, and postprocessor for numerical solutions. The solver can be based on finite element, finite difference, or finite volume methods. To gauge the accuracy and precision of CFD results, temperature-dependent parameters may be experimentally measured based on electrical, optical, or physical contact methods. Zou et al. created an integrated measurement system for LEDs in which thermal, optical, and electrical characteristics are ascertained. Their procedure allows for the experimental determination of the thermal resistance from the device's junction to any other reference point [23].

2.2 LED Thermal Pathways

2.2.1 Heat Dissipation Overview

The thermal resistance networks of LED applications can be quite intricate, although they are often simplified as shown in Figure 13. Heat is conducted through the heat sink to its surfaces where convection and radiation cause thermal dissipation. An LED's junction temperature is determined by the heat load, the thermal resistance path from the device junction to the ambient environment, and the ambient temperature.

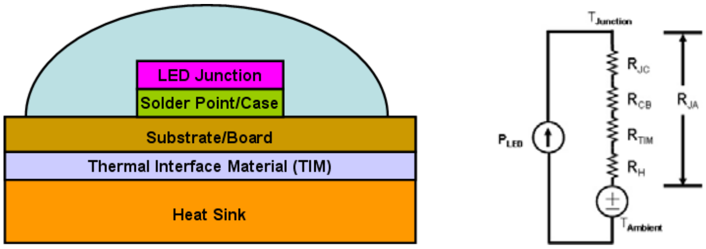

Figure 13. Simplified thermal resistance network for LED illumination.

In general, most heat sinks attached to general illumination sources are cooled by air. For very small dimensions, packages and heat sinks are prone to experience developing turbulent flow, sometimes even for natural convection. On the other hand, many lighting applications entail tight design constraints, constricted clearances, elevated ambient temperatures, building codes, and air pathways susceptible to clogging [51].

Thermal interface resistances and spreading resistances, as depicted in Figure 14, have critical roles for small-scale conduction. Ideally, thermal interface materials with very high thermal conductivity would be applied to perfectly flat contact areas at interfaces. The quality of bonding materials is dependent on their mechanical durability, manufacturability, and thermal performance. For mounting the heat sink, mechanical attachments such as screws, springs, or clips are preferable over adhesives and tape. Thermal grease or thermal compounds are often applied to interfaces to eliminate air gaps and maximize the contact area [52, 53].

Figure 14. Spreading resistance and contact resistance schematics [54].

2.2.2 Heat Sink Considerations

Heat sink design will influence the convective surface area and how it receives approaching flow. The geometry is usually a flat plate, extruded finned, or die-cast finned. While there should be ample surface area to permit suitable heat transfer at the surface, proper aerodynamic design should allow the fluid to flow swiftly for a reasonable pumping power. A large flat plate's thermal performance may be competitive with that of a finned heat sink, but the latter is often preferred when space is limited.

Thermal radiation from heat sinks may be a significant portion of heat transfer for natural convection and for heat sinks at very high temperatures. Surface coatings are often used to increase emissivity. Anodizing and etching can also help increase the radiative heat transfer [52, 53].

2.3 LED Thermal Management Framework

2.3.1 Overview

Before applying thermal management technologies, all significant heat sources and thermal constraints should be identified. Also, front-end design should include an effort to minimize the thermal load that needs to be dissipated. Consideration should be given to the device's tolerated temperatures, total operation cost, and system robustness.

Passive cooling methods, requiring no energy input, include the use of thermal vias, heat spreading mechanisms, phase change materials, heat sinks, heat pipes, and materials with high thermal conductivity [32, 55]. Attaching a common, basic heat sink or heat pipe to a compact electronic device typically reduces the thermal resistance by 50% – 80% [51, 56].

Active cooling methods require external energy, and they usually involve higher cost, volume, and noise than passive methods. Also, active techniques are intrinsically at risk of malfunctioning. Active cool methods include forced convection, liquid loops, thermosyphons, spray cooling, thermoelectric cooling, vapor compression refrigeration, cold plates, and thermoionic cooling [32, 55].

Generic cooling enhancement techniques include surface roughening, corrugations, and surface interruptions [57, 58]. Also, heat generation may be reduced from the supply-side by power minimization or power management improvements. This can be done with dynamic power management, demand-based switching, glitch reduction, power harnessing technology, path reduction, and placing driver electronics far enough away from temperature-sensitive devices [32, 55].

Techniques that enhance upon the above methods are also in development. Banks of micro pin fins have shown promise for liquid cooling, with heat transfer coefficients similar to boiling flow [59, 60]. Micro-fluidic cooling has been used to cool high power LEDs with thermal loads up to 220W. These micro-jet structures dissipated a thermal load 50% higher than the baseline, and reduced the maximum temperature by as much as 23°C [61-66]. Metal honeycomb structures have improved the heat transfer rate of an open duct by two orders of magnitude, but its turbulent flow causes loud noise [67, 68].

Closed-loop feedback systems have been proposed for LED light applications. With integrated temperature sensors, LED modules could self-adjust the drive current, and thus the temperature of the device [29]. Alternatively, an array of LEDs could operate only certain members of the array at a given time. The switching time between different groups of LEDs could be designed to prevent overheating.

2.3.2 Importance of Materials

Material selection has a critical role in compact electronic devices, as the conductivity directly impacts the thermal dissipation efficiency. Ideally, the materials would be low-cost, have high thermal conductivity, and have a low and tunable coefficient of thermal expansion (CTE). Also, density should be low if weight is a concern. Other properties, such as strength, stiffness, and electrical resistivity, may be important. The goals of material selection include improving device performance, thermal regulation, and manufacturing yield, as well as reducing thermal stresses, warping, size requirements, weight, and cost.

Common heat sink materials include aluminum, duralumin, and copper. Next-generation materials have shown strong potential to significantly increase the thermal conductivity and drastically decrease the CTE, as shown in Table 1. The transition to advanced materials is being hampered by high costs and a mature industrial infrastructure. However, some commercial microprocessor heat sinks are now being made with diamond particle-reinforced silicon carbide [69].

Thermal interface materials (TIMs) that minimize interfacial resistances constitute a substantial research field. Vertically aligned carbon nanotube arrays have been used as a TIM on aluminum heat sinks for high power LEDs, and the interface thermal resistance has been as low as 38 mm^2K/W [70]. Generally for LED light engines, the thermal resistance from the TIM is less than 0.05 K/W [49].

Table 1. Properties of traditional and advanced packaging materials [69].

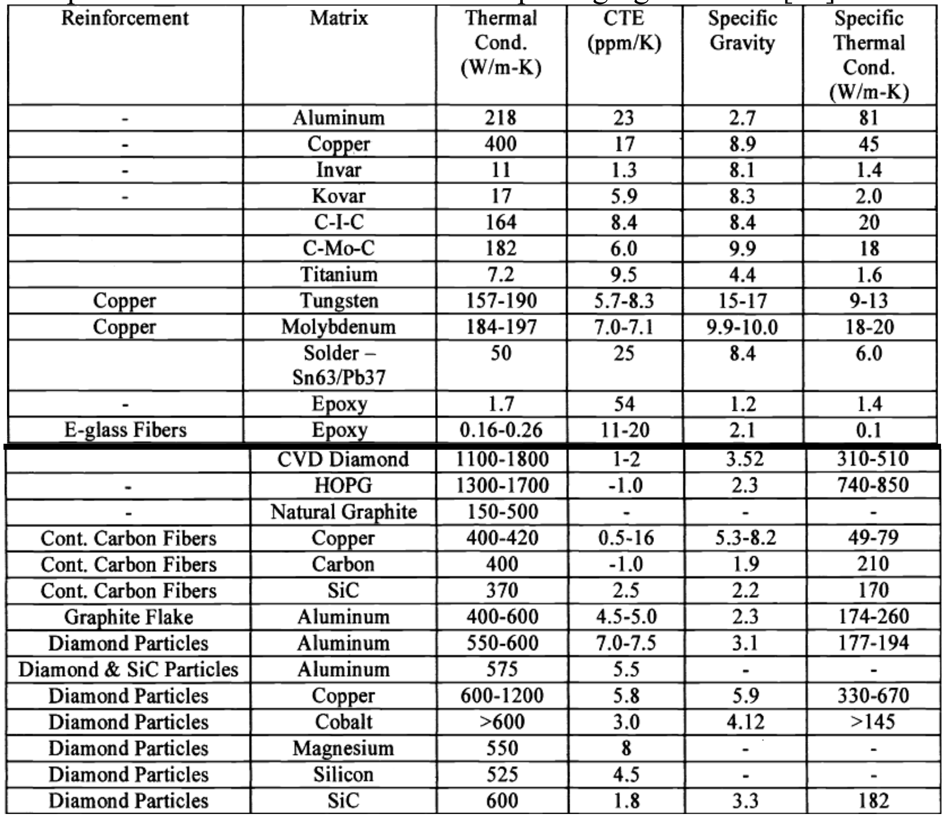

Reinforcement	Matrix	Thermal Cond. (W/m-K)	CTE (ppm/K)	Specific Gravity	Specific Thermal Cond. (W/m-K)
-	Aluminum	218	23	2.7	81
-	Copper	400	17	8.9	45
-	Invar	11	1.3	8.1	1.4
-	Kovar	17	5.9	8.3	2.0
	C-I-C	164	8.4	8.4	20
	C-Mo-C	182	6.0	9.9	18
	Titanium	7.2	9.5	4.4	1.6
Copper	Tungsten	157-190	5.7-8.3	15-17	9-13
Copper	Molybdenum	184-197	7.0-7.1	9.9-10.0	18-20
	Solder – Sn63/Pb37	50	25	8.4	6.0
-	Epoxy	1.7	54	1.2	1.4
E-glass Fibers	Epoxy	0.16-0.26	11-20	2.1	0.1
	CVD Diamond	1100-1800	1-2	3.52	310-510
-	HOPG	1300-1700	-1.0	2.3	740-850
-	Natural Graphite	150-500	-	-	-
Cont. Carbon Fibers	Copper	400-420	0.5-16	5.3-8.2	49-79
Cont. Carbon Fibers	Carbon	400	-1.0	1.9	210
Cont. Carbon Fibers	SiC	370	2.5	2.2	170
Graphite Flake	Aluminum	400-600	4.5-5.0	2.3	174-260
Diamond Particles	Aluminum	550-600	7.0-7.5	3.1	177-194
Diamond & SiC Particles	Aluminum	575	5.5	-	-
Diamond Particles	Copper	600-1200	5.8	5.9	330-670
Diamond Particles	Cobalt	>600	3.0	4.12	>145
Diamond Particles	Magnesium	550	8	-	-
Diamond Particles	Silicon	525	4.5	-	-
Diamond Particles	SiC	600	1.8	3.3	182

Inner-device resistance relates to the definitive behavior of the solid-state lighting technology, which is persistently in development. For example, Table 2 shows the impact of using various heat slug materials for LEDs. Recent achievements in LED manufacturing, such as the chemical-mechanical polishing method that replaced the laser-lift off process, have resulted in inner-die resistances as low as 1 K/W [48].

Table 2. Comparison of heat slug effects on LED thermal resistance [71].

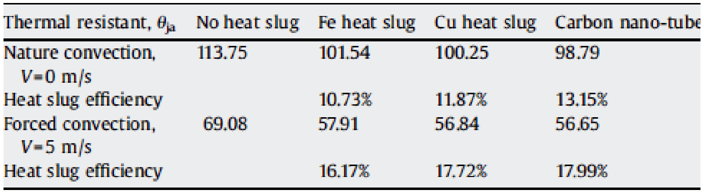

Thermal resistant, θ_{ja}	No heat slug	Fe heat slug	Cu heat slug	Carbon nano-tube
Nature convection, $V=0$ m/s	113.75	101.54	100.25	98.79
Heat slug efficiency		10.73%	11.87%	13.15%
Forced convection, $V=5$ m/s	69.08	57.91	56.84	56.65
Heat slug efficiency		16.17%	17.72%	17.99%

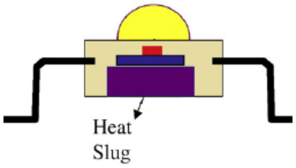

2.3.3 Importance of Flow Pattern

It is important for heat sink designers to remain conscience of how the fluid flow is being utilized. Jet flow fans use pulsation, while conventional fans create swirling flow and have hubs that consist of 25% – 30% of its frontal area. If traditional fans are applied directly to unmodified heat sinks, as shown in Figure 15, the resulting middle hot spot is detrimental for the overall system conductance.

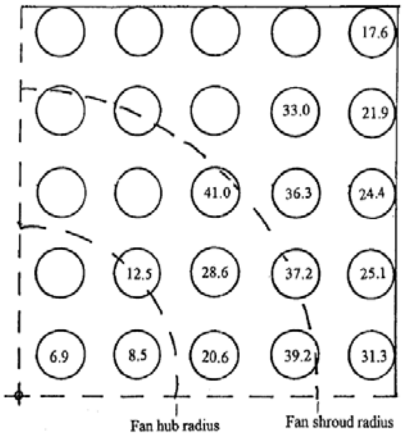

Figure 15. Heat transfer coefficient distribution for cylindrical fins experiencing impingement flow from a conventional fan [72].

Most down-lighting applications inherently have some sort of housing that acts like a shroud and affects the flow. The ability to concurrently optimize these housings for thermal and optical performance will enhance the possibility for the widespread implementation of LED general illumination. An example LED down-lighting fixture is shown in Figure 16, although it is limited to a 600 lumen output because its thermal dissipation relies on natural convection [73]. It is noteworthy that this system has slightly curved radial fins, as well as driver electronics placed outside of the housing.

Figure 16. Commercial fixture for recessed LED down-lighting [73].

Applying a shroud to a heat sink can either improve or worsen a system's performance. For natural convection, the shroud's value is dictated by how much the buoyancy increases compared to the additional viscous effects, as well as how much it impedes radiation to ambient conditions. For forced convection, shrouds are used to guide the cooling fluid and prevent flow by-pass. Most shroud applications for reducing the thermal resistance of an active cooling system require a higher pumping power.

2.3.4 Importance of Design Flexibility and Ingenuity

The LED light systems that successfully penetrated the market, as discussed in §1.1.4, were mostly novel concepts that leveraged design flexibility. For example, the LED automotive headlamps shown in Figure 17 have junction temperatures of 70.6ºC and 30.25ºC for an air inlet velocity of 0 and 75 miles per hour, respectively. These temperatures were further reduced by about 4ºC from integrating fins into the system [74]. As another example, the Federal Aviation Administration weatherability regulation for airport taxiway lights was satisfied by the LED design shown in Figure 18. By partially recessing the lights into the heat sink, snow and ice could be melted so as to prevent light inhibition. In addition, the incorporated variable-current system enhanced the energy conservation [75].

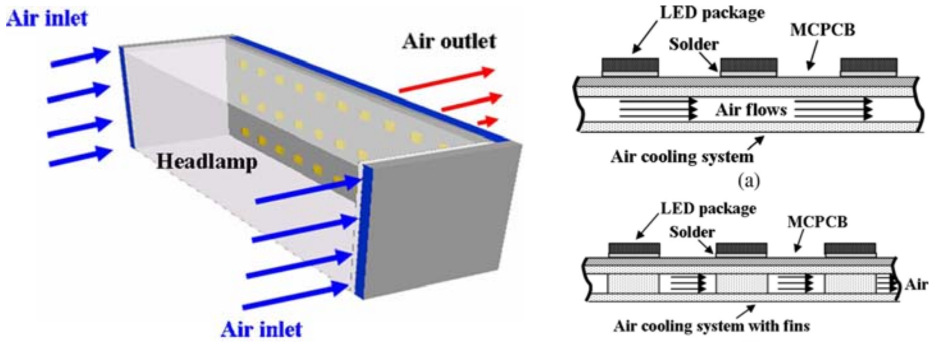

Figure 17. Cooling system for automotive headlamp system of LED arrays [74].

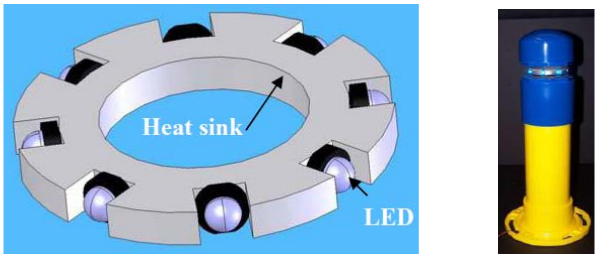

Figure 18. Cooling system for airport taxiway LED fixtures [75].

2.4 Summary

For solid-state lighting, thermal management severely dictates the efficiency, performance, and reliability. Tradeoffs are usually needed to satisfy conflicting thermal, mechanical, electrical, optical, and cost design requirements. The most promising cooling methodologies seem to be optimized flow, power minimization, synthetic jets, micro-jet arrays, advanced thermal vias, flip-chip packaging, direct copper bonded ceramic substrates, and material enhancement [32, 53, 76-80].

For LED lighting, the thermal resistance from the heat sink's conduction and convection is becoming more significant as developments are diminishing other thermal resistances in the system. As shown in Figure 19, there have been great reductions in the thermal resistance of commercial LED packages. In turn, the focus for cooling high power LEDs has been shifting to an overall system consideration. Figure 20 illustrates how poor heat sink design may restrict heat dissipation, and thus why there is an opportunity to improve LED thermal management.

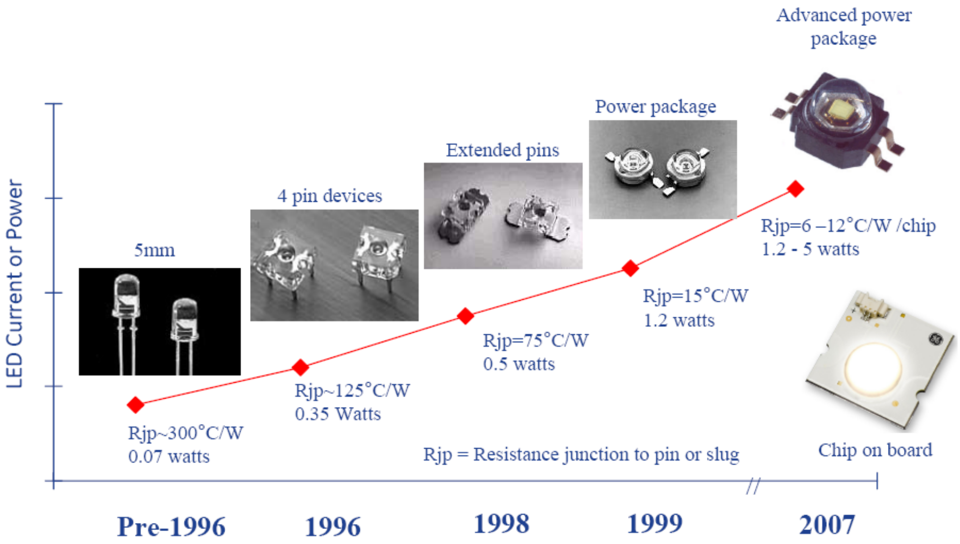

Figure 19. Level 1 package development for high power LEDs [47].

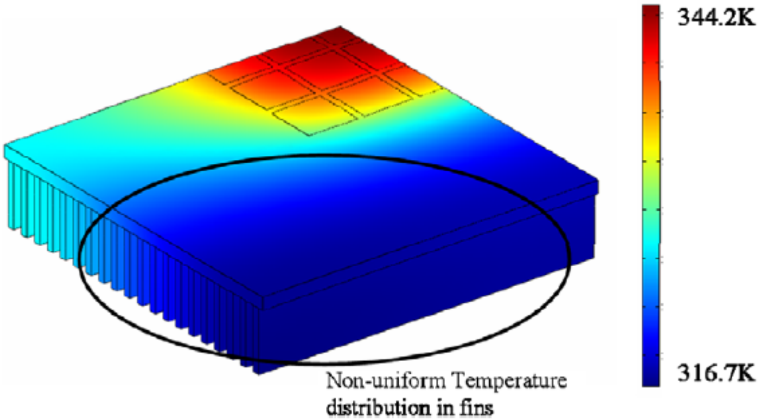

Figure 20. Poorly utilized heat sink for an LED array, indicated by the highly non-uniform temperature in the heat sink fins [49].

By utilizing thermal resistance networks, such as that of Figure 21, the most important factors in the thermal conductance of a system may be pinpointed. This research analyzed the impact of the heat sink and shroud geometries on the total system resistance, although the active cooling model that was used only included resistances from convection and within the heat sink. Radiation is typically responsible for less than 5% of heat transfer in forced convection and was assumed negligible for this study. The resistances from thermal interfaces and within the LED constitute research fields beyond the scope of this work.

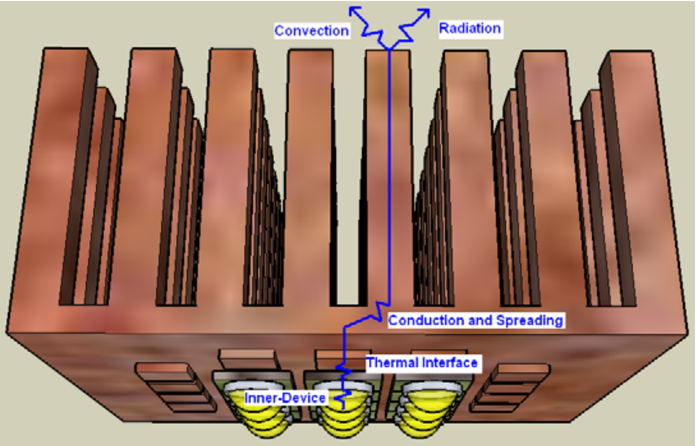

Figure 21. Simplified thermal pathway of an array of down-lighting LEDs attached to a heat sink.

CHAPTER 3

LITERATURE REVIEW OF SHROUDED SINKS AND RADIAL FINS

3.1 Overview

The thermal performance of a heat sink system depends on the material properties, fin dimensions, fin density, fin spacing, interfacial material(s), heat source location(s), heat source size(s), and all of the characteristics of the flow field. Most of the reviewed publications parametrically analyzed the heat sink fin geometry within fixed shrouds or studied various shrouds applied to a fixed heat sink. Some of the general studies established the fundamental performance limits of various heat sinks [81-84]. Only a very limited amount of forced convection publications reported the relationship between their system's overall thermal resistance and the corresponding energy input.

Shroud applications predominantly spawned from natural convection enhancement, also known as the chimney effect. Most contributions on shrouded free convection were experimental studies, as a numerical analysis of this type requires large amounts of computational power and time. This is due to the inherent need to include radiation and a thermally-dependant fluid density. The only reviewed natural convection analyses that used computer modeling were by Yalcin et al., Arik et al., and Yazawa.

As power densities are becoming too high to be dissipated by free convection, such as in some high power LED applications, shroud studies pertaining to active cooling are becoming more prevalent. Analyses of forced convection may often legitimately assume constant fluid density and negligible radiation heat transfer. Thus, many of the reviewed active cooling analyses utilized computational fluid dynamic programs.

Parametric studies on shrouds are far from exhausted due to the myriad of possible configurations and system geometries. Most contributions assessed performance based on temperature vs. volumetric flow rate, while some reported volumetric flow rate vs. pressure drop. Only recently have forced convection studies been relating the thermal performance to the required energy input. Also, the focus has been appropriately shifting to the minimization of the entire system's thermal resistance.

Many of the reviewed studies had the goal of maximizing the Nusselt number. This metric provides a comparison between the convection and conduction components of heat transfer across a solid-fluid boundary, and an increase in the Nusselt number indicates a growing dominance of convection. Simply maximizing the convection coefficient or the Nusselt number ensures good convection performance, but it does not guarantee that there is sufficient conduction performance within the heat sink. Thus, this approach often fails to minimize the device's junction temperature.

Commercial LED products are increasingly utilizing radial fins for both natural and forced convection, as exemplified in Figure 22. Recent studies on various configurations of radial fins, including curved geometries, have revealed interesting design guidelines for enhancing heat transfer.

Figure 22. Commercial LEDs with radial fins and Edison screw mounts [13-16].

General shroud optimization strategies were not thoroughly detailed until lately. In a recent publication, Bejan described an optimization strategy based on exergy analysis, entropy generation minimization, and thermo-economics. An exergy analysis qualifies the energy available to do work and provides information on where waste energy is lost. Entropy generation minimization considers thermodynamics, heat transfer, and fluid mechanics in its pursuit to maximize the percentage of a system's available energy that does useful work. Thermo-economics is an analysis of how much it costs to manufacture and operate an energy system. Bejan claimed that thermodynamic optimization should still be the first step in design, as this allows trends to be discovered and optimization opportunities to be better illustrated [85].

In this chapter, §3.2–3.5 review shrouded heat sink research and are sectionalized based on the type of flow field. Each section is further divided based on heat sink geometry. §3.2–3.4 refer to forced convection studies only. §3.2 pertains to impingement flow, which is common in cooling electronic devices, processing materials, and cooling turbine blades. §3.3 analyzes the transition of impingement flow to horizontal cross-flow that some systems experience, while §3.4 pertains to pure horizontal cross-flow. §3.5 reviews pure vertical cross-flow, in which natural convection enhancement accounts for a substantial amount of the material. §3.6 discusses publications regarding the modern research fields of radial fins and curved radial fins. Lastly, §3.7 summarizes some of the key findings from this literature review.

3.2 Impingement Flow

3.2.1 Square Pin Fins

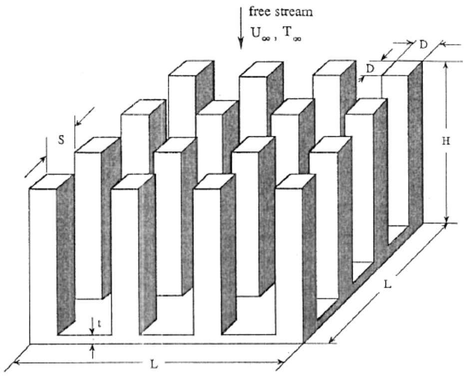

Figure 23. Impingement cooling of square pin fin heat sinks [86].

Maveety and Jung aimed to optimize square pin fin heat sinks experiencing impingement cooling by having appropriate thermal capacitance, ample convective wetted surface area, and balanced spreading resistances. According to their suggestions, the baseplate should generally be between 1-6 mm thick, and further geometric guidelines are reported in Equations (2)–(4) [87]. Figure 23 provides a visual explanation of the geometric variables.

$$\frac{H}{L} = .53 \tag{2}$$

$$\frac{D}{L} = .1 \tag{3}$$

$$\frac{S}{L} = .05 \tag{4}$$

Furthermore, Equations (5) and (6) indicate the optimal fin height (H_{opt}) and optimal fin thickness ($D_{\mathrm{f,opt}}$), in which A_p is the fin's cross-sectional area, h is the average heat transfer coefficient, and k is the thermal conductivity [87].

$$H_{\text{opt}} = 1.2629\left(\frac{kA_{p}}{4h}\right)^{1/3} \tag{5}$$

$$D_{\text{f,opt}} = \left(\frac{A_{p}}{1.4192}\sqrt{\frac{4h}{k}}\right)^{2/3} \tag{6}$$

The dependency of the optimal fin diameter on the Reynolds number and fin height for this configuration is illustrated in Figure 24.

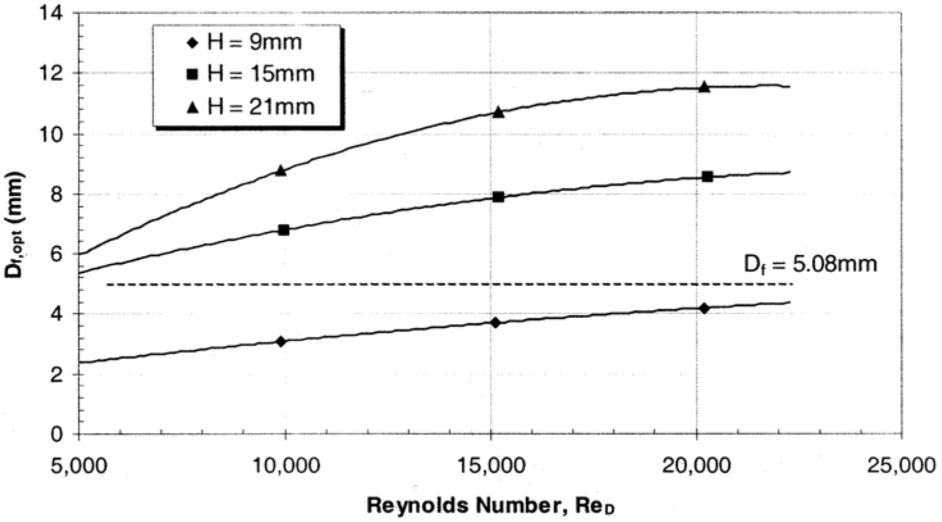

Figure 24. Optimal fin diameter vs. impingement Reynolds number for square pin fin heat sink with three different fin heights [87].

Bejan found the optimal fin spacing for this set-up to be within 16% of:

$$\frac{S_{\text{opt}}}{L} = .81\,\text{Pr}^{-.25}\ \text{Re}_{\text{L}}^{\ -.32} \tag{7}$$

Equation (7) is valid for $.06 < D/L < .14$ and $.28 < H/L < .56$ and $.72 < Pr < 7$ and $10 < Re_D < 700$ and $90 < Re_L < 6{,}000$ [86].

Maveety and Jung applied a deflector plate to a heat sink that was optimized according to Equations (2)–(6). They observed an 11.8% reduction in the thermal resistance when the plate was placed 1.5 mm from the heat sink, as shown in Figure 25. The plate created a more desired flow pattern and increased the velocity from around 9 m/s to 11 m/s [87].

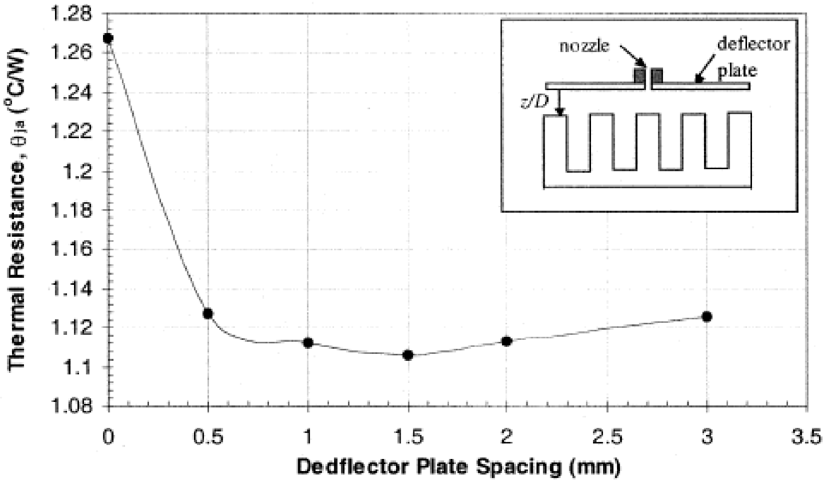

Figure 25. Thermal resistance improvement from applying a deflector plate to square pin fins experiencing impingement flow [87].

3.2.2 Cylindrical Pin Fins

Zheng and Wirtz studied a horizontal cylindrical pin fin heat sink with a fan resting on top of it. Their method of maximizing the product of flow rate and heat transfer surface area (UA) is satisfactory if the fan operating point is set, but it does not account for spreading resistance or energy input. As such, their approach only optimized the convection performance for set flow conditions. For many of the cases they studied, the Fin Area Density of 0.2 corresponded to the minimum U*A product, and hence their worst-case convection performance. The equation for the Fin Area Density *D* is:

$$D = n^2 \frac{\pi}{4}\left(\frac{d}{L}\right)^2 \tag{8}$$

In Equation (8), *n* is the number of fins, *d* is the fin's hydraulic diameter, and *L* is the heat sink's footprint length.

Figure 26 shows the Nusselt number as a function of *D* for a range that encompasses both an experimental method and that of a previously developed correlation. The Nusselt number for jet impingement was higher than fan impingement by 10% and 37% for a Reynolds number of 1,000 and 10,000 respectively [88].

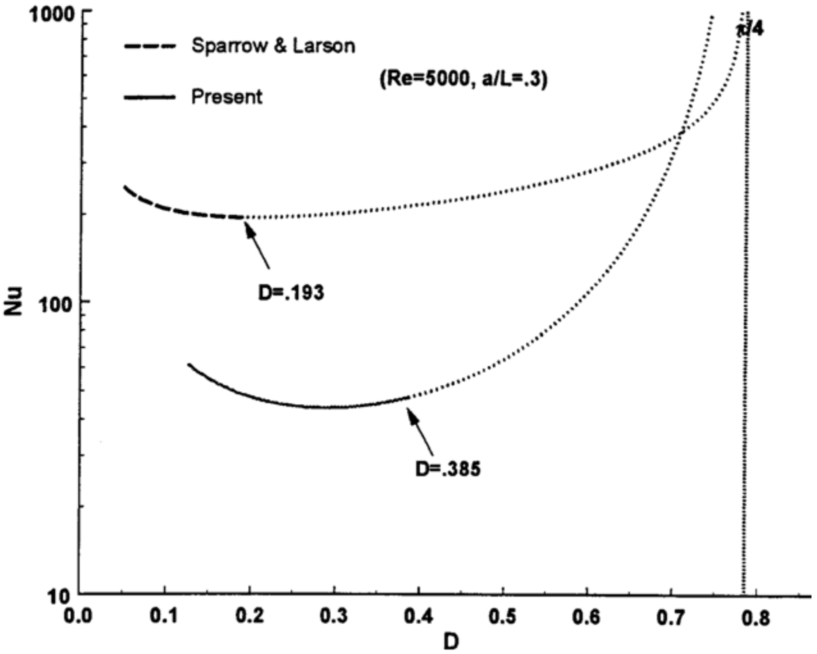

Figure 26. Sparrow and Larson jet impingement correlation, compared to fan impingement experimental data for cooling cylindrical pin fins [88].

3.3 Impingement Flow Transitioned into Horizontal Cross-Flow

3.3.1 Extruded Fins

Duan and Muzychka applied a shroud to convert impinging flow into horizontal cross-flow for a heat sink of extruded fins. They developed a correlation to compare the pressure drop to the velocity with an accuracy of ±20% and a root mean square error of 11.5%. Subsequently, they analyzed the thermal performance of four heat sinks and graphed the average channel Nusselt number vs. dimensionless thermal developing flow length, shown in Figure 28. Their heat transfer correlation was ±11% of the experimental results. There was no connection between the thermal and pressure performance [89, 90].

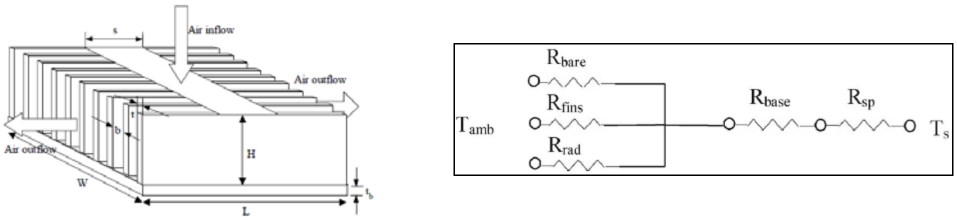

Figure 27. Impingement flow transitioned into horizontal cross-flow for extruded fins. The air inflow region represents the shroud opening [89].

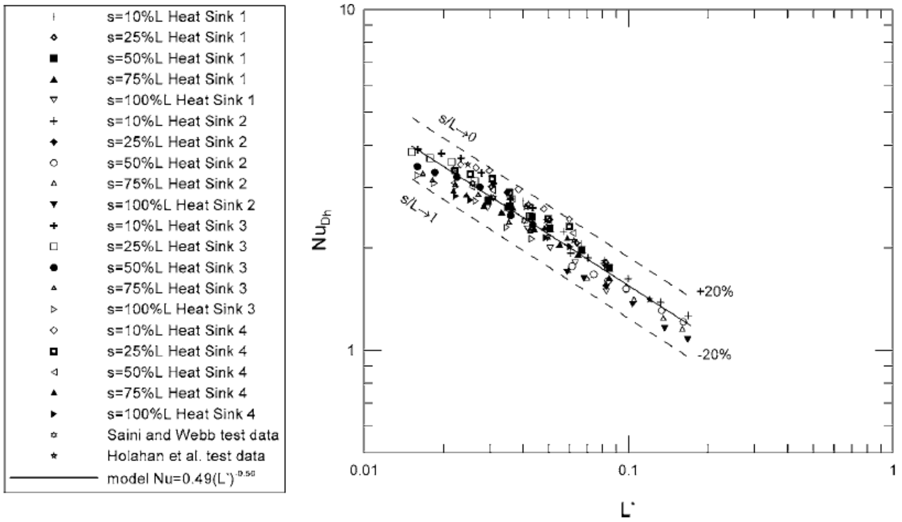

Figure 28. Duan and Muzychka's experimental data and model [89].

3.3.2 Cylindrical Pin Fins

Sparrow and Larson utilized a shroud to convert impinging flow into horizontal cross-flow for a heat sink of cylindrical pin fins, as shown in Figure 29. The heat transfer coefficients for the fins along the outer ring of the sink were the highest, and those of the middle fins were the lowest. The dimensionless heat transfer coefficients were virtually independent of both the fin's height-to-diameter ratio and the fin's spacing-to-diameter ratio when correlated with the appropriate Reynolds number. The longitudinal flow's Reynolds number was used for the inner fins, while the cross-flow's Reynolds number was used for the outer fins. Their correlations for the Nusselt and Sherwood numbers are given in Equations (9)–(13) [91].

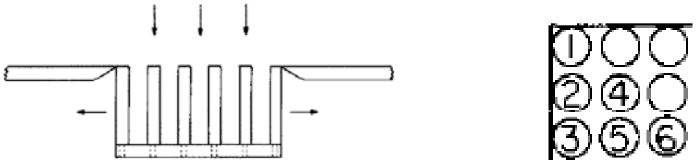

Figure 29. Impingement flow transitioned into horizontal cross-flow for cylindrical pin fins, shown with schematic of quarter heat sink's pin fin numbering scheme in which Fin Location 6 is closest to the heat sink center [91].

$$Nu = \left({}^{Pr}\!/_{Sc} \right)^{n} Sh = \left({}^{.7}\!/_{2.5} \right)^{.36} Sh = .632Sh \tag{9}$$

$$Sh = .321RE_{C}^{.647} \quad \text{for Fin Location 1} \tag{10}$$

$$Sh = .609RE_{C}^{.579} \quad \text{for Fin Locations 2 and 3} \tag{11}$$

$$Sh = .357RE_{L}^{.582} \quad \text{for Fin Locations 4 and 5} \tag{12}$$

$$Sh = .190RE_{L}^{.626} \quad \text{for Fin Location 6} \tag{13}$$

3.4 Horizontal Cross-Flow

3.4.1 Overview

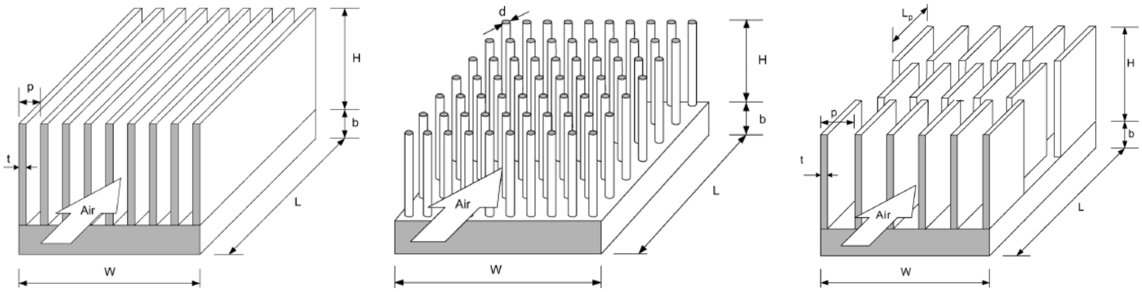

Figure 30. Horizontal cross-flow through extruded fins, in-line cylindrical pin fins, or staggered rectangular fins [92].

Horizontal cross-flow is the most widespread studied flow pattern for shrouded forced convection, with Kim and Webb's publication being an extensive review of the side-inlet-side-exit flow of ducted heat sinks. A sink of in-line cylindrical pin fins optimized for convective thermal resistance had a value that was 32.8% higher than that of optimized extruded fins. Meanwhile, the optimized staggered cylindrical pin fins had a convective thermal resistance 46.4% higher than that of the extruded fins. Optimized staggered rectangular fins had 2.9% lower convective thermal resistances than those of the extruded fins [92]. More details from this study are provided later in this chapter.

3.4.2 Extruded Fins

For extruded fins in cross-flow, minimizing the thermal resistance is highly dependent on the appropriate fin thickness and fin pitch. Fins must be thick enough so that fin efficiency is suitable, while pitch and thickness should be managed to prevent the need for a high pressure drop. The optimal extruded fin thickness and pitch are approximately .55 mm and 2.00 mm, respectively [92, 93].

Holahan utilized this configuration to create a method for selecting fin-fan combinations when trying to find the maximum volumetric conductance. He stressed the importance of considering the fan volume when designing for a specific heat sink's volumetric effectiveness. The equation for Net Volumetric Conductance (W/K*m^3) is:

$$C_{\text{sys}} = \frac{C_{\text{HS}}}{V_{\text{fan}} + V_{\text{HS}}} = \frac{N_{\text{fins}} C_{\text{fin}}}{D^3 + N_{\text{fins}} wHL} \tag{14}$$

C_{HS} is the overall conductance of the fin matrix, $V_{\text{fan}} + V_{\text{HS}}$ is the package volume, N_{fins} is the number of fins, C_{HS} is the overall conductance of one fin, D is the fan housing length, and wHL are the fin dimensions. Holahan's program iterates through hydraulic points to find the minimum required fan volume, followed by a calculation of how many fins the fan's flow can handle at that pressure, and concludes with a thermal performance evaluation. In this manner, Holahan has created a way to find the optimum fan diameter that achieves the highest net volumetric conductance for a set fin geometry and spatial arrangement [94].

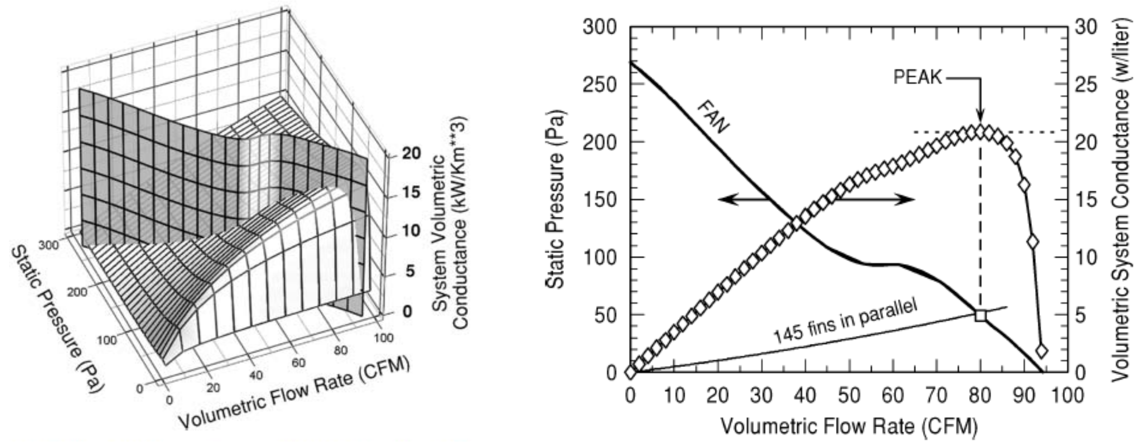

Figure 31. Potential system volumetric conductance, intersecting with actual fan curve for extruded fins experiencing horizontal cross-flow; Peak volumetric system conductance for given fan [94].

Bar-Cohen's group performed a parametric study on the side-inlet-side-exit cooling of extruded fins. Their baseline results for the system without the shroud are provided in Table 3. They found that as the shroud-fin clearance went from large to small, their optimum fin density progressed from 24 to 32. The shroud's impact was more significant for velocities less than 3 m/s. The data for the shrouded cases is in Figure 32 [95].

Table 3. Thermodynamic performance of extruded fin heat sink experiencing horizontal cross-flow [95].

		Sparse Heat Sink $N_{fin} = 16$, $s = 4.21$mm		Moderate Heat Sink $N_{fin} = 24$, $s = 2.57$ mm		Dense Heat Sink $N_{fin} = 32$, $s = 1.78$ mm	
Vol. flow rate (m^3/s)	Velocity (m/s)	R_{hs}, K/W	ΔP, Pa	R_{hs}, K/W	ΔP, Pa	R_{hs}, K/W	ΔP, Pa
0.005	1.5	0.391	3.986	0.257	9.052	0.214	18.359
0.01	3	0.318	10.373	0.192	21.117	0.142	40.515
0.015	4.5	0.286	19.162	0.169	36.196	0.12	66.471
0.02	6	0.265	30.353	0.157	54.289	0.109	96.224
0.025	7.5	0.25	43.945	0.148	75.395	0.102	129.776
0.03	9	0.238	59.939	0.142	99.515	0.098	167.127
0.035	10.5	0.229	78.334	0.137	126.648	0.094	208.275
0.04	12	0.221	99.132	0.133	156.795	0.091	253.223

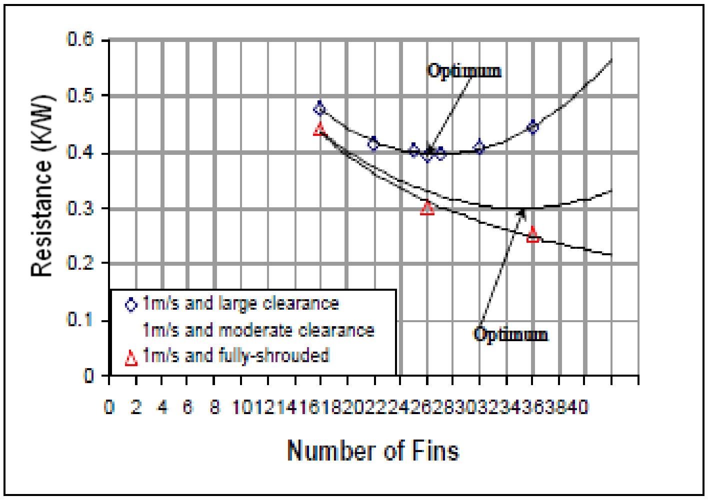

Figure 32. Thermal resistance vs. fin density for Bar-Cohen's three shrouding cases experiencing 1 m/s horizontal cross-flow [95].

Copeland focused on minimizing the thermal resistance of extruded heat sinks in horizontal cross-flow by empirically studying the effect of fin thickness and fin pitch. The results varied based on the set of operating conditions, which was specified by fixing the approach velocity, pressure drop, or fan power. Copeland also studied heat sink performance by fixing the thermal resistance and determining the operating conditions necessary for the heat sink to achieve it. For some cases, the optimal heat sink dimensions were not feasible based on manufacturing limitations at the time [81, 96].

Babus'Haq et al. studied cross-flow of a shrouded extruded fin heat sink, as shown in Figure 33. For the range of variables used, the optimal inter-fin spacing had only a very slight dependence on both the flow velocity and the shroud-gap-to-fin-height ratio. The optimal spacing was 2.0 ± .1 mm for duralumin, and 4.1 ± .1 mm for mild steel. Although the research group analyzed the relationship between velocity and pressure drop, they did not develop a relationship between the thermal performance and the pressure drop [97].

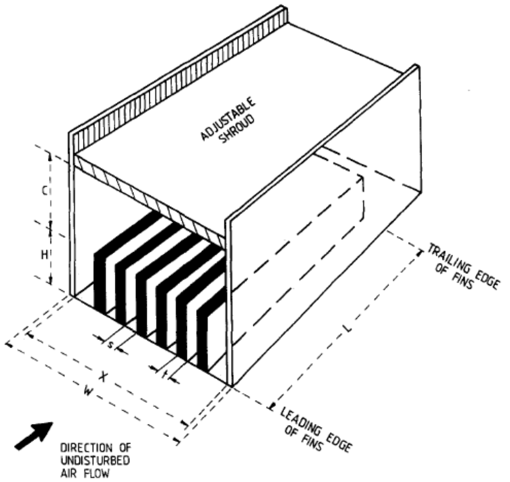

Figure 33. Shrouded extruded fin heat sink experiencing horizontal cross-flow [97].

Naik et al. did a similar study as Babus'Haq, although for the turbulent regime. The optimal fin spacing highly depended on both the fin-height-to-length ratio and the Reynolds number, although shroud clearance had little effect. Their correlation for the optimum spacing (s_{opt}), although they did not consider the pressure drop, was:

$$\left(\frac{s_{\text{opt}}}{H}\right) = .0359\left(\frac{H}{L}\right)^{-.642} \text{Re}^{.023} \tag{15}$$

Equation (15) is valid for $.085 \le H/L \le .36$ and $.39 \le s/H \le .6$ and $13 \le L/s \le 107$ and $0 \le C/H \le 1$ and $3.1\text{E}^3 \le \text{Re} \le 3.4\text{E}^4$. Variable C represents the shroud clearance [98].

El-Sayed et al. also analyzed turbulent horizontal flow through extruded fins, although they studied shrouds without side walls. They too neglected the required pressure drop as they derived their equation for the mean Nusselt number:

$$\text{Nu}_{\text{m}} = 5.734146\left(\frac{W}{L}\right)^{.214171}\left(\frac{H}{W}\right)^{-.36263}\left(\frac{t}{W}\right)^{.15250885}\left(\text{Re}_{\text{L}}\right)^{.42422} \tag{16}$$

Equation (16) is valid for $24{,}649 \le \text{Re}_{\text{L}} \le 189{,}462$ and $3\text{mm} \le t \le 9\text{mm}$ and $23\text{mm} \le H \le 92\text{mm}$ and $10\text{mm} \le W \le 42\text{mm}$ and $L = 150\text{mm}$ [99].

3.4.3 Cylindrical Pin Fins

Khan et al.'s data in Table 4 shows that while the thermal resistance for staggered cylindrical pin fins was approximately half of that for the in-line arrangement in the same horizontal cross-flow pattern, the pressure drop of the staggered heat sink was about three times as much [100]. Kim and Webb reported that the optimal fin diameter and fin pitch of in-line cylinders in cross-flow are 1.85 mm and 3.6 mm respectively. Their in-line formation had a slightly lower thermal resistance than their staggered arrangement, which had an optimal fin diameter and fin pitch of 3.25 mm and 5.9 mm respectively [92].

Table 4. Thermal resistance and pressure drop of shrouded cylindrical pin fin heat sink with in-line vs. staggered arrangement in horizontal cross-flow [100].

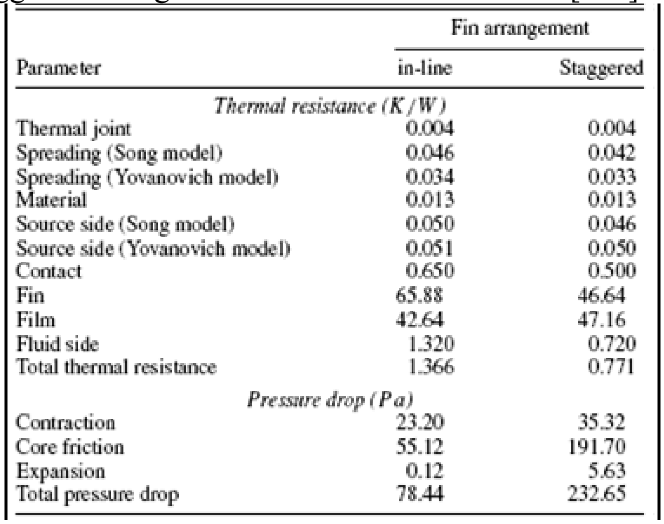

Parameter	Fin arrangement	
	in-line	Staggered
Thermal resistance (K/W)		
Thermal joint	0.004	0.004
Spreading (Song model)	0.046	0.042
Spreading (Yovanovich model)	0.034	0.033
Material	0.013	0.013
Source side (Song model)	0.050	0.046
Source side (Yovanovich model)	0.051	0.050
Contact	0.650	0.500
Fin	65.88	46.64
Film	42.64	47.16
Fluid side	1.320	0.720
Total thermal resistance	1.366	0.771
Pressure drop (Pa)		
Contraction	23.20	35.32
Core friction	55.12	191.70
Expansion	0.12	5.63
Total pressure drop	78.44	232.65

Azar and Mandrone found that the thermal resistance of unshrouded cylindrical pin fin heat sinks is a strong function of the cross-flow's velocity. Furthermore, the heat transfer coefficient experiences an asymptotic behavior in relation to the velocity [101]. They were able to find optimal pin fin densities for natural convection and two cross-flows, as exemplified in Figure 34.

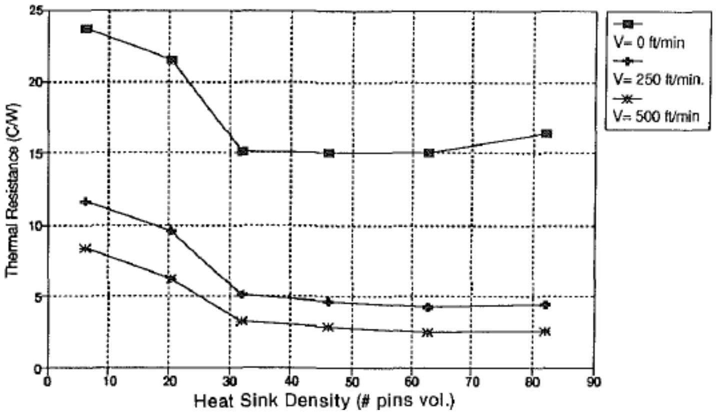

Figure 34. Thermal resistance vs. fin density for a cylindrical pin fin heat sink experiencing horizontal cross-flow or natural convection [101].

Babus'Haq et al. studied forced convection cross-flow of a shrouded cylindrical pin fin heat sink, as shown in Figure 35. The optimal pin spacing-to-diameter ratio in the span-wise direction was found to be 1.04, while the optimal ratio for the stream-wise direction highly depends on the pin alignment and the material's thermal conductivity. The latter ratio is .58 for an in-line arrangement of Duralumin pins. For staggered arrangements, the correlation developed to find the ratio was [102]:

$$\frac{S_{y,\,opt}}{d} = .59 + (.0667 * e^{.01k}) \tag{17}$$

The devised heat transfer correlation for this type of heat sink is given by Equation (18), in which *X* is the span-wise base width and *L* is the stream-wise base length [103]:

$$Nu = .355\left(\frac{S_x}{X}\right)^{.0446}\left(\frac{S_y}{L}\right)^{.048}\mathrm{Re}^{.585} \tag{18}$$

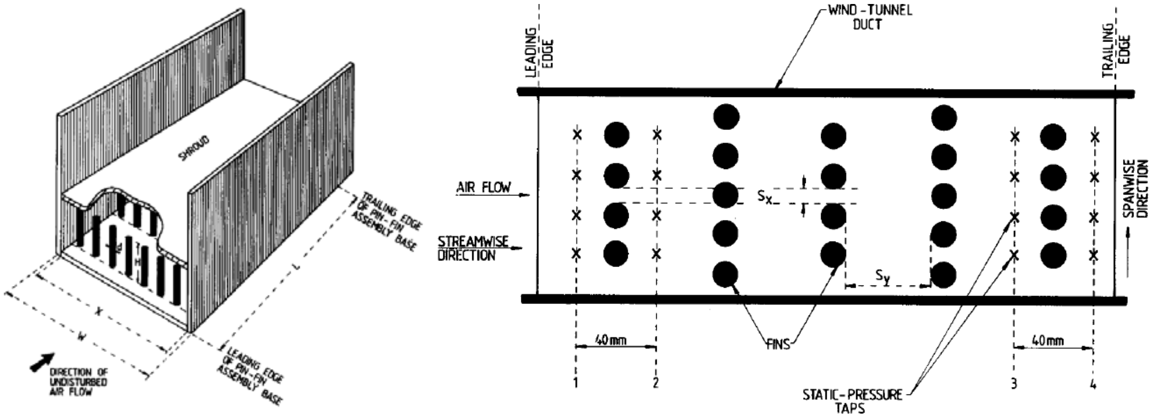

Figure 35. Shrouded cylindrical pin fin heat sink experiencing horizontal cross-flow created by Babus'Haq et al. [102, 103].

Moores and Joshi studied the tip clearance of water-cooled staggered cylindrical pin fins, as shown in Figure 36. By introducing tip clearance, the exposed area of the fin tips contributes to the heat transfer area, and flow vortices may cause a high local heat transfer rate there. For fin-height-to-fin-diameter ratios of .5, .8, and 1.1, the maximum heat transfer improvement was 23%, 19%, and 15% respectively, while the heat transfer area increase was 49%, 36%, and 27% respectively. When the clearance was made too big, flow bypass and lower channel velocities caused the heat transfer rate to decrease by up to 35%. The suggested clearance was less than 10% of the pin fin height [104].

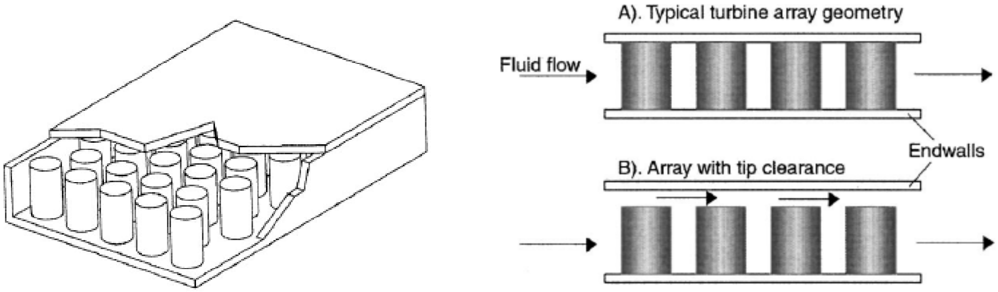

Figure 36. Shrouded cylindrical pin fin arrangement experiencing horizontal cross-flow, with and without tip clearance [104].

3.4.4 Square Pin Fins

Ryu et al.'s results in Table 5 were from a parametric study of square pin fin heat sinks in cross-flow of a square duct shroud with dimensions 101.43 x 101.43 mm. In the table, the lateral and longitudinal dimensions of the fins are represented by *a* and *b* respectively. Their data was developed into guidelines for designing shrouded heat sinks by minimizing the product of pumping power and thermal resistance, shown in Equation (21). They also proposed that exponents could be used on both of the multiplicands to allow the designer to designate the importance of each factor.

Table 5. Parametric analysis results for shrouded square pin fin heat sinks in horizontal cross-flow [105].

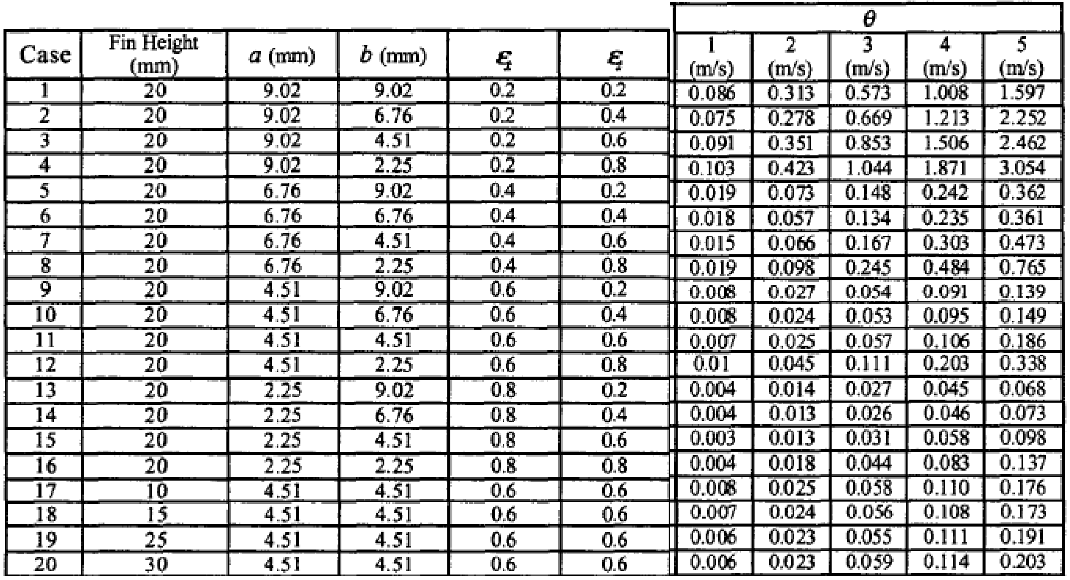

Case	Fin Height (mm)	*a* (mm)	*b* (mm)	ε_x	ε_z	θ				
						1 (m/s)	2 (m/s)	3 (m/s)	4 (m/s)	5 (m/s)
1	20	9.02	9.02	0.2	0.2	0.086	0.313	0.573	1.008	1.597
2	20	9.02	6.76	0.2	0.4	0.075	0.278	0.669	1.213	2.252
3	20	9.02	4.51	0.2	0.6	0.091	0.351	0.853	1.506	2.462
4	20	9.02	2.25	0.2	0.8	0.103	0.423	1.044	1.871	3.054
5	20	6.76	9.02	0.4	0.2	0.019	0.073	0.148	0.242	0.362
6	20	6.76	6.76	0.4	0.4	0.018	0.057	0.134	0.235	0.361
7	20	6.76	4.51	0.4	0.6	0.015	0.066	0.167	0.303	0.473
8	20	6.76	2.25	0.4	0.8	0.019	0.098	0.245	0.484	0.765
9	20	4.51	9.02	0.6	0.2	0.008	0.027	0.054	0.091	0.139
10	20	4.51	6.76	0.6	0.4	0.008	0.024	0.053	0.095	0.149
11	20	4.51	4.51	0.6	0.6	0.007	0.025	0.057	0.106	0.186
12	20	4.51	2.25	0.6	0.8	0.01	0.045	0.111	0.203	0.338
13	20	2.25	9.02	0.8	0.2	0.004	0.014	0.027	0.045	0.068
14	20	2.25	6.76	0.8	0.4	0.004	0.013	0.026	0.046	0.073
15	20	2.25	4.51	0.8	0.6	0.003	0.013	0.031	0.058	0.098
16	20	2.25	2.25	0.8	0.8	0.004	0.018	0.044	0.083	0.137
17	10	4.51	4.51	0.6	0.6	0.008	0.025	0.058	0.110	0.176
18	15	4.51	4.51	0.6	0.6	0.007	0.024	0.056	0.108	0.173
19	25	4.51	4.51	0.6	0.6	0.006	0.023	0.055	0.111	0.191
20	30	4.51	4.51	0.6	0.6	0.006	0.023	0.059	0.114	0.203

$$\varepsilon_x = 1 - \frac{\text{Fin width}}{\text{Fin pitch}} \tag{19}$$

$$\varepsilon_z = 1 - \frac{\text{Fin length}}{\text{Fin pitch}} \tag{20}$$

$$\theta = (\text{Pumping Power})(\text{Thermal Resistance}) \tag{21}$$

Dvinsky et al. determined that for cross-flow forced convection on a heat sink of square pin fins, the in-line arrangement was more thermally efficient than a staggered arrangement. The only exceptions that they observed were for some fully shrouded cases. Also, at higher velocities, the increased mixing reduced the difference in performance. Staggered arrangements had more active surface area (50% more on their pins and 20% more on their base) than in-line, but the required pressure drops were substantially higher. In cross-flow, in-line arrangements performed better, despite their high temperatures (and low heat transfer) in recirculation zones behind each pin [106].

Table 6. Thermodynamic performance of shrouded square pin fin heat sink with in-line vs. staggered arrangement for horizontal cross-flow and 25.4 mm shroud clearance [106].

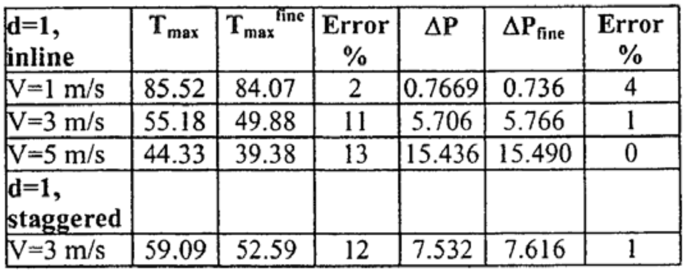

d=1, inline	T_{max}	T_{max}^{fine}	Error %	ΔP	ΔP_{fine}	Error %
V=1 m/s	85.52	84.07	2	0.7669	0.736	4
V=3 m/s	55.18	49.88	11	5.706	5.766	1
V=5 m/s	44.33	39.38	13	15.436	15.490	0
d=1, staggered						
V=3 m/s	59.09	52.59	12	7.532	7.616	1

3.4.5 Rectangular Fins

While not many studies have been done on rectangular fins in cross-flow, Kim and Webb found that when staggered, they had less convective thermal resistance than in-line cylindrical pin fins, staggered cylindrical pin fins, and extruded rectangular fins. For staggered rectangular fins with a depth of 32.5 mm along the cross-flow, their suggested thickness and pitch was .85 mm and 2.85 mm respectively. However, this study failed to consider spreading resistance.

3.5 Vertical Cross-Flow and Natural Convection Enhancement

3.5.1 Extruded Fins

Toh and Leong reported that shrouded vertically-aligned extruded fin heat sinks, as shown in Figure 37, have Nusselt numbers between the limits of those of parallel plates and square ducts. Their equations for the Nusselt number and dimensionless distance (x^+) were [107]:

$$Nu = 2.3319(x^+)^{-.28486} \tag{22}$$

$$x^+ = \frac{\text{Fin Plate Height}}{\text{(Hydraulic Diameter)RePr}} \tag{23}$$

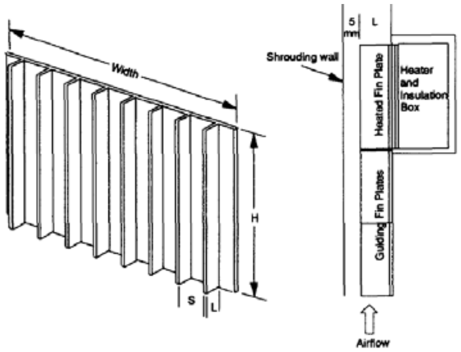

Figure 37. Vertically-aligned extruded fin heat sink with shroud wall [107].

Bejan found that for natural convection in vertical parallel plate channels, the optimal spacing is within 20% of:

$$\frac{\mathrm{D_{opt}}}{H} = 2.3\left[\frac{g * \beta * (\mathrm{T_{max}}\text{-}\mathrm{T_o}) * H^3}{\alpha * \nu}\right]^{-.25} \tag{24}$$

In Equation (24), β is the coefficient of thermal expansion, α is the thermal diffusivity, and ν is the kinematic viscosity [86].

Bejan also found that for natural convection in staggered vertical parallel plate channels, the optimal horizontal spacing is within 6% of:

$$\frac{\mathrm{D_{opt}}}{H} = 6.3\left(\frac{N * b}{H}\right)^{1.48} * \mathrm{Ra}_H^{\ -.19} \tag{25}$$

Equation (25) is valid for $10^3 \leq \mathrm{Ra}_H \leq 5\mathrm{E}^5$ and $0.4 \leq (N * b/H) \leq 1.2$ [86].

Yalcin et al. analyzed the impact of certain parameters on the natural convection heat flux per unit base area of a shrouded horizontal heat sink made of extruded fins, as shown in Figure 38. They observed an optimum heat flux when the fin spacing was 8 mm and the fin length was 127 mm, although this latter value was the minimum for that parameter. The optimum clearance was their maximum tested value of 100 mm, which corresponded to the maximum fin height of 50 mm [108].

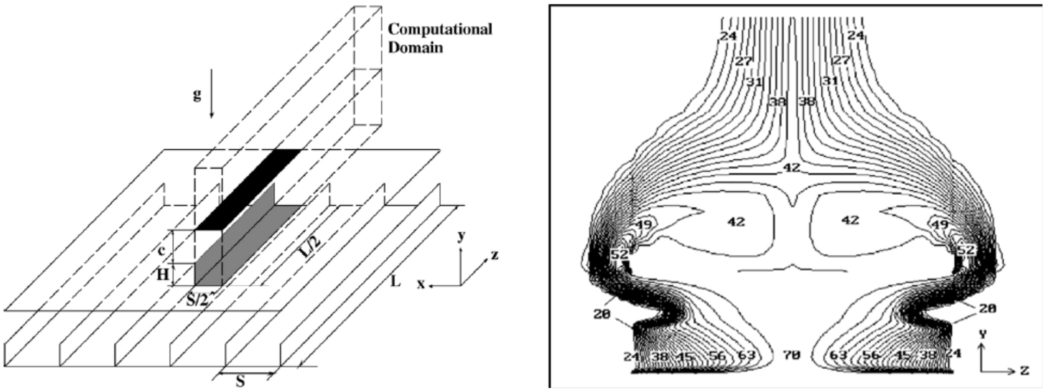

Figure 38. Extruded fin array decomposed into CFD domain, and a sample temperature contour for natural convection [108].

Cengel and Ngai reduced their heat sink's maximum temperature in natural convection by up to 20% by applying a shroud, as shown in Figure 39. Shrouding worked well when applied to sinks with long fins and wide spacing, and the biggest maximum temperature drop was from 120.6ºC to 105.5ºC for a shroud with a 25 mm clearance. However, shrouding was detrimental for sinks with closely spaced fins and increased the maximum temperature by up to 40%. Radiation was responsible for 20-50% of the heat transfer when no shroud was present, and only 8-20% of the heat transfer when a shroud was applied. Their data is shown in Table 7 [109].

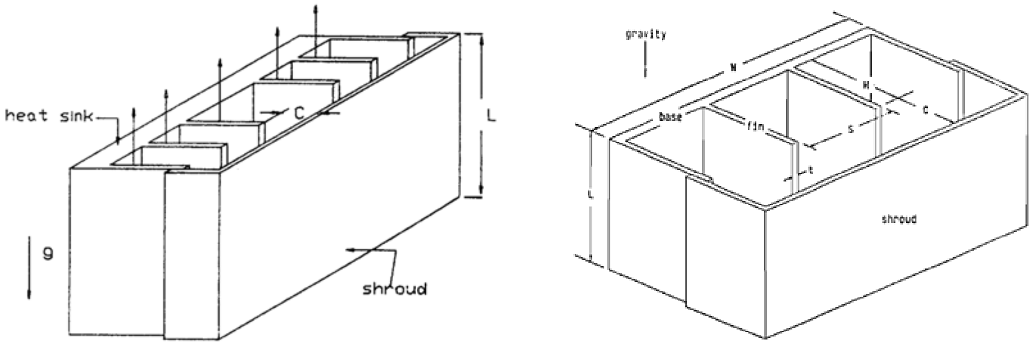

Figure 39. Vertically-aligned extruded fin heat sink with shroud [26, 109].

Table 7. Maximum temperature change from applying a shroud to extruded fin heat sinks experiencing vertical cross-flow [109].

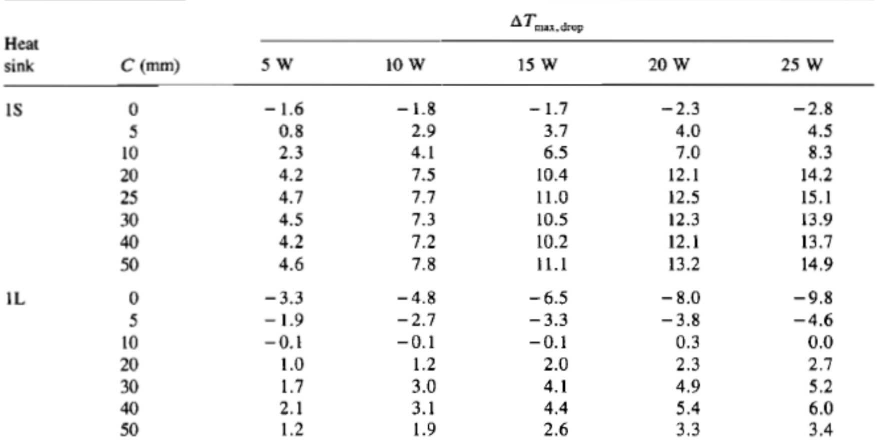

Heat sink	C (mm)	$\Delta T_{\mathrm{max,drop}}$				
		5 W	10 W	15 W	20 W	25 W
1S	0	−1.6	−1.8	−1.7	−2.3	−2.8
	5	0.8	2.9	3.7	4.0	4.5
	10	2.3	4.1	6.5	7.0	8.3
	20	4.2	7.5	10.4	12.1	14.2
	25	4.7	7.7	11.0	12.5	15.1
	30	4.5	7.3	10.5	12.3	13.9
	40	4.2	7.2	10.2	12.1	13.7
	50	4.6	7.8	11.1	13.2	14.9
1L	0	−3.3	−4.8	−6.5	−8.0	−9.8
	5	−1.9	−2.7	−3.3	−3.8	−4.6
	10	−0.1	−0.1	−0.1	0.3	0.0
	20	1.0	1.2	2.0	2.3	2.7
	30	1.7	3.0	4.1	4.9	5.2
	40	2.1	3.1	4.4	5.4	6.0
	50	1.2	1.9	2.6	3.3	3.4

Subsequent studies by Cengel and Zing showed a maximum temperature drop of 30ºC due to the shroud. For various heat sink geometries, the optimum shroud clearance was between .5 and 1.5 times the fin height. Once again the shroud diminished the baseline performance when placed to close to the heat sink [26].

Bhattacharya et al. performed a numerical analysis for geometry similar to Cengel and Ngai's, but with a simple plate shroud. The application of the shroud improved performance by up to 15% and decreased performance by as much as 10%, although their study neglected radiation. Heating the shroud helped performance and increased the optimum clearance, which varied depending on the fin geometry [110, 111].

Arik et al. varied the height of extruded fins for natural convection, as shown in Figure 40. It was noted that manufacturing standards dictate that the fin height-to-spacing ratio should not exceed 10:1. For the case in which fin height was 3 inches, converting the system into square pin fins resulted in an almost identical temperature. For the pin fins, the lower surface area was compensated for by the enhanced fluid circulation [31].

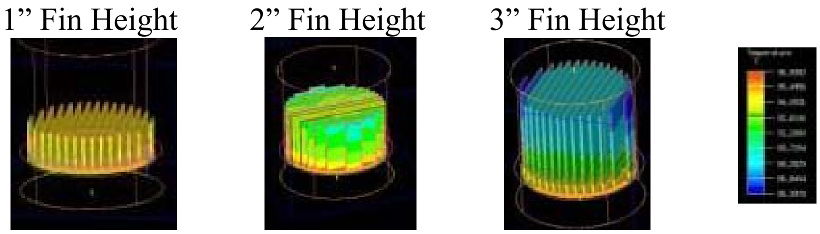

Figure 40. Variation of extruded fin thermal behavior in natural convection, based on fin height [31].

3.5.2 Cylindrical Pin Fins

Sparrow and Vemuri tested the natural convection of cylindrical pin fin heat sinks in three orientations. The sink with fins facing vertically upward performed the best, followed by the sink with horizontally-aligned fins, which was followed by the sink with fins facing vertically downward. Their calculations included radiation effects, which accounted for 25-40% of the heat transfer [112]. They also observed optimal fin densities (based on convection only) as shown in Figure 41.

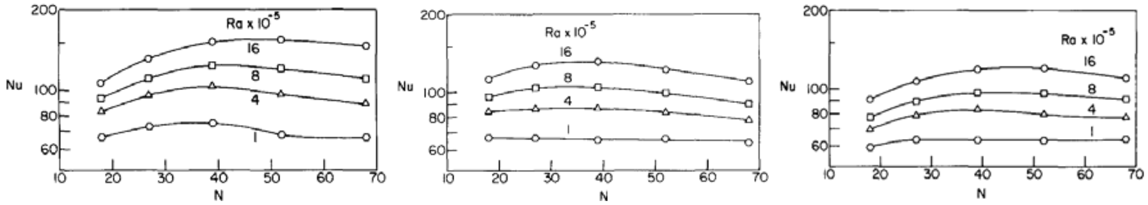

Figure 41. Nusselt number vs. fin number for various Rayleigh numbers of cylindrical pin fins facing: a) vertically upward b) horizontally c) vertically downward [112].

Bejan found that the optimal center-to-center spacing between staggered horizontal cylindrical pin fins in natural convection is within 2% of:

$$\frac{\mathrm{S_{opt}}}{H} = 2.72\left(\frac{H}{D}\right)^{1/12} \mathrm{Ra}_{H}^{-.25} + .263\frac{D}{H} \tag{26}$$

Equation (26) is valid for Pr =.72 and $350 \leq \mathrm{Ra}_D \leq 10^4$ and $6 \leq (H/D) \leq 20$. When vertical cross-flow was applied to the staggered horizontal cylindrical pin fin array, the optimal spacing became within 5.6% of:

$$\frac{\mathrm{S_{opt}}}{D} = 1.59\frac{\left(H/D\right)^{0.52}}{P^{0.13}\,\mathrm{Pr}^{0.24}} \tag{27}$$

P represents the dimensionless pressure drop. Equation (27) is valid for Pr =.72 and $10^4 \leq P \leq 10^8$ and $25 \leq (H/D) \leq 200$ [86].

Thrasher et al. found that tweaking the porosity of a chimney affects the buoyancy and thus the cooling power of shrouded heat sinks. For their natural convection studies, they concluded an optimal porosity of around 91 percent, although this value has an inverse relationship with the chimney height and the Reynolds number. They decreased the sink temperature rise by over 30% with the application of a 233 mm chimney [113].

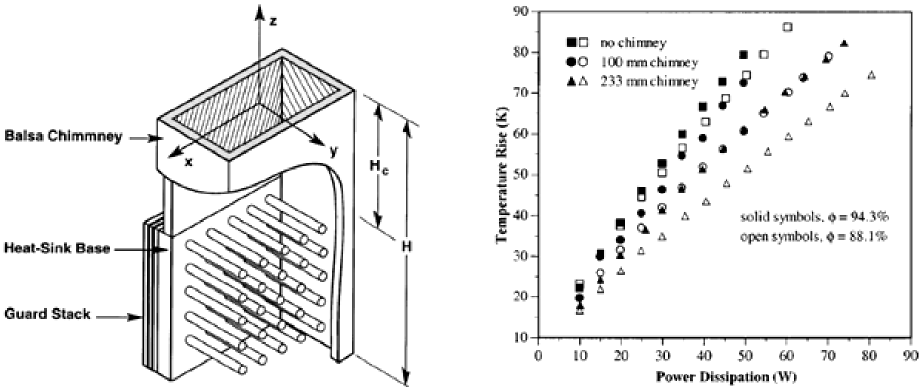

Figure 42. Thrasher et al.'s heat chimney configuration, and temperature rise above ambient for combinations of two porosities and three chimney heights [113].

3.5.3 Square Channels

Yazawa utilized the chimney effect by building vertical square channels along the side of a microelectronic device, as shown in Figure 43. The optimal gap width was 15.4 mm, and the natural convection heat dissipation went from 4.83 W to 18.9 W due to the vertical micro-channels [114].

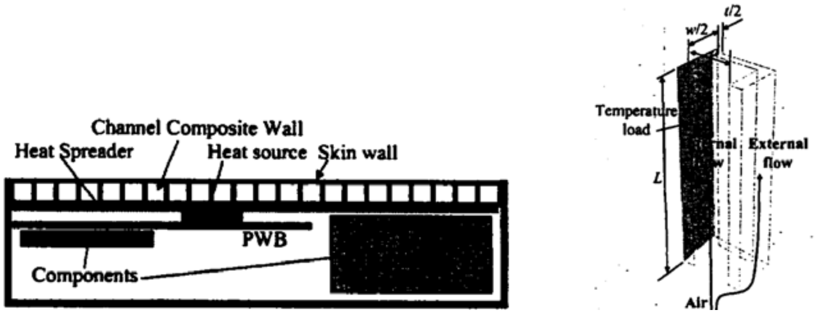

Figure 43. Top view of Yazawa's square channels and isometric view of computational domain for numerical analysis [114].

3.5.4 Rectangular Pin Fins

Guglielmini et al. applied a shroud to staggered vertical rectangular fins for natural convection, as shown in Figure 44. Their results included a Nusselt number variation of -10% to +12% compared to their baseline. They reported that radiation accounted for approximately 4% of the heat transfer. Depending on the fin arrangement, the optimum frontal wall spacing was between 25% – 50% of the fin length [115].

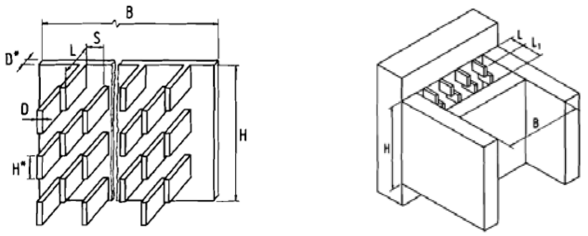

Figure 44. Vertically-aligned staggered rectangular fin heat sink with shroud [115].

3.5.5 Parallel Plate Shroud

Manca et al. augmented natural convection by applying a parallel plate as a shroud, and studied the effect of the orientation and spacing as shown in Figure 45. The maximum wall temperature increased as the angle was increased to 88 degrees from vertical, although the dependence of the wall temperature on the angle was slight from between 0 and 60 degrees. From 88 to 90 degrees, the maximum wall temperature slightly decreased. The optimum gap was found to be approximately 20.0 mm [116].

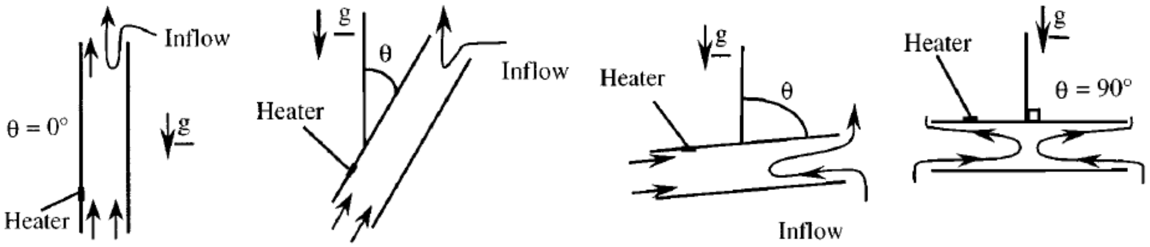

Figure 45. Free convection air inflow pattern altered by a plate shroud [116].

Hui et al. performed a similar study as Manca et al., except the range of angles was only 0-10º from horizontal, and the fluid was water. Natural convection increased as the angle increased, and was much more significant when the spacing between the parallel plates was small. The greatest Nusselt number increase was 50%, occurring at the maximum angle of 10º [117].

3.6 Radial Fins

Jian-Hui and Chun-Xin modified a fin array so that it nearly seamlessly accepted the exit velocity profile from the fan, as shown in Figure 46. Doing so prevented backflow in the fins, while adding surface area available for heat transfer. Thus, the required pressure drop of such an array was lowered, and the thermal resistance was reduced by 15.9% to a value of 0.323 K/W. For their parameters, the maximum temperature reduced from 350 K to 342 K. They reported the thermal resistance of various geometries as shown in Figure 46, although the thermal performance vs. pressure drop was not charted [118].

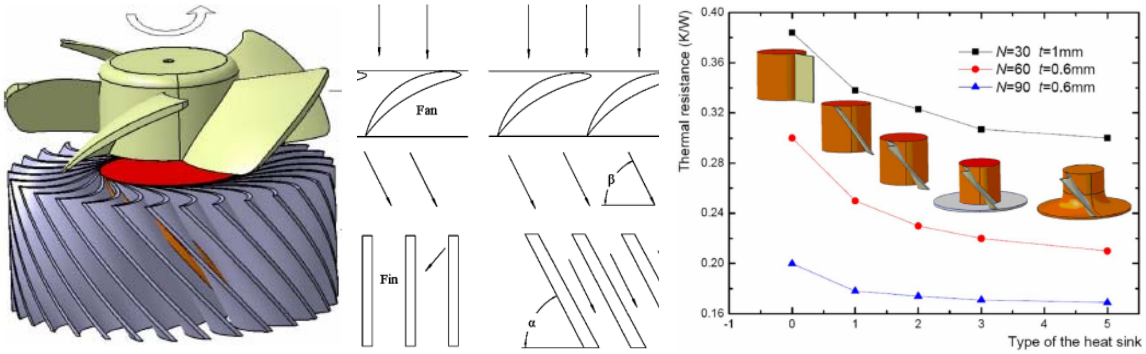

Figure 46. Streamlined radial fin array, schematic of flow visualization, and chart of thermal resistances for five radial fin schemes [118].

Jian-Hui and Chun-Xin stressed the importance of minimizing the entropy generation rate for the entire system. By operating the fan near its optimal point and having a properly designed heat sink, irreversibility in the system can be minimized. They claimed that this simultaneous consideration of thermal performance and pressure drop is essential for forced convection analyses.

Taufiq et al. optimized the forced convection of annular radial fins by minimizing the entropy generation rate. They also emphasized that there is an optimal Reynolds number for a given system that will minimize the entropy. In their case, the optimal Reynolds number was around 50 for laminar flow and approximately 4300 for turbulent flow. They achieved a fin array efficiency of .9999 with the optimal dimensions of 3.44 mm fin thickness, 17.2 mm base radius, and 34.4 mm tip radius [119].

Almogbel and Bejan optimized the cylindrical radial pin fins in Figure 47 by minimizing the system's thermal resistance for a fixed amount of solid volume. Their findings revealed that a set of tapered fins had a thermal resistance of about 60% of the baseline, although manufacturing issues could be troublesome with the optimized geometry. For $140 < \mathrm{Re}_{Do} < 14{,}000$ the optimal x-axis spacing was found to be [120]:

$$\frac{\mathrm{S_{opt}}}{D_o} = 1.7\,\mathrm{Pr}^{-.24}\left(\frac{H}{D_o}\right)^{.52}\mathrm{Re}^{-.26} \qquad (28)$$

Heggs and Ooi established a procedure for rating or designing annular fins based on the fin performance ratio, which is a measure of the fin effectiveness rather than its thermal performance [121]. Radial fins have even been applied to cylinders to enhance boiling heat transfer [122]. These studies are represented in Figure 48.

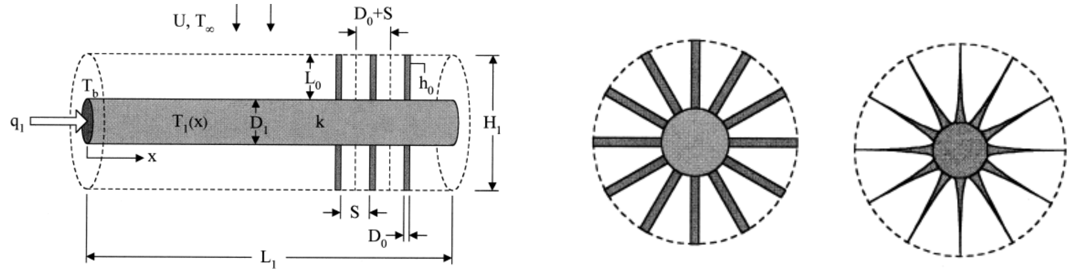

Figure 47. Radial cylindrical pin fins in cross-flow, shown with original and optimized cross-sections [120].

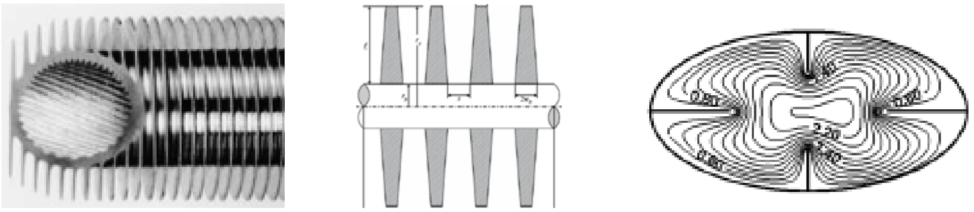

Figure 48. Various radial fin geometries common in research literature [121-123].

Papadopoulos and Hatzikonstantinou were able to enhance the forced convection heat transfer of flow in an elliptical duct (Figure 48c) by implementing radial fins starting from the duct wall and approaching the center. Large fins improved the Nusselt number by up to 300%, although there was no quantitative analysis of the pressure drop [123].

Rahnama and Farhadi studied the natural convection of various arrangements of rectangular radial fins placed in between two concentric cylinders. For every configuration they studied, the Nusselt number decreased due to the presence of the radial fins [124].

Heindel et al. used radial fins in submerged jet cooling to increase the surface area by a factor of five and to reduce the thermal resistance over three-fold. Their system used fluorocarbon liquid FC-77 and is shown in Figure 49. The minimum resistance of 0.4 cm^{2}K/W occurred when the shroud diameter was 22.23 mm, the flow rate was 7.5 l/min, and both the nozzle diameter and nozzle-to-sink distance were 4.42 mm [125].

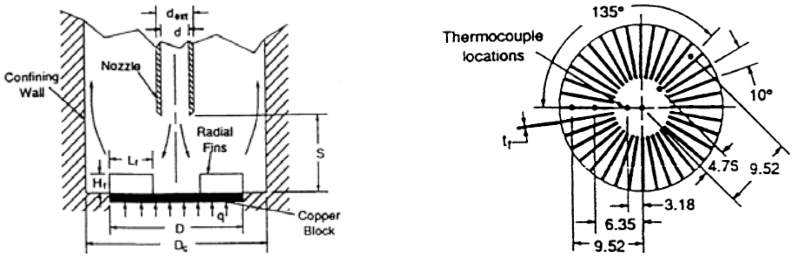

Figure 49. Submerged jet cooling configuration with radial fins [125].

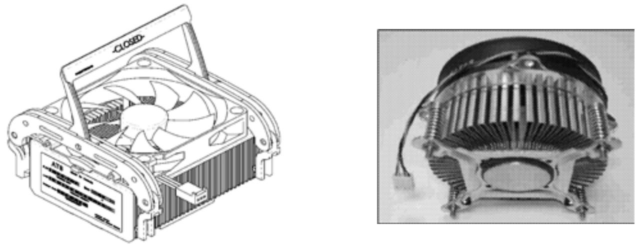

Figure 50. Conventional folded fin heat sink vs. radial folded fin sink [126].

Dehoff et al. engineered radial folded fin heat sink designs to obtain thermal resistances below 0.3 ºC/W in a very small form factor. Along with volumetric concerns, their parameter assignments took into consideration weight and cost. The optimum values for the fin thickness, fin number, and center core diameter were 0.4 mm, 104, and 33 mm respectively. The 4% thermal performance increase of using copper instead of aluminum did not justify the extra cost and weight of copper. Their prototype is shown in Figure 50, along with a schematic of the precursor to these types of heat sinks [126].

Chang et al. mapped out the Nusselt number spatial distribution within curved radial fins, as shown in Figure 51. The focus was to optimize the fin-length-to-hydraulic-diameter ratio (L/D) for preset cross-sectional fin geometry. Their optimal ratios are provided in Equations (29)–(31), although there was no consideration of pressure drop or spreading resistance [127].

$$\left(\frac{L}{D}\right)_{Optimal} = 18.89 - (.0032\,\mathrm{Re}) \qquad \text{for Re} \le 1{,}200 \tag{29}$$

$$\left(\frac{L}{D}\right)_{Optimal} = 16.26 + (.0006\,\mathrm{Re}) \qquad \text{for } 2{,}000 \le \text{Re} \le 8{,}000 \tag{30}$$

$$\left(\frac{L}{D}\right)_{Optimal} = 17.8 + (.0007\,\mathrm{Re}) \qquad \text{for side exit only and } 500 \le \text{Re} \le 8{,}000 \tag{31}$$

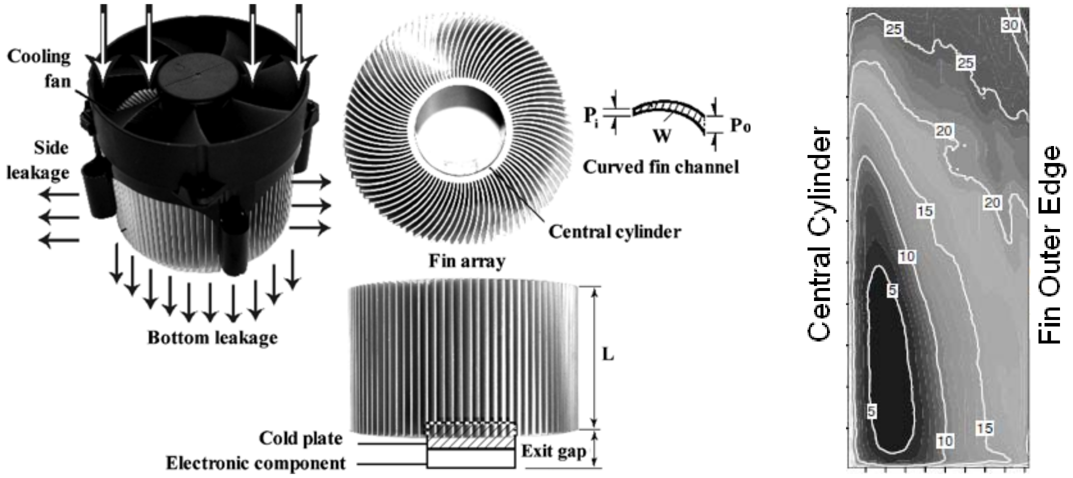

Figure 51. Chang's configuration and sample result of a fin geometry with the Nusselt number mapping imposed upon it [127].

Synthetic jets are a relatively new research field with much promise for efficient and effective active cooling. Studies have supported claims that synthetic jets are more reliable, quieter, and have smaller footprints than traditional fans. Commercial down-lighting LED modules with this technology applied to radial fins, as shown in Figure 52, are in production. The synthetic jets are designed to last as long as 100,000 hours, and they consume around 1.1 W. Cost remains a concern, as the price for these devices are between $10 and $20 [80, 86, 128-131].

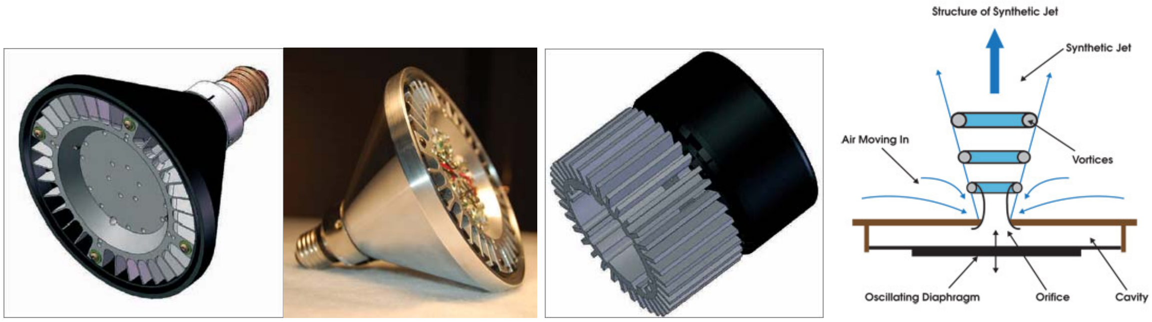

Figure 52. Commercial synthetic jet coolers with concept diagram [76, 128].

3.7 Summary

The interrelations of parameters and the thermal performance of shrouded heat sink systems highly depend on the type of flow. While the foundations of shroud applications spawned from natural convection enhancement, the consequence of radiation shielding may weaken free convection thermal dissipation. This has become more prevalent as surface coatings have been developed to boost radiation. The goal of shrouding for natural convection is to increase buoyancy forces, whereas the goal of shrouding for forced convection is to prevent flow bypass and improve the aerodynamics of the system. Because of increasingly high energy densities in modern electronics, engineers have begun focusing more on the active cooling of shrouded heat sinks.

Generally, a heat sink's thermal resistance decreases when the fin density, fin diameter, or imminent velocity is increased, although the required pressure drop is inherently linked to these parameters. Pin fins are usually an excellent choice for heat sinks due to their large ratio of surface area to volume. They are also basically insensitive to the flow path. It has been shown that the best cross-sectional shape for pin fins is generally cylindrical, although at high velocities an elliptical shape sometimes becomes preferable [72, 100, 132]. Aluminum alloy AA2024, also known as duralumin, was the most popular heat sink material used by the reviewed researchers.

The optimization methodology for forced convection shrouded heat sinks needs to consider the energy input, and thus should consider required pumping power and minimizing the entropy generation. Thermodynamic optimization remains the first step in revealing trends in the design space and understanding the opportunities for performance improvements.

CHAPTER 4

COMPUTER MODELING PROCEDURE

4.1 Purpose

Chapter 3 has provided an overview of shroud studies and radial fin research, from which there are several opportunities for unique contributions. Because of the multitude of possible shrouded heat sink configurations, there is a plethora of cases that could be parametrically studied. The research herein pertained to the goal of engineering a suitable heat sink system for the restrictive design constraints of general down-lighting applications. Specifically, this study analyzed various configurations of shrouded heat sinks to determine which would be the most effective for the active cooling of down-lighting LED systems.

Both the heat loads and the geometrical scale were chosen with consideration to high power solid-state lighting arrays. The shroud frames were pyramidal, square, conical, or cylindrical, while the heat sinks consisted of square pin fins, straight radial fins, curved radial fins, or a combination of them. Like many of the forced convection studies reviewed in Chapter 3, this study used a computational fluid dynamics (CFD) program, neglected radiation heat transfer, and neglected the thermal dependence of the fluid's density.

Although shroud applications primarily originated for natural convection enhancement, the focus has been shifting to utilizing shrouds for active cooling. This was in response to the steady increase of power densities in microelectronics, such as high power LED systems. In turn, active cooling studies should relate the thermal performance to the required energy input, which was a task unfulfilled by most of the reviewed publications. Another flaw in many of the previous contributions was the failure to consider the entire system's thermal resistance. This study included these two issues as primary components of the research goals.

4.2 Software and Governing Equations

FLUENT 6.3.26 was the CFD program used for this study. It utilized the finite volume method after importing the mesh from other software. GAMBIT 2.4.6 was the program chosen for the geometric modeling and mesh generation. To run GAMBIT, a remote session was initiated by utilizing the PC X server X-Win32 9.0. Both FLUENT and GAMBIT are produced by ANSYS, Inc.

The governing equations of mass, momentum, and energy were solved by FLUENT. Equation (32) is the conservation of mass equation, also known as the continuity equation:

$$\frac{\partial \rho}{\partial t} + \nabla \cdot \left(\rho \vec{\upsilon} \right) = S_m \tag{32}$$

Equation (33) is the conservation of momentum equation, with Equation (34) expressing the stress tensor within Equation (33):

$$\frac{\partial}{\partial t}(\rho \vec{\upsilon}) + \nabla \cdot (\rho \vec{\upsilon} \vec{\upsilon}) = -\nabla P + \nabla \cdot \left(\overset{=}{\tau} \right) + \rho \vec{g} + \vec{F} \tag{33}$$

$$\overset{=}{\tau} = \mu \left[\left(\nabla \vec{\upsilon} + \nabla \vec{\upsilon}^{\mathrm{T}} \right) - \frac{2}{3} \nabla \cdot \vec{\upsilon} I \right] \tag{34}$$

Equation (35) is the energy equation:

$$\frac{\partial}{\partial t}(\rho E) + \nabla \cdot \left(k_{\mathrm{eff}} \nabla T - \sum_{\mathrm{j}} h_{\mathrm{j}} \vec{J}_{\mathrm{j}} + \left(\overset{=}{\tau}_{\mathrm{eff}} \cdot \vec{\upsilon} \right) \right) + S_h \tag{35}$$

4.3 Modeling Assumptions

This study solved for the long-term steady state solutions. Radiation heat transfer was neglected, which is suitable for most forced convection analyses [133]. For both the heat sink material and the air, the properties of thermal conductivity, density, and specific heat were considered to be constant. The air's viscosity was also set as a constant. These material properties are listed in Table 8. All heat generated by the heat source volume was assumed to travel through the heat sink, which was done by applying adiabatic boundaries to all but one surface of the heat source.

Table 8. Constant solid and fluid properties used in this study.

Material	**Density (kg/m^3)**	**Specific Heat (J/kg*K)**	**Conductivity (W/m*K)**	**Viscosity (kg/m*s)**
Aluminum	2719	871	202.4	---
Copper	8978	381	387.6	---
Air	1.225	1006.43	0.0242	1.7894×10^{-5}

This numerical analysis used a laminar solver, which was checked for sufficiency during post-processing. For almost every case in this study, the velocity was less than 10 m/s, and subsequent cell Reynolds number studies verified the applicability of the laminar assumption. For this research, the stipulation was that the Reynolds number be under 10,000. Geometries with small inlet areas created high velocities, although they were kept below 17.5 m/s. These high-velocity simulations may have some small error associated with them, because neglecting the influence of turbulence would under predict the heat transfer performance.

4.4 Pre-Processing Procedure

4.4.1 Geometry Creation

The initial heat sink geometry was inspired by a commercial product, a schematic of which is shown in Figure 53. Its inter-fin spacing and fin dimensions are similar to those of “optimum” performance from various publications [86, 87, 92, 102]. The only fixed aspect of the entire system’s geometry was the heat source, which was arbitrarily set as a 40 x 40 x 5.08 mm block after benchmarking high power LED devices. This heat source was attached to the center of the heat sinks, as shown in Figure 54. Volumetric energy generation was applied, such that the heat source created 25, 35, 50 or 75 W of power as desired. These heat loads are a reasonable range for those expected from high power LED light arrays. The interface connecting the heat source and the heat sink was where the area-weighted average of temperature was reported.

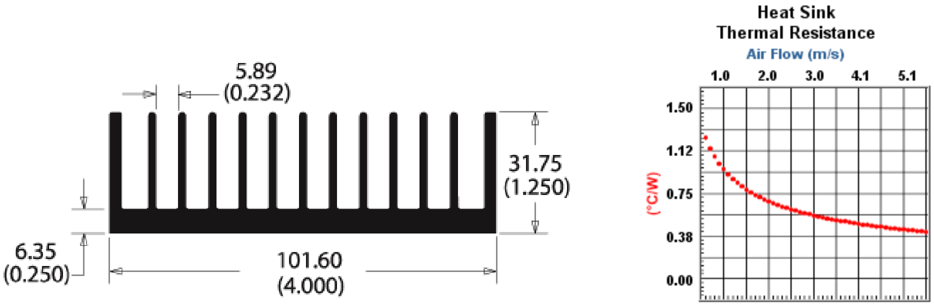

Figure 53. Commercial heat sink geometry and its general thermal resistance [134].

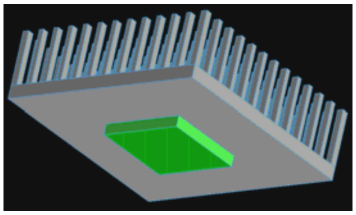

Figure 54. Baseline heat sink geometry, with green-colored heat source attached.

With the available computing power, it was necessary to utilize quarter-symmetry so FLUENT would be able to execute the simulations. Figure 55 shows the various shrouded heat sink configurations considered. All shrouds were 3.5mm-thick and 100mm-tall, except those for Progression 6 which were shortened to as low as 10mm-tall.

Progression 1 had the pin fin square heat sink from Figure 53 initially in a pyramidal shroud. The velocity inlet area at the top of the shroud was iteratively increased until the shroud became a rectangular channel.

Progressions 2–4 had identical conical shroud iterations up to becoming a cylindrical channel. Progression 2 analyzed a pin fin circular sink, Progression 3 considered a circular sink with straight radial fins, and Progression 4 studied a circular sink with both pin fins and straight radial fins.

Progression 5 had a circular sink with both pin fins and curved radial fins. Lastly, Progression 6 was a more in-depth analysis of circular sinks with only straight radial fins.

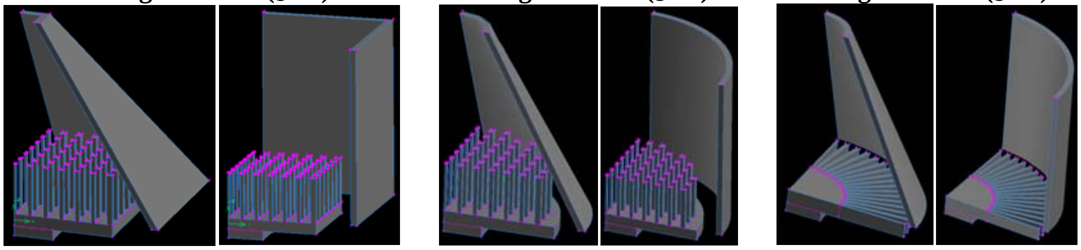

Progression 1 (§5.2) **Progression 2 (§5.3)** **Progression 3 (§5.4)**

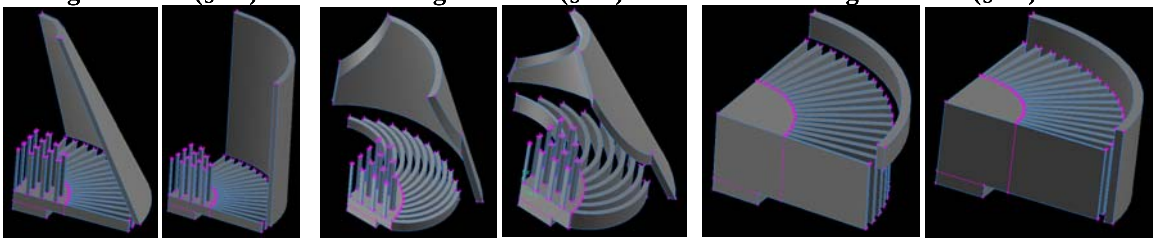

Progression 4 (§5.5) **Progression 5 (§5.6)** **Progression 6 (§5.7)**

Figure 55. Each progression's heat sink geometry shown with two sample shrouds.

The heat sink's convective surface area was an important characteristic to consider when comparing progressions. As shown in Table 9, the total surface areas for Progressions 2–5 were maintained within 0.3% of each other, and the effort to do so dictated geometrical dimensions. Progression 1 had over 15% more surface area than Progressions 2–5 , and yet generally had worse performance.

The central heat sink core of Progressions 3–7 had a radius of 30 mm, chosen to minimize the core diameter and to create radial fins in a manner that would keep the surface area consistent with the previous set of runs. The straight radial fin dimensions for Progression 3 were 37.72 x 7.855 x 2.25 mm, and for Progression 4 were 37.72 x 6.35 x 2.25 mm. For Progression 5, heat sinks with twelve 6.35mm-thick curved radial fins or eight 10mm-thick curved radial fins were experimented with. For Progression 6, the surface area was no longer held constant.

Table 9. Heat sink quarter-geometry surface area for all progressions.

Section	Progression	Heat Sink Description	Heat Sink Surface Area (mm^2)	
			Total	Just Top/Sides
5.2	1	Pin Fin Square	15,616	13,435
5.3	2	Pin Fin Circular	13,543	11,283
5.4	3	Straight Radial Circular Sink	13,580	11,916
5.5	4	Radial and Pin Fin Circular Sink	13,579	11,972
5.6	5a	6.35mm Thick Curved Radial	13,341	11,728
	5b	10mm Thick Curved Radial	13,341	12,094
5.7	6a	7.855mm Thick Radial	13,580	11,916
	6b	11mm Thick Radial	17,525	16,878
	6c	14mm Thick Radial	21,287	20,641
	6d	17mm Thick Radial	25,050	24,404
	6e	20mm Thick Radial	28,812	28,166
	6f	23mm Thick Radial	32,575	31,929
	6g	26mm Thick Radial	36,336	35,690
	6h	29mm Thick Radial	40,100	39,454
	6i	20mm Thick, 40mm Radius Core	23,103	21,249
	6j	20mm Thick, No Gap	31,071	29,107

To simulate the shrouded heat sink sitting in free space, the domain size was made large enough so that virtually all activity occurred within the bounds. This was later verified by analyzing vector images and checking mass and heat fluxes at the boundaries. Before meshing, it was confirmed that the geometry was properly created by ensuring that all volumes were ‘real’ and appropriately connected.

4.4.2 Mesh Creation

Due to large domains and intricate geometries, creating the meshes in GAMBIT was constantly challenged by the need to keep the number of elements low enough for FLUENT to run. The largest number of elements in a successful run was 2,122,353. Element sizes were kept small near the main area of activity, and sizing functions were used to grow the element size as they got further from the area of interest. Volumes with an attached sizing function were limited to tetrahedron or hybrid elements. Thus, hexahedron elements were used only for the heat source and square heat sink. The ‘examine mesh’ tool was utilized to gauge the mesh quality and ensure that the EquiSize Skew distribution was suitable, and mesh refinement was later performed in FLUENT. An example of a mesh created for this study is provided in Figure 56.

4.4.3 Boundary and Continuum Assignments

Boundary types were specified in GAMBIT to facilitate boundary condition implementation and post-processing in FLUENT. The symmetry condition provided adiabatic walls with full slip condition and allowed quarter-geometry modeling. Exterior domain walls were assigned as pressure inlets, fluid-solid interfaces were given the “wall” boundary, and the velocity inlet was designated. The continuum type of either fluid or solid was given to every volume. The mesh was then exported from GAMBIT.

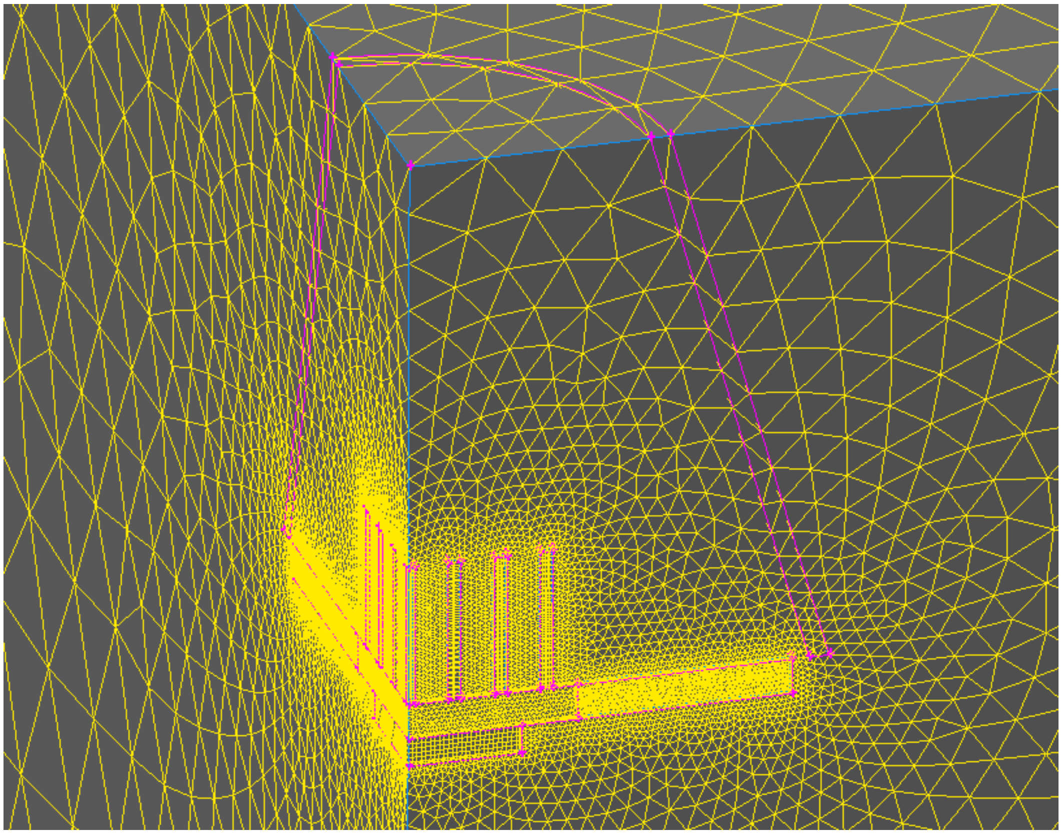

Figure 56. Sample mesh created for this study.

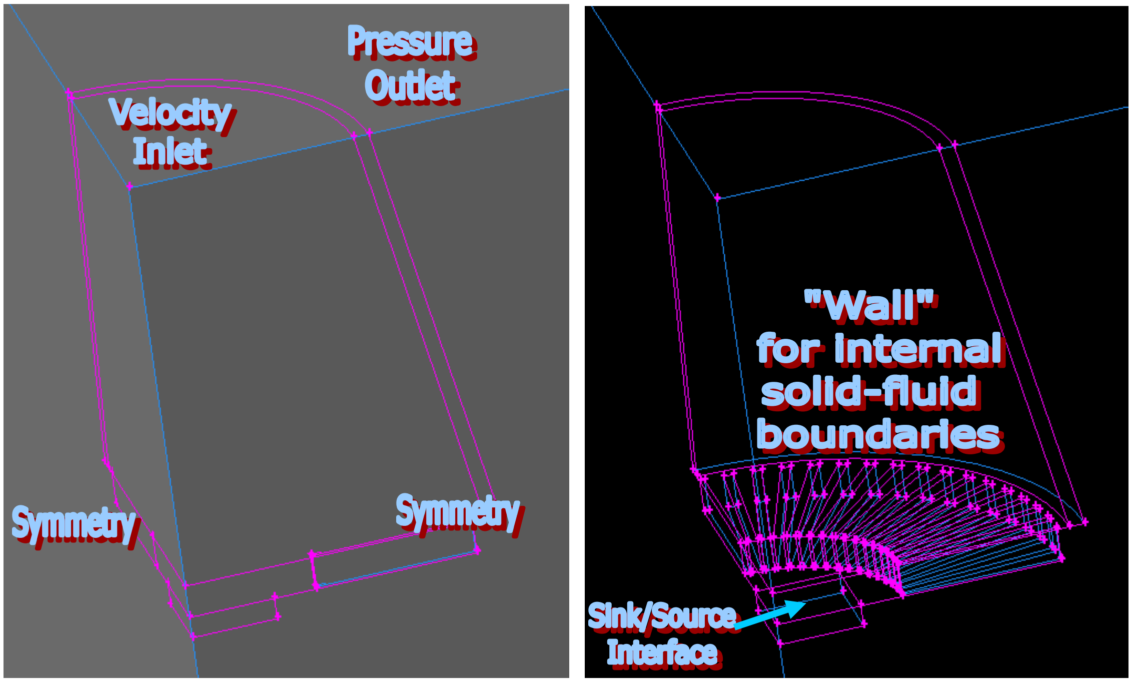

Figure 57. Boundary conditions overview.

4.5 FLUENT Simulation Procedure

4.5.1 Mesh Import, Refinement, and Scaling

Upon opening FLUENT (3D Full Simulation Mode), the mesh was imported. First, the ‘check grid’ tool was used to substantiate that the geometry and mesh were appropriately created. Grid refinement was then executed by using the ‘smooth/swap’ tools with the skewness method. Because the geometry was created in millimeters, the ‘scale’ tool was employed to adjust the units to meters.

4.5.2 Defining Models, Materials, Operating Conditions, and Boundary Conditions

The ‘solver’ submenu was given the setting settings of 3D pressure based solver, implicit formulation, steady time, absolute velocity formulation, Green-Gauss node based gradient option, and superficial velocity porous formulation. Also in this submenu, the energy equation was activated and radiation was deactivated.

In the ‘materials’ submenu, continuum type and material properties were assigned to every volume. The working fluid was air, and all of the solid material was specified as aluminum unless otherwise specified, in which copper was modeled. For operating conditions, the ambient pressure was set to 101,325 Pa and gravity was deactivated.

Boundary conditions were assigned so that the heat source walls (except for the interface with the heat sink) were set as adiabatic. Also, the heat source volume was given its power density value, and the inlet velocity was designated. These two settings were the main user-input variables that were altered from run to run.

4.5.3 Solution Controls, Solution Limits, Monitor Set-up, and Initializing

The solution controls for both the flow and energy equations needed to be sufficient. The under-relaxation factors of pressure and momentum were set as 0.3, and 0.7 respectively. A standard discretization method was used for pressure, while momentum and energy were assigned second order upwind methods. SIMPLEC was chosen as the pressure-velocity coupling. The solution limits were kept at the default values, with absolute pressure ranging from 1 to $5\text{x}10^{10}$ Pa and static temperature ranging from 1 to 5000 K. Surface monitors were set up to observe the residuals, velocity inlet pressure drop, and the temperature at the interface between the heat sink and heat source. The latter two values were area-weighted averages. Solution initialization was the final pre-processing step, and it was done by choosing to compute from all zones.

4.5.4 Iteration and Convergence

In the ‘solve’ menu, the iterate command initiated the simulation. The iterative solving of FLUENT was converged when the residuals reached the acceptable values, shown in Table 10. For many of the cases studied, all five of the residuals converged to the specified values. However, for some intricate cases with steeper gradients, the continuity residual did not fully converge. The associated temperature error when this occurred was below ± 0.1 K, while the associated pressure error was below ± 0.25 Pa.

Table 10. Residual convergence values.

	Continuity	**X-velocity**	**Y-velocity**	**Z-velocity**	**Energy**
Absolute Criteria	.001	.001	.001	.001	$1\text{x}10^{-7}$

4.6 Validation Methods

Verifying CFD results was essential before drawing conclusions, establishing trends, and defining the optimum parameters for each run's fixed constraints. The validation process included checking residuals, energy balances, and momentum balances. Grid refinement studies were also utilized. In addition, there were a few other ways that results were corroborated as sensible.

Energy and momentum balances were analyzed to ensure that boundary conditions were properly enforced. The energy balance at the interface between the heat source and heat sink verified that the desired power was implemented. Momentum balances were used to verify the volumetric flow rate and that the domain was big enough to simulate a system sitting in free space.

Grid refinement studies were used to ensure that the solution was mesh-independent, as well as to verify the minimum element resolution for meshing. This latter concern was significant due to the complex geometries and closely placed fins. Figure 58 shows the 1/64th geometry created to allow for the extremely dense packing of mesh elements. For the other part of the grid refinement study, two markedly different meshes for the same geometry were created, which was done by selecting different element geometries and different sizing functions. The solution dependency on the mesh and full residual convergence was between the values of ± 0.2 K and ± 0.5 Pa for temperature and pressure, respectively.

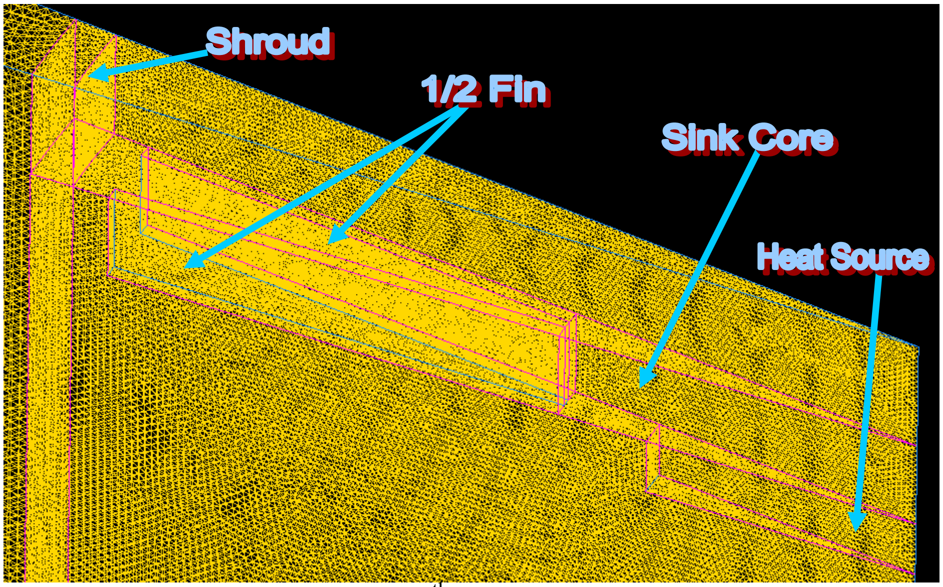

Figure 58. Grid refinement study of 1/64th of the geometry from Progression 3.

There were various methods used to check for sensible results. Contour and vector imaging allowed observations of the fundamental behavior of the system and helped to ensure that boundary conditions were properly enforced. Also, redundancy was utilized by the application of four different heat loads, as similar cases correctly had very comparable thermal resistances. This was expected since the simulations were one-way coupled systems. Lastly, correlations and results from literature and textbooks were used to help gauge the sensibility of the results.

CHAPTER 5

PARAMETRIC ANALYSES OF SHROUDED HEAT SINKS

5.1 Overview

The thermal performance and corresponding pumping power for the active cooling of shrouded LED-scale heat sinks have been accurately predicted in this chapter by utilizing the CFD modeling procedure and assumptions detailed in Chapter 4. Each section of §5.2 – §5.7 pertains to one progression of simulations designated for a specific heat sink geometry, as indicated in Figure 55. The geometry overview for this parametric study provided in §4.4.1 has been expanded upon within each progression's section in this chapter.

For the graphs in §5.2 – §5.7, 'temperature' refers to the area-weighted average temperature of the elements at the interface between the heat source and heat sink, as described in §4.4.1 and shown in Figure 54. To characterize the active cooling systems, this temperature was linked to the energy input, which was represented by the pumping power, calculated as the volumetric flow rate multiplied by the pressure drop at the velocity inlet. Thus, the overall system performance was defined as the interface temperature vs. pumping power. This relationship served as the most crucial criterion for these numerical analyses, because it coupled the overall system thermal performance with the energy requirement for the operating pressure.

Graphs of interface temperature vs. pressure drop, interface temperature vs. volumetric flow rate, and volumetric flow rate vs. pressure drop were used to further characterize the systems. Temperature contours and flow fields were also analyzed.

Minimizing an LED's junction temperature is realized by minimizing the system's total thermal resistance. Denoted by R_{th}, this value is represented by Equation (36) in which Q is the heat load, T_{max} is the maximum temperature, and T_{amb} is the ambient temperature:

$$R_{th} = \frac{T_{max} - T_{amb}}{Q} \quad [K/W] \tag{36}$$

Since all cases in this study had an ambient temperature of 300 K and each graph relates to a specific heat load, the charted trends of overall system performance are consistent with the trends of thermal resistance. Hence, the graphs of temperature vs. pumping power reflect how the heat sink systems compare to each other in terms of overall thermal conductance as well.

Temperature, rather than thermal resistance, was used in the graphs to convey an estimated solder TIM temperature for an LED source. Therefore, estimated die temperatures and the temperature differences between the various heat sinks may clearly be discerned from the graphs. The junction temperature may be significantly higher than the TIM temperature, although this depends on the package and its thermal resistance. For example, a 5W LED with a thermal resistance of 5 K/W would be 25 K above the TIM temperature.

In §5.8, comparisons are made between this study's various geometries. Also, the maximum thermal resistances of the heat sinks have been tabulated for the best-case shroud geometry of each progression. This data used the maximum temperature, which was found within the heat source volume and was approximately 0.5K – 1K above the average interface temperature.

5.2 Pin Fin Square Sink with Pyramidal or Square Shroud

Progression 1 entailed the pin fin square heat sink from Figure 53, initially with pyramidal Shroud 1. As shown in Figure 59, the velocity inlet area at the top of the shroud was iteratively increased until the shroud became Square Channel 1. Subsequently, the square channel cross-section was reduced to create Square Channels 2 and 3. The shroud dimensions for this progression's runs are shown in Table 11.

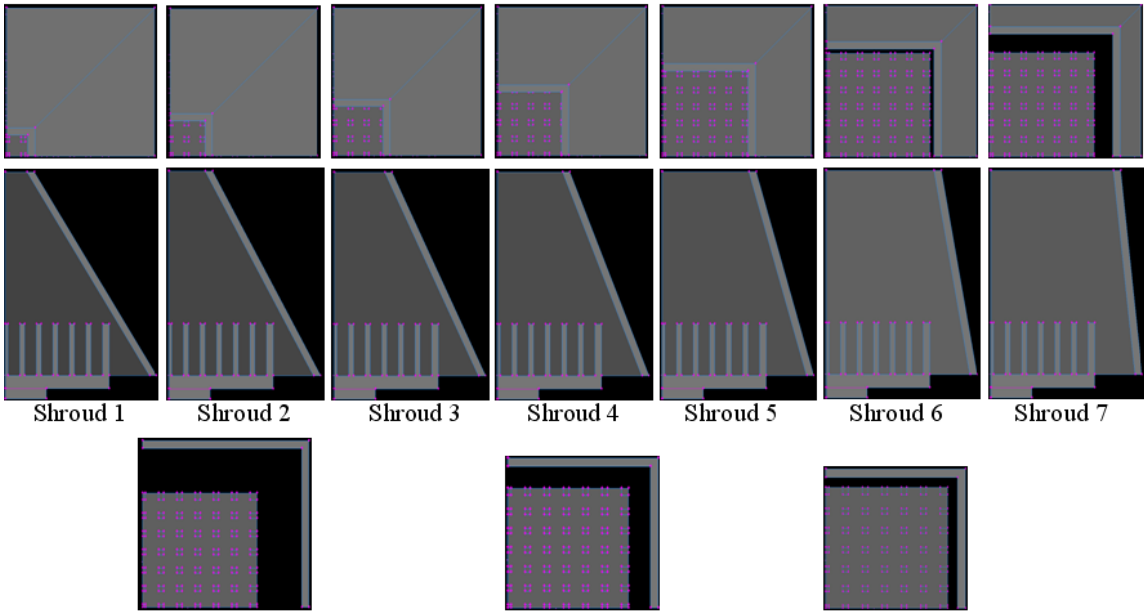

Shroud 1 Shroud 2 Shroud 3 Shroud 4 Shroud 5 Shroud 6 Shroud 7

Square Channel 1 Square Channel 2 Square Channel 3

Figure 59. Pin fin square heat sink in pyramidal shrouds and square channels.

Table 11. Shroud dimensions for Progression 1.

	Inlet dimensions (mm x mm)	Base dimensions (mm x mm)
Shroud 1	21.2 x 21.2	141.42 x 141.42
Shroud 2	35.35 x 35.35	141.42 x 141.42
Shroud 3	49.5 x 49.5	141.42 x 141.42
Shroud 4	63.64 x 63.64	141.42 x 141.42
Shroud 5	84.85 x 84.85	141.42 x 141.42
Shroud 6	106.1 x 106.1	141.42 x 141.42
Shroud 7	120.2 x 120.2	141.42 x 141.42
Square Channel 1	141.42 x 141.42	141.42 x 141.42
Square Channel 2	120 x 120	120 x 120
Square Channel 3	110 x 110	110 x 110

Figure 62 shows the overall system performance for Progression 1 with a 35 W heat load. For the smallest cross-sectional inlet area of Shroud 1, the interface temperature decreased from about 330 K to 318 K as the pumping power was increased from about 0.01 W to 0.80 W. As the inlet area was increased from Shroud 1 to Shroud 4, the temperatures were continually lower for a fixed pumping power, which signified a continual improvement in overall system performance. For Shroud 4, the interface temperature decreased from about 324 K to 313 K as the pumping power was increased from about 0.01 W to 4.30 W.

Increasing the cross-sectional inlet area from Shroud 4 to Square Channel 1 caused the system performance to decrease. For Square Channel 1, the interface temperature was about 330 K and 314 K for a pumping power of about 0.01 W and 5.20 W, respectively. As shown in Figure 61, reducing the channel's cross-section to Square Channels 2 increased performance, while further reducing the cross-section to Square Channel 3 reduced performance.

Shroud 4 was the best shroud geometry for Progression 1. With base dimensions of approximately 141 x 141 mm and inlet area dimensions of around 64 x 64 mm, the shroud slope had an acute angle of 71.8° between the horizontal plane and the shroud. For any fixed pumping power in the examined range, the temperature difference was less than 6 K.

Figure 62 shows the temperature vs. pressure performance for Progression 1 with a 35 W heat load, in which the impact of the shroud was more significant at smaller velocities. While this figure helps to characterize the system, it should not be mistaken for overall performance because pumping power must be considered as the energy input.

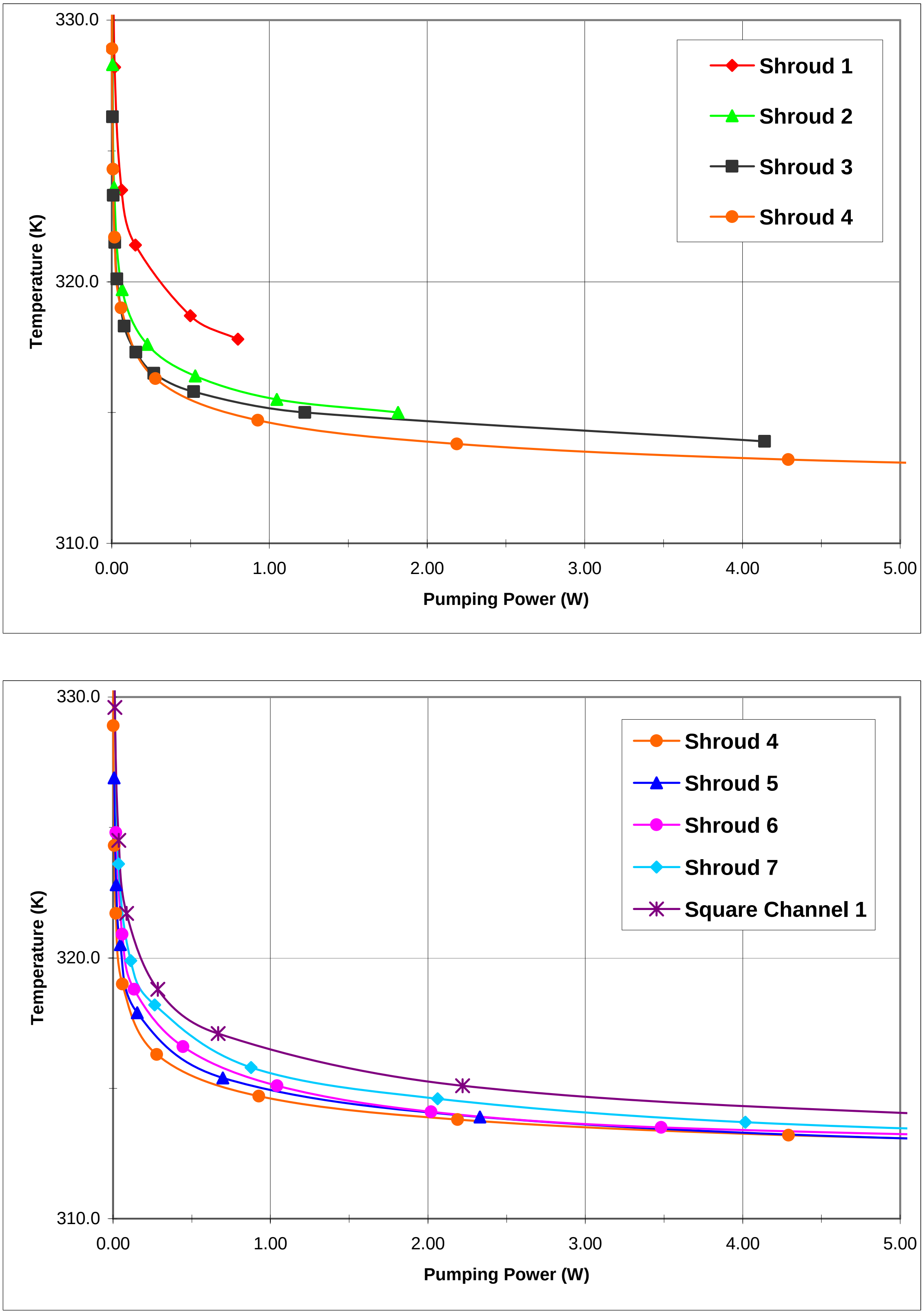

Figure 60. Source/sink interface temperature vs. pumping power for Progression 1 with a 35 W heat load.

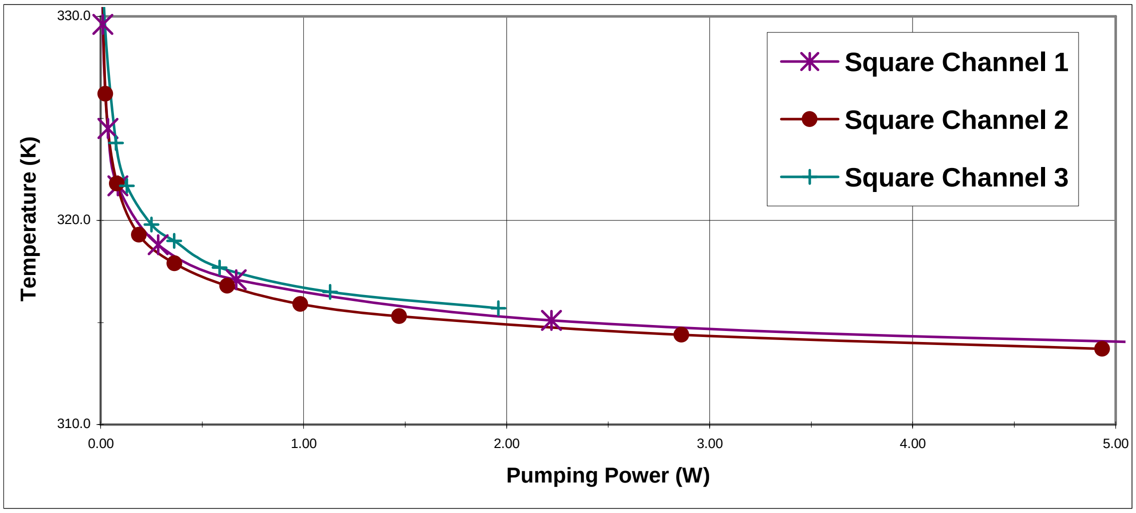

Figure 61. Source/sink interface temperature vs. pumping power for square channels of Progression 1 with a 35 W heat load.

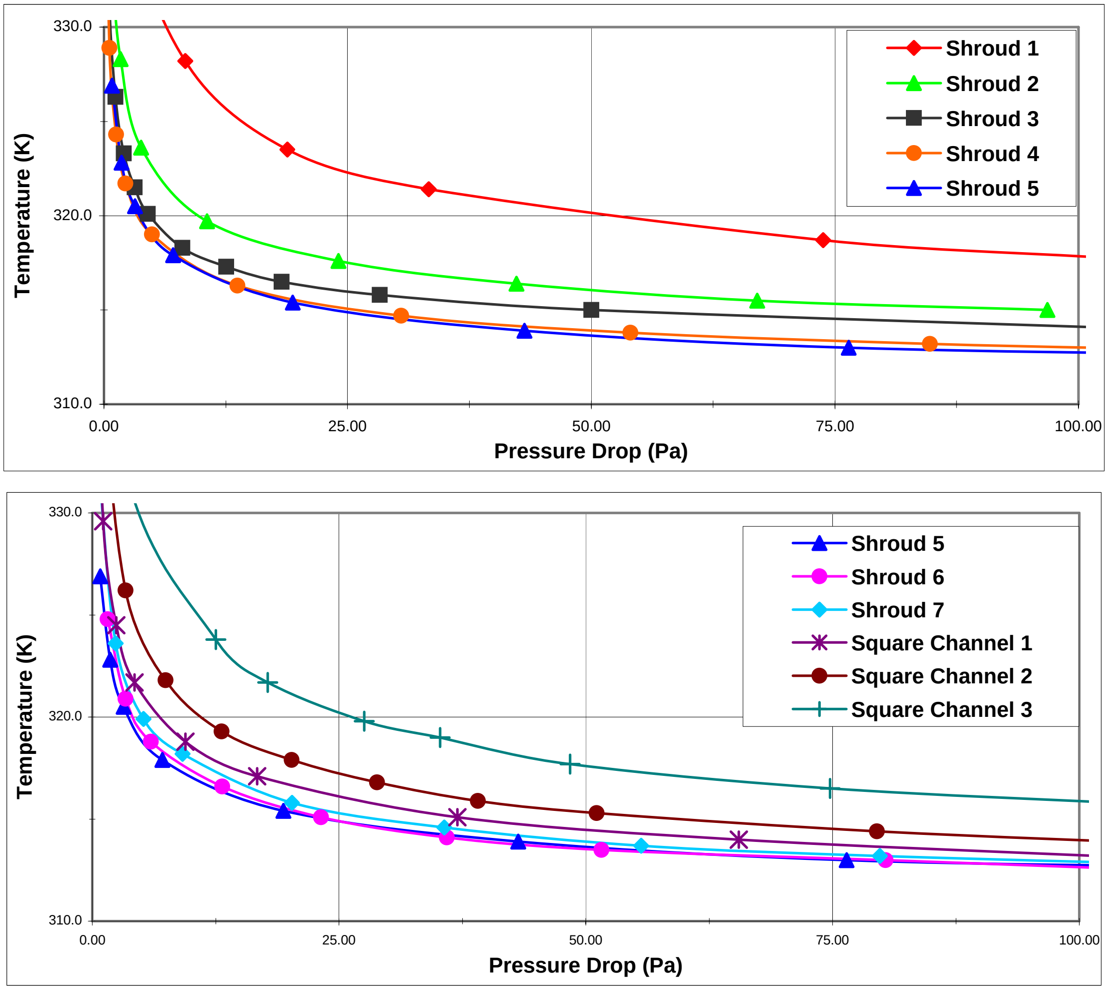

Figure 62. Progression 1 interface temperature vs. pressure drop for 35 W heat load.

Figure 63 shows the temperature vs. volumetric flow rate relationships. When the inlet area was small, the impinging velocity was focused at the central hottest part of the heat sink. Also, the flow velocity for a fixed volumetric flow rate is faster for a smaller inlet area. Thus, Shroud 1 had the best temperature vs. flow rate performance.

On the other hand, a small inlet cross-section restricted the volumetric flow rate for a given pressure drop, as shown by the relationships in Figure 64. Furthermore, Figure 65 shows flow fields for Shroud 1 and Shroud 4, with the former having a more tortuous path of impingement flow transformed into cross-flow which increased the pressure requirement. Also, the air heats up as it travels along the flow path, and a longer path degrades the thermal dissipation capability of the down-stream fins. Lastly, Shroud 1 did not experience flow recirculation on the bottom of the heat sink like Shroud 4 did. This was not as significant of a factor as first thought, since the heat transfer through the bottom of the heat sink for Shroud 4 was only about 2.5% of the thermal dissipation. The relatively evenly-distributed fluid flow of Shroud 4 utilized the pumping power well, as shown by the temperature contour in Figure 66.

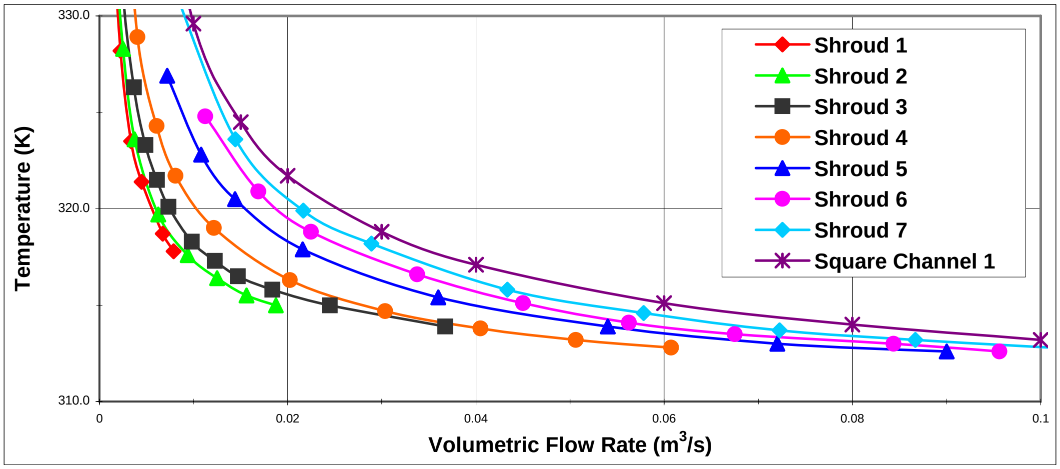

Figure 63. Source/sink interface temperature vs. inlet volumetric flow rate for Progression 1 with a 35 W heat load.

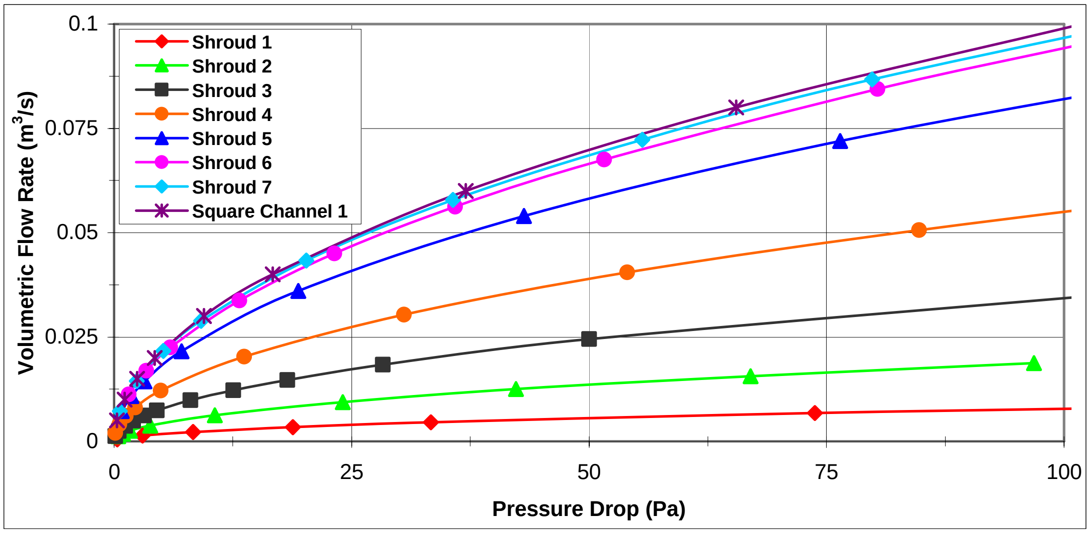

Figure 64. Inlet volumetric flow rate vs. inlet pressure drop for Progression 1.

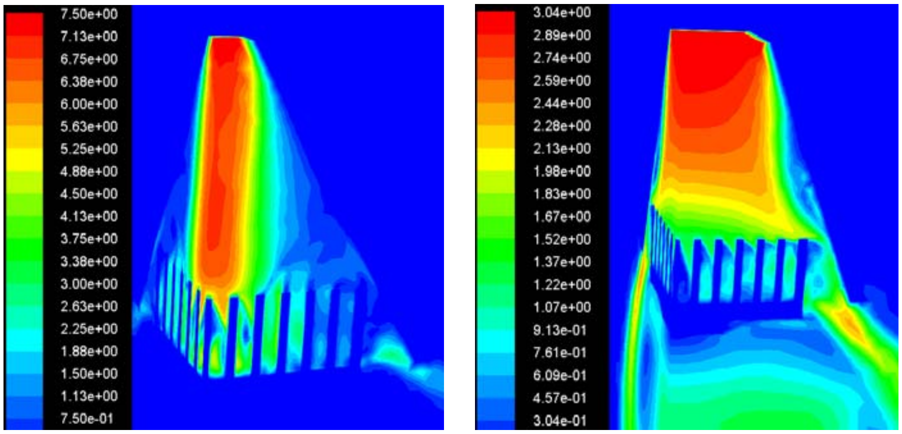

Figure 65. Velocity contours (m/s) for Shrouds 1 and 4 for 0.10 W pumping power.

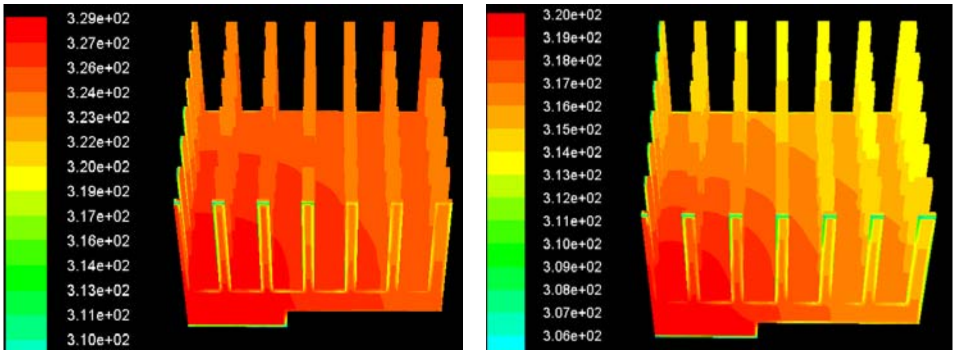

Figure 66. Temperature contours for Shrouds 1 and 4 for 35 W heat load and 0.10 W pumping power.

5.3 Pin Fin Circular Sink with Conical or Cylindrical Shroud

Progression 2 used a pin fin circular heat sink derived from the heat sink in Progression 1. The circular heat sink radius was 58.2 mm, and its number of fins in the quarter-symmetry geometry was reduced to 34.25 from the 42.25 on the square heat sink. The heat sink in Progression 2 had 86.7% of the surface area of that for Progression 1.

As shown in Figure 67, the velocity inlet area at the top of the conical Shroud 1C was iteratively increased until the shroud became Cylinder Channel 1. Subsequently, the channel cross-section was reduced to create Cylinder Channels 2 and 3. The shroud dimensions for this progression's runs are shown in Table 12.

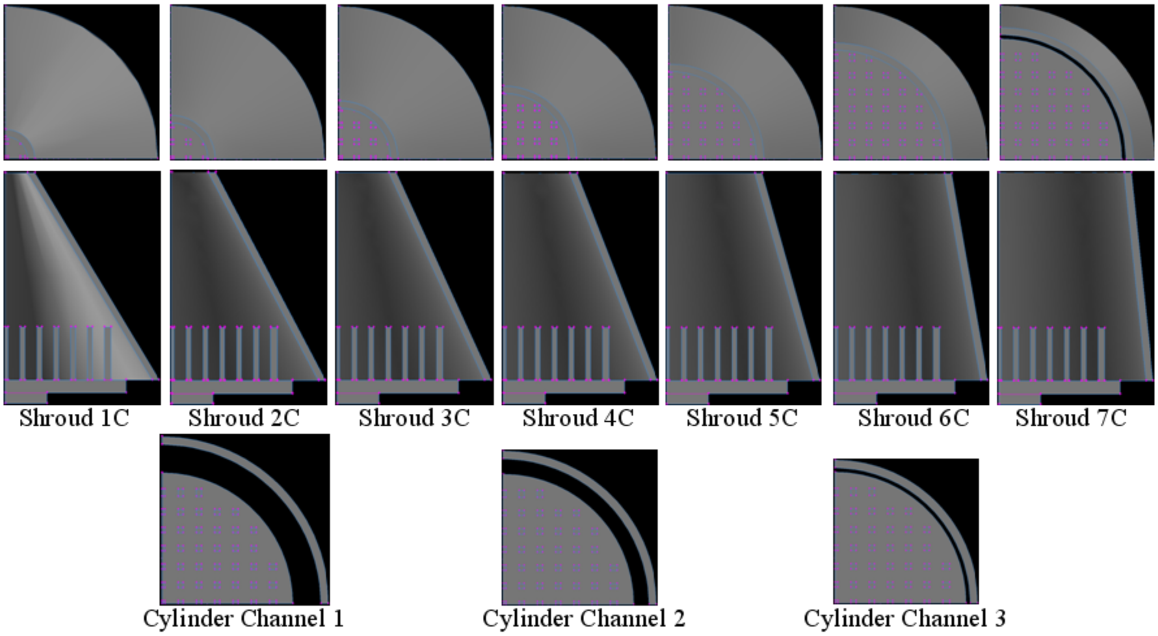

Shroud 1C Shroud 2C Shroud 3C Shroud 4C Shroud 5C Shroud 6C Shroud 7C

Cylinder Channel 1 Cylinder Channel 2 Cylinder Channel 3

Figure 67. Pin fin circular heat sink in conical shrouds and cylindrical channels.

Table 12. Shroud dimensions for Progression 2.

	Inlet radius (mm)	Base radius (mm)
Shroud 1C	10.6	70.71
Shroud 2C	17.675	70.71
Shroud 3C	24.75	70.71
Shroud 4C	31.82	70.71
Shroud 5C	42.425	70.71
Shroud 6C	53.05	70.71
Shroud 7C	60.1	70.71
Cylinder Channel 1	70.71	70.71
Cylinder Channel 2	65	65
Cylinder Channel 3	60	60

Figure 68 shows the overall system performance for Progression 2 with a 35 W heat load. For the smallest cross-sectional inlet area of Shroud 1C, the interface temperature decreased from about 335 K to 316 K as the pumping power was increased from about 0.01 W to 1.80 W. As the inlet area was increased from Shroud 1C to Shroud 3C, the temperatures were continually lower for a given pumping power, which signified a continual improvement in overall system performance. For Shroud 3C, the interface temperature decreased from about 324 K to 312 K as the pumping power was increased from about 0.01 W to 2.70 W. Increasing the cross-sectional inlet area from Shroud 3C to Cylinder Channel 1 worsened performance. For any fixed pumping power in the Shroud 1C – Cylinder Channel 1 range, the temperature difference was less than 7 K.

The reduced cross-sections of Cylinder Channels 2 and 3 further increased the temperature for a given pumping power. Shroud 3C was the best shroud geometry for Progression 2. With a base radius of approximately 71 mm and an inlet area radius of around 25 mm, that shroud slope had the acute angle of 65.3° between the horizontal plane and the shroud. For this progression, the interface temperature vs. pressure performance shown in Figure 69 mirrored that of the overall system performance.

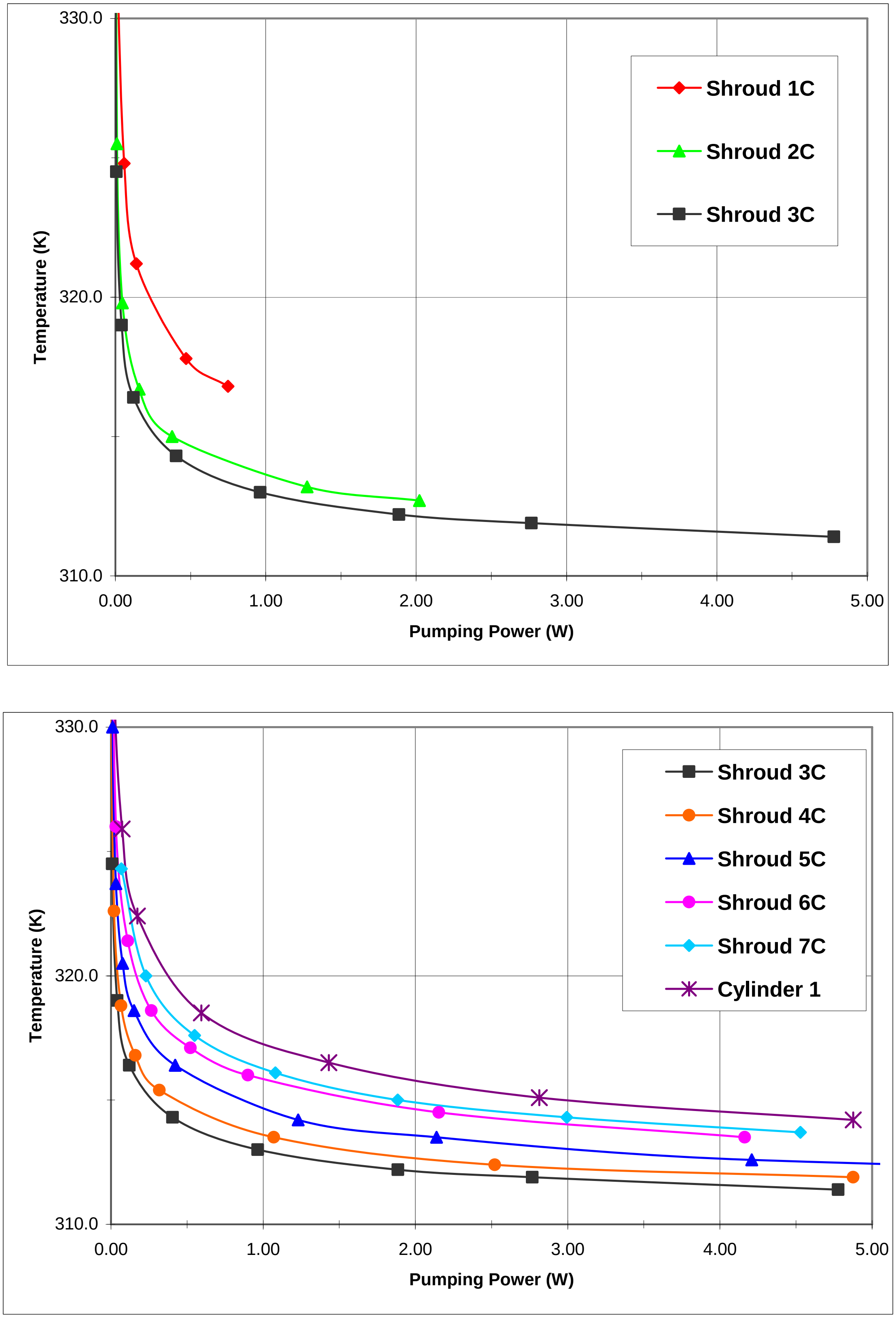

Figure 68. Source/sink interface temperature vs. pumping power for Progression 2 with a 35 W heat load.

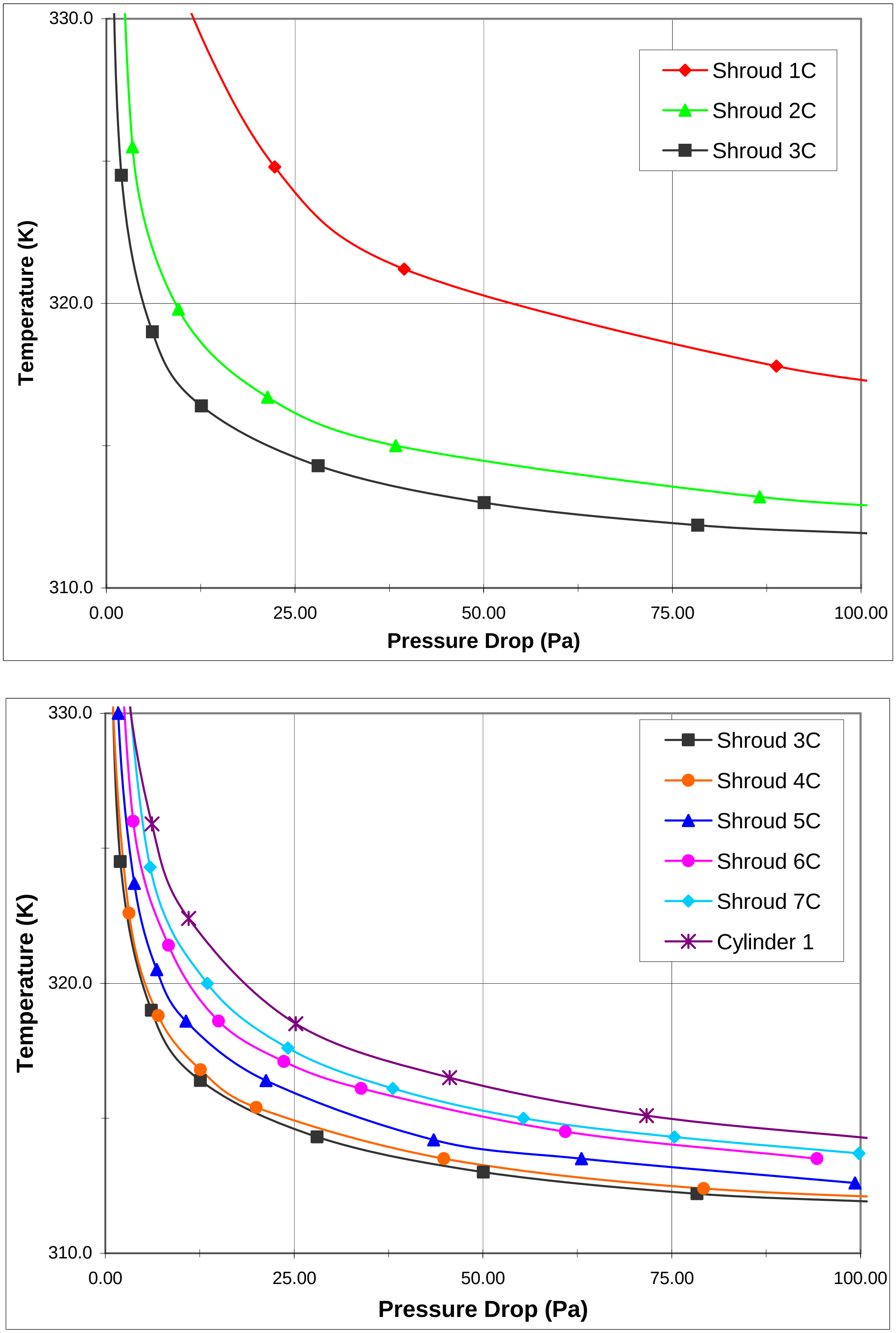

Figure 69. Source/Sink interface temperature vs. inlet pressure drop for Progression 2 with a 35 W heat load.

For Progression 2, Figure 70 shows the temperature vs. volumetric flow rate performances, while Figure 71 shows the volumetric flow rate vs. pressure drop relationships. The same system dynamics as described in Progression 1 occurred, in which increasing the inlet area caused the velocity and focused-flow effect to diminish but the volumetric flow rate for a given pressure drop to increase.

The flow fields for Shroud 1C and Shroud 3C are provided in Figure 72, with the former having a more tortuous path of impingement flow transformed into cross-flow which increased the pressure requirement. Also, the air heats up as it travels along the flow path, and a longer path degrades the thermal dissipation capability of the downstream fins. The relatively evenly-distributed fluid flow of Shroud 3C, which was imaged in an "unfilled" manner due to computational demand, utilized the heat sink well, as illustrated by the temperature contours in Figure 73.

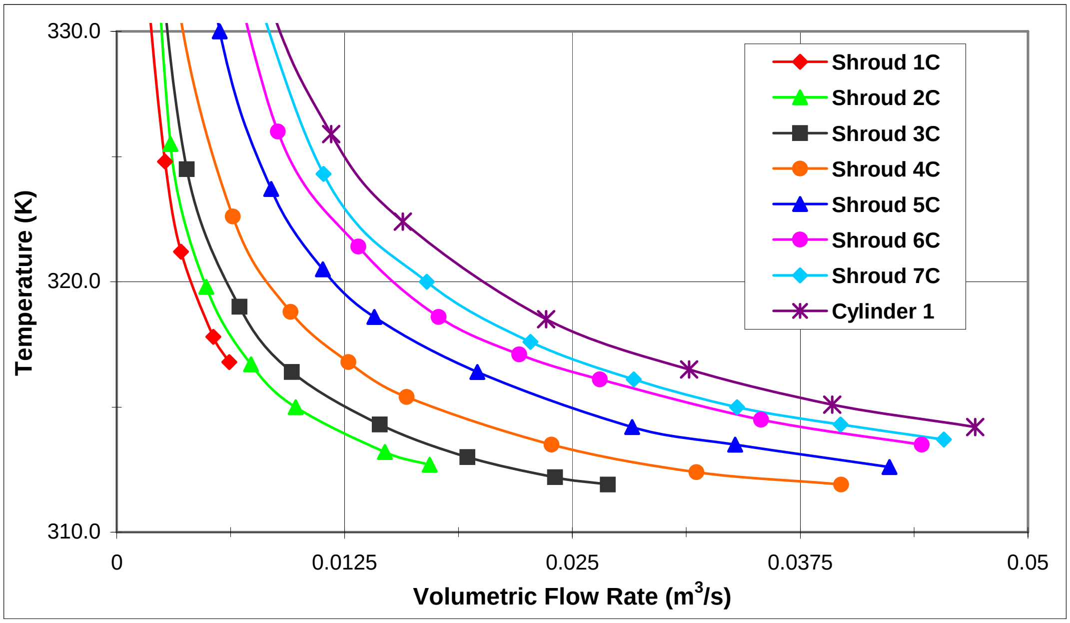

Figure 70. Source/sink interface temperature vs. inlet volumetric flow rate for Progression 2 with a 35 W heat load.

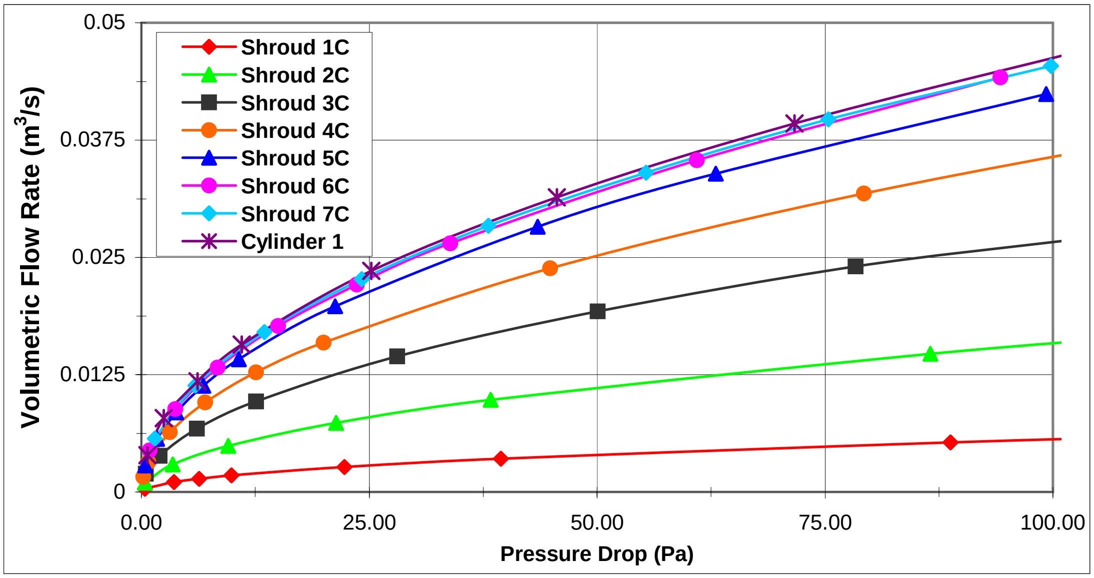

Figure 71. Inlet volumetric flow rate vs. inlet pressure drop for Progression 2.

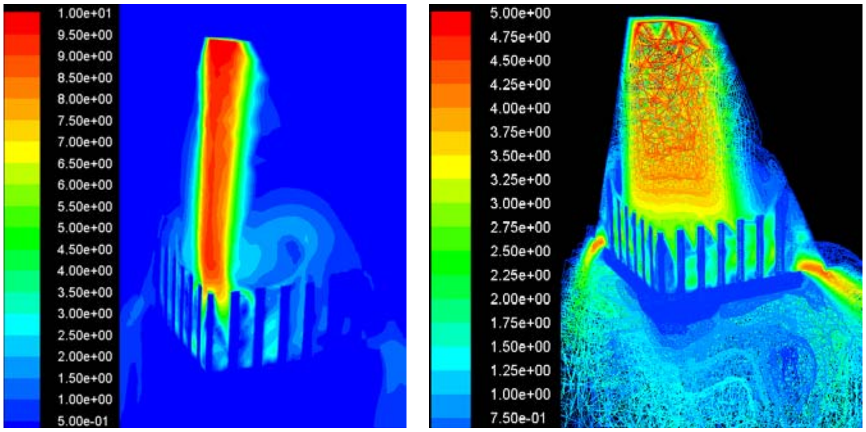

Figure 72. Velocity contours (m/s) for Shrouds 1C and 3C for 0.14 W pumping power.

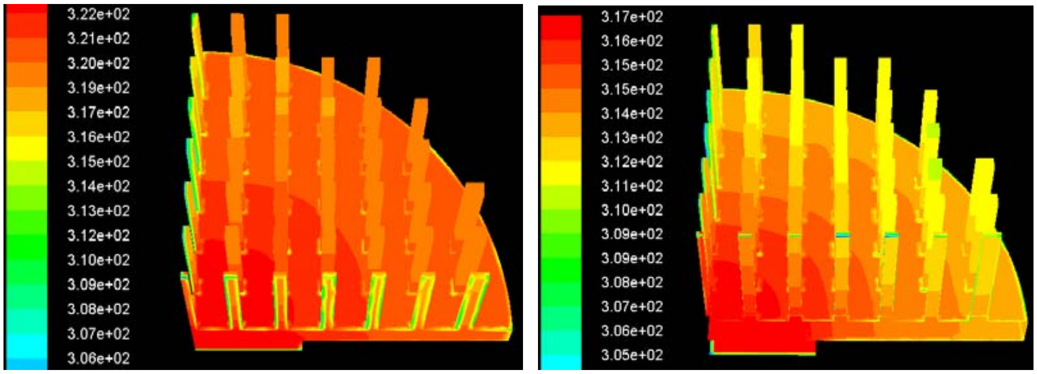

Figure 73. Temperature contours (K) for Shrouds 1C and 3C for 35 W heat load and 0.14W pumping power.

5.4 Straight Radial Fin Circular Sink with Conical or Cylindrical Shroud

Progression 3 used a circular heat sink with straight radial fins. The central heat sink core had a radius of 30 mm, which was nearly the smallest radius that could accommodate the fixed geometry of the heat source. The geometry was dictated by the effort to maintain the same convective surface area as Progression 2, and thus the heat sink and fin thickness was increased from 6.35 mm to 7.855 mm. For the quarter-symmetry geometry, there were 16 straight radial fins of 37.72 x 7.855 x 2.25 mm. The heat sink in Progression 3 had merely 0.3% more surface area than that for Progression 2.

As shown in Figure 74, the velocity inlet area at the top of the conical Shroud 1SRO was iteratively increased until the shroud became Cylinder Channel 1SRO. The cross-section of the cylinder channel was not altered to create any further cylinder geometries. The shroud dimensions for this progression's runs are shown in Table 13.

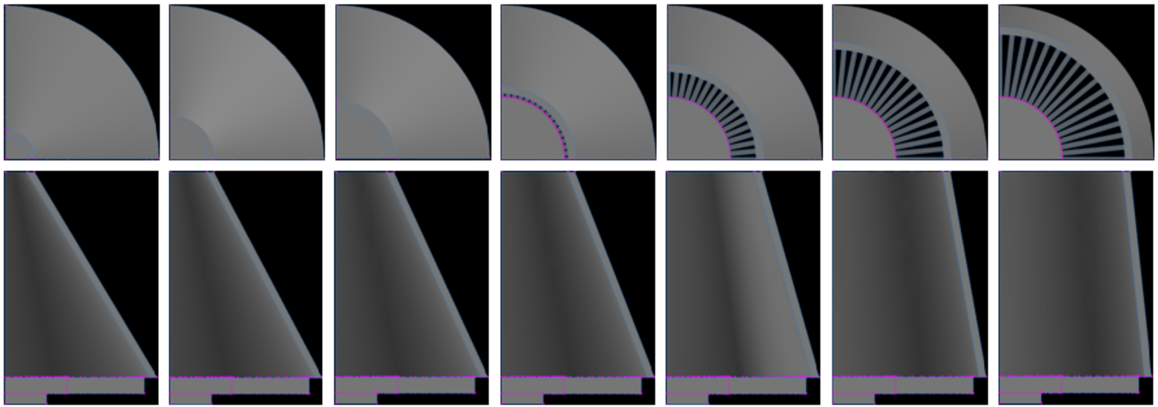

Shroud 1SRO Shroud 2SRO Shroud 3SRO Shroud 4SRO Shroud 5SRO Shroud 6SRO Shroud 7SRO

Cylinder Channel 1SRO

Figure 74. Straight radial fin heat sink in conical shrouds and a cylindrical channel.

Table 13. Shroud dimensions for Progression 3.

	Inlet radius (mm)	Base radius (mm)
Shroud 1SRO	10.6	70.71
Shroud 2SRO	17.675	70.71
Shroud 3SRO	24.75	70.71
Shroud 4SRO	31.82	70.71
Shroud 5SRO	42.425	70.71
Shroud 6SRO	53.05	70.71
Shroud 7SRO	60.1	70.71
Cylinder Channel 1SRO	70.71	70.71

Figure 75 shows the overall system performance for Progression 3 with a 35 W heat load. For the smallest cross-sectional inlet area of Shroud 1SRO, the interface temperature decreased from about 343 K to 320 K as the pumping power was increased from 0.01 W to 0.50 W. As the inlet area was increased from Shroud 1SRO to Cylinder 1SRO, the temperatures were continually lower for a given pumping power, which signified a continual improvement in overall system performance. For Cylinder 1SRO, the interface temperature decreased from about 320 K to 311 K as the pumping power was increased from 0.01 W to 3.80 W.

As can be seen in Figure 75, the impact of the shroud was more significant at smaller pumping powers. The temperature disparity for the various shrouds at a fixed pumping power was always less than 11 K.

Shrouds 6SRO and 7SRO had almost identical overall performance as Cylinder 1SRO. Along with being the best shroud geometry for Progression 3, Cylinder 1SRO has additional benefits over sloped shrouds because of manufacturing and cost concerns.

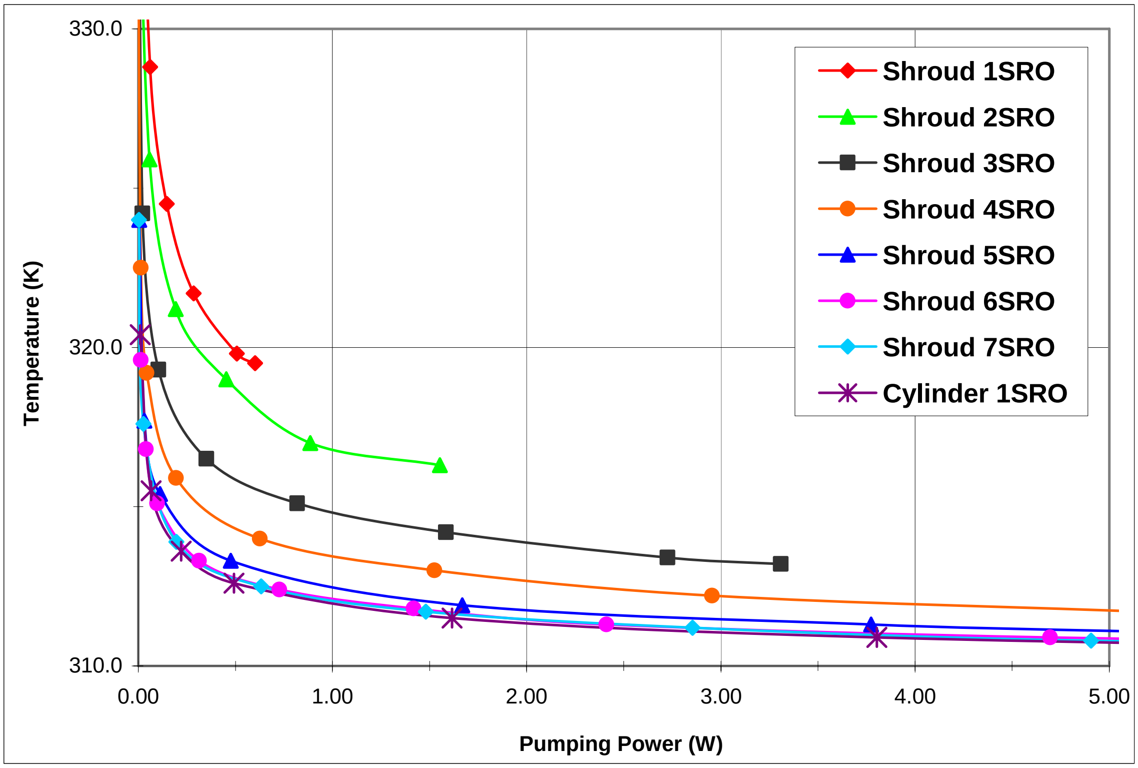

Figure 75. Source/sink interface temperature vs. pumping power for Progression 3 with a 35 W heat load.

Figure 76 shows the temperature vs. volumetric flow rate relationships for Progression 3, which were markedly different from Progressions 1 and 2. Without pin fins, less of the convective surface area was centralized in this progression. Thus, the focused-velocity effect did not have a significant role, and increasing the inlet area did not substantially impact the temperature vs. flow rate performance. Excluding Shroud 1SRO, the consistent temperature vs. volumetric flow rate performance was in close accordance with this power fit correlation shown in Figure 77:

$$T = .4V^{-.7118} + 308.1 \tag{37}$$

T represents the interface temperature and V represents the volumetric flow rate. The R-square value was 0.9982 and the root mean square error value was 0.1819.

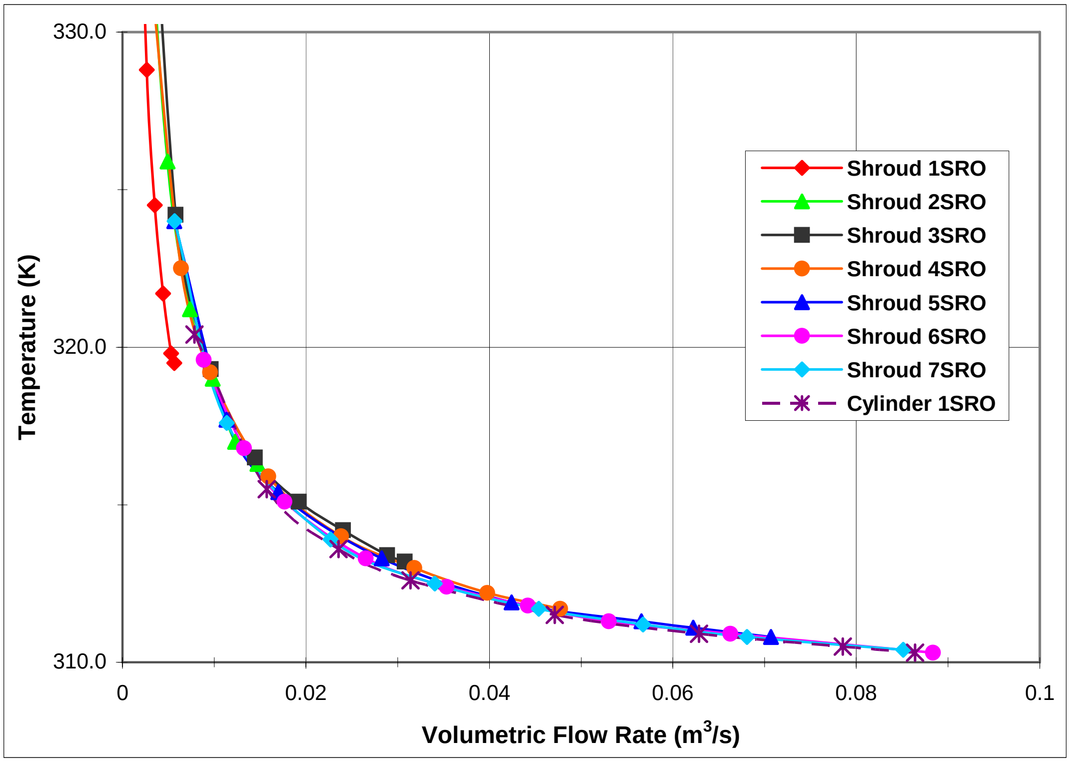

Figure 76. Source/sink interface temperature vs. inlet volumetric flow rate for Progression 3 with a 35 W heat load.

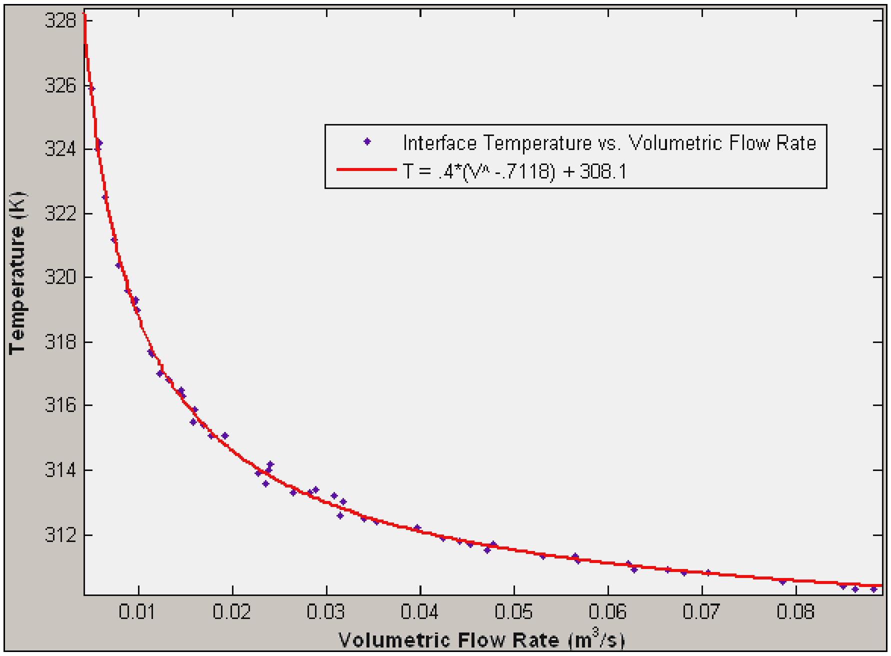

Figure 77. Power fit correlation for interface temperature and inlet volumetric flow rate for Progression 3 with a 35 W heat load, excluding Shroud 1SRO

The flow fields for Shroud 1SRO and Cylinder 1SRO are provided in Figure 78, with the latter having a more seamless path of interaction with the radial fins. The relatively evenly-distributed fluid flow of Cylinder 1SRO utilized the heat sink well, as illustrated by the temperature contours in Figure 79. Again, the cylinder has flow recirculation on the bottom surface of the heat sink, and the cylinder was imaged in an "unfilled" manner due to high element count.

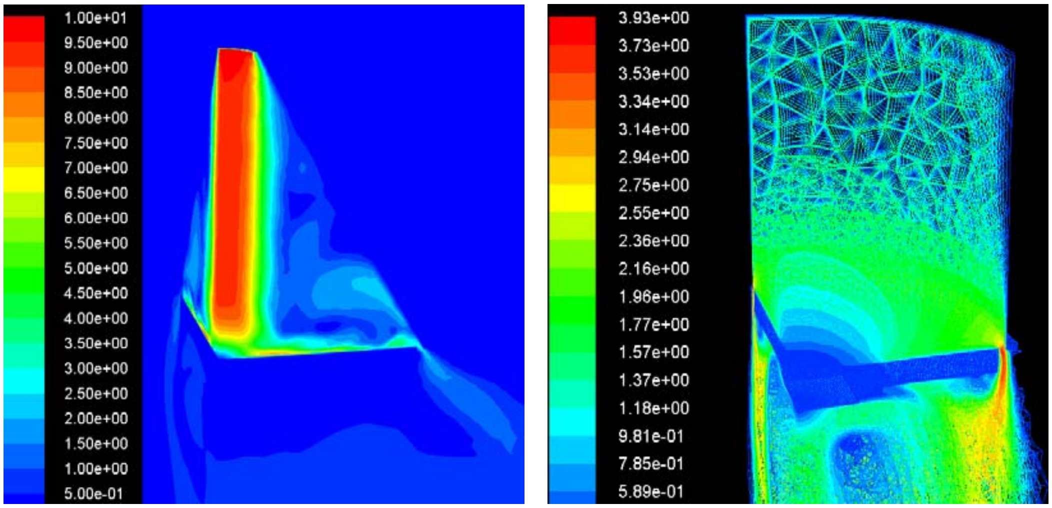

Figure 78. Velocity contours (m/s) for Shroud 1SRO and Cylinder 1SRO for 0.15 W pumping power.

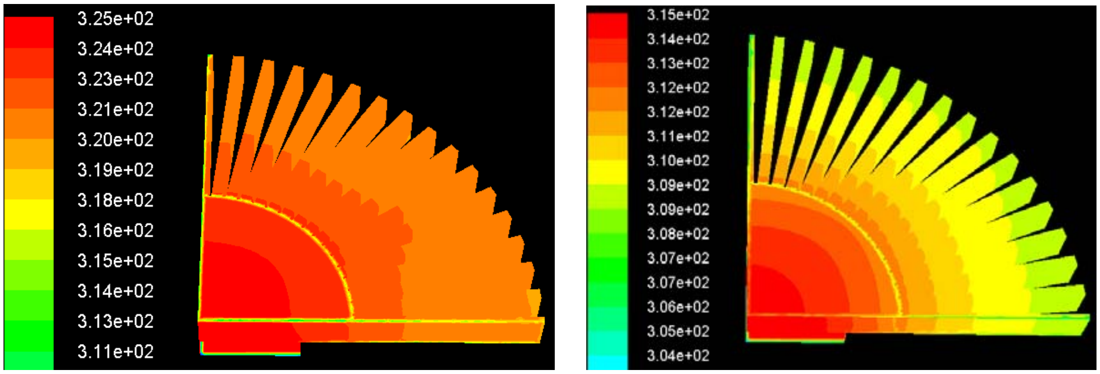

Figure 79. Temperature contours (K) for Shroud 1SRO and Cylinder 1SRO for 35 W heat load and 0.15 W pumping power.

5.5 Pin and Radial Fin Circular Sink with Conical or Cylindrical Shroud

Progression 4 used a circular heat sink with both pin fins and straight radial fins. The central heat sink core had a radius of 30 mm, which was the same as Progression 3. Like Progressions 1 and 2, the heat sink and fin thickness was 6.35 mm. The heat sink in this progression had the same surface area as that for Progression 2. For the quarter-symmetry geometry, there were 16 straight radial fins of 37.72 x 7.855 x 2.25 mm and 9.25 pin fins.

As shown in Figure 80, the velocity inlet area at the top of the conical Shroud 1SR was iteratively increased until the shroud became Cylinder Channel 1SR. The cross-section of the cylinder channel was not altered to create any further cylinder geometries. The shroud dimensions for this progression's runs are shown in Table 14.

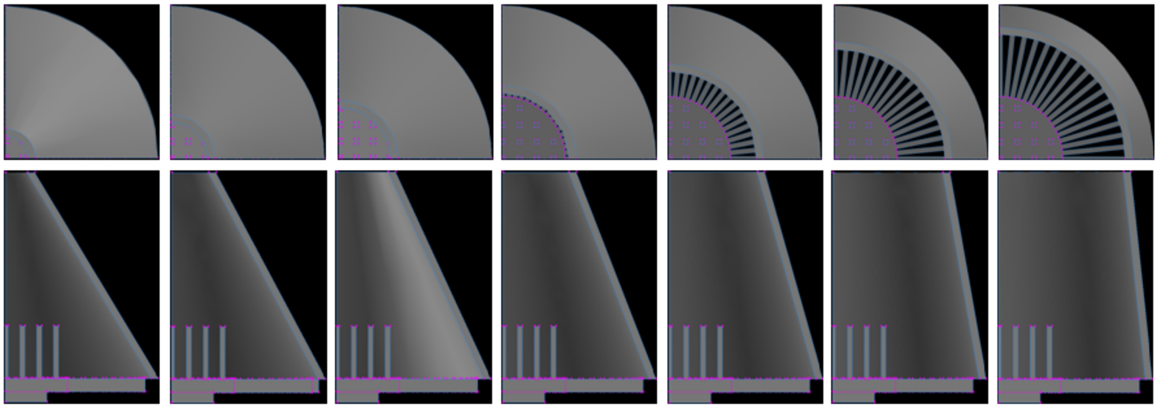

Shroud 1SR Shroud 2SR Shroud 3SR Shroud 4SR Shroud 5SR Shroud 6SR Shroud 7SR

Cylinder Channel 1SR

Figure 80. Circular heat sink with pin fins and straight radial fins in conical shrouds and a cylindrical channel.

Table 14. Shroud dimensions for Progression 4.

	Inlet radius (mm)	Base radius (mm)
Shroud 1SR	10.6	70.71
Shroud 2SR	17.675	70.71
Shroud 3SR	24.75	70.71
Shroud 4SR	31.82	70.71
Shroud 5SR	42.425	70.71
Shroud 6SR	53.05	70.71
Shroud 7SR	60.1	70.71
Cylinder Channel 1SR	70.71	70.71

Figure 81 shows the overall system performance for Progression 4 with a 35 W heat load. For the smallest cross-sectional inlet area of Shroud 1SR, the interface temperature decreased from about 343 K to 319 K as the pumping power was increased from 0.01 W to 0.70 W. As the inlet area was increased from Shroud 1SRO to Shroud 5SRO, the temperatures were continually lower for a given pumping power, which signified a continual improvement in overall system performance. For Shroud 5SRO, the interface temperature decreased from about 320 K to 311 K as the pumping power was increased from 0.01 W to 5.00 W.

Increasing the cross-sectional inlet area from Shroud 5SR to Cylinder 1SR resulted in slightly worse overall performance. Because of the very low disparity and the manufacturing and cost concerns, Cylinder 1SR would be deemed the best shroud geometry for Progression 4.

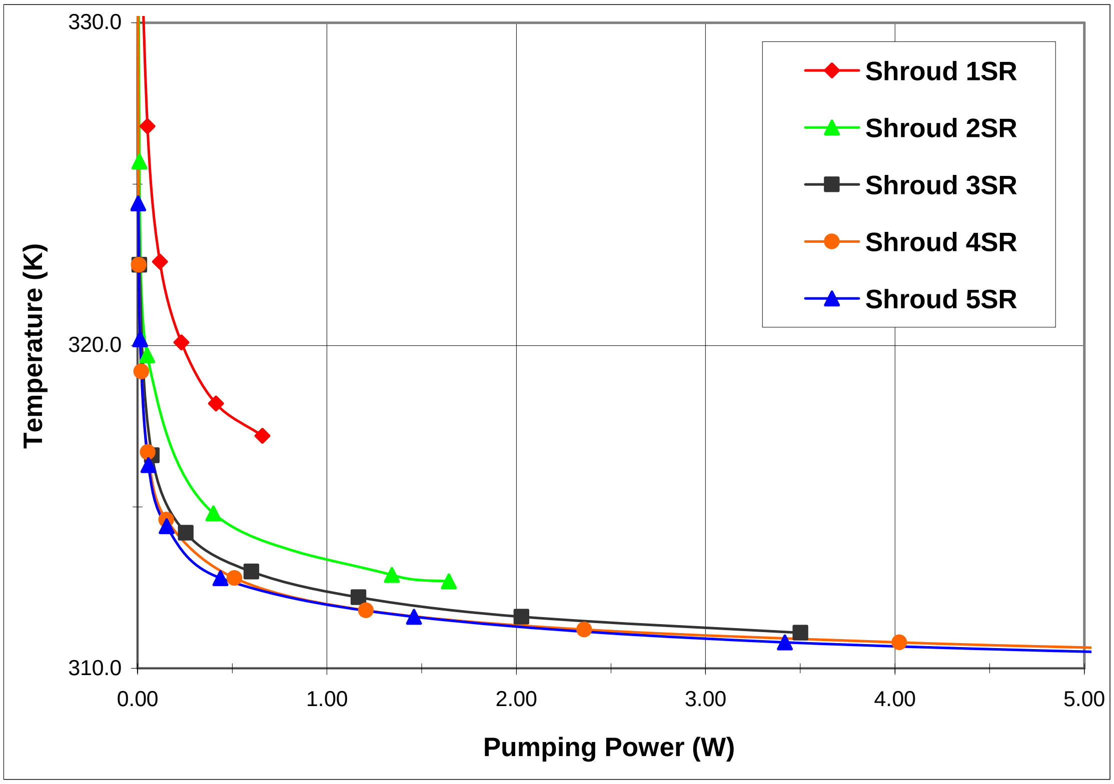

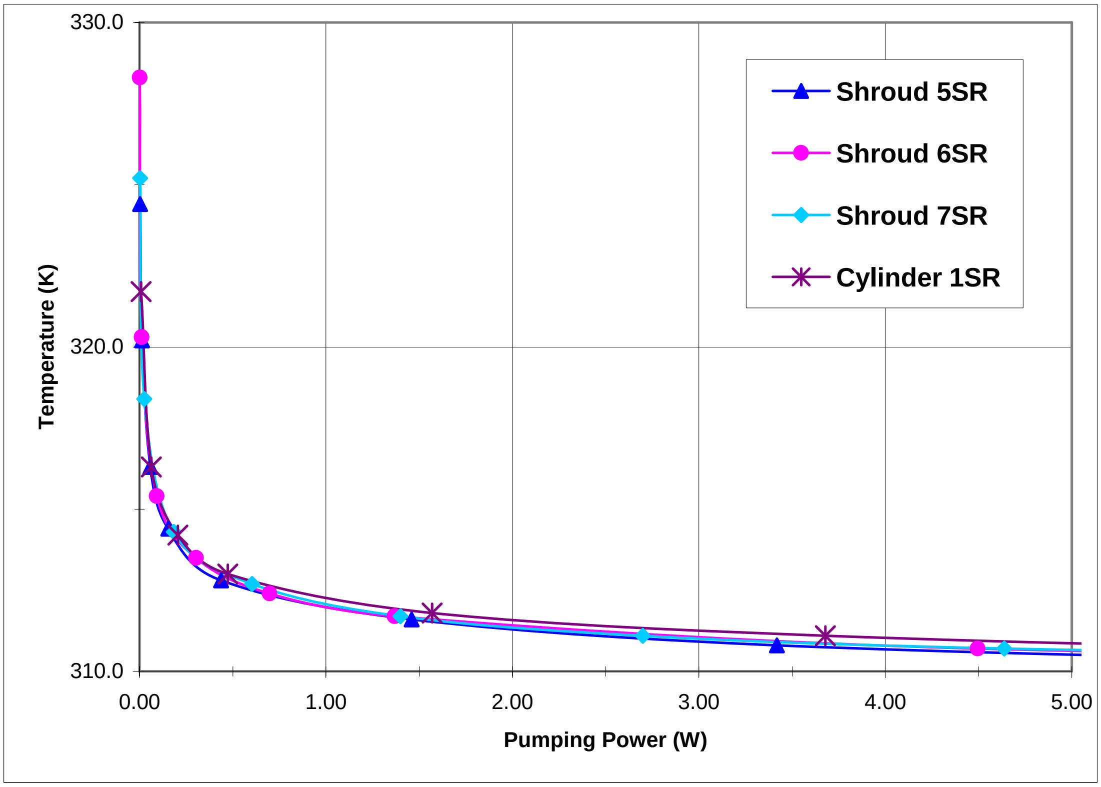

Figure 81. Source/sink interface temperature vs. pumping power for Progression 4 with a 35 W heat load.

For Progression 4, the interrelations of the heat sinks' temperature vs. volumetric flow rate performance were close to the average of those between Progressions 2 and 3. While Progression 2 had a strong variance of the thermal dependence on the flow rate, Progression 3 had barely any variance at all and Progression 4 had a subtle dependency variance. The reasoning for these relationships is most likely due to the level of presence of pin fins. In similar fashion as the previous progressions, increasing the inlet area increased the volumetric flow rate for a given pressure drop.

The flow fields for Shroud 1SR and Cylinder 1SR are provided in Figure 82, in which Cylinder 1SR had to be imaged in an "unfilled manner" due to its higher element count. The temperature contours for these two heat sinks are provided in Figure 83.

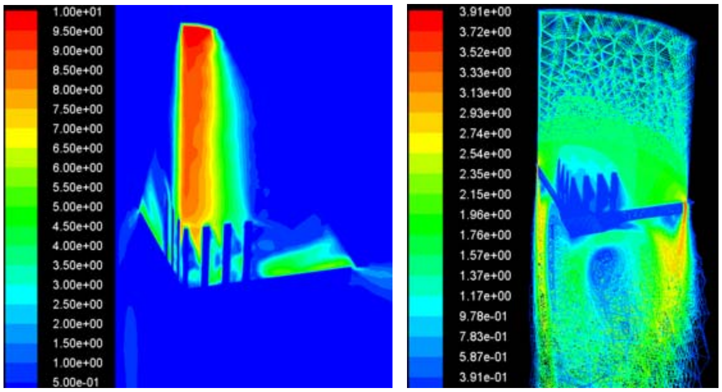

Figure 82. Velocity contours (m/s) for Shroud 1SR and Cylinder 1SR for 0.12 W pumping power.

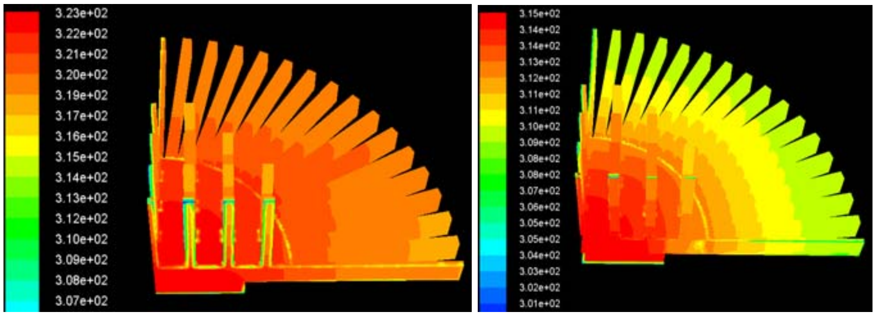

Figure 83. Temperature contours (K) for Shroud 1SR and Cylinder 1SR for 35 W heat load and 0.12 W pumping power.

5.6 Pin and Curved Radial Fin Circular Sink with Conical Shroud

Progression 5 was a brief experiment of curved radial fins, which kept the surface area relatively the same as the heat sinks in Progressions 2 – 4. Figure 84 shows the geometries created for this progression, which had symmetry boundary lines in accordance with the flow path's anticipated mid-stream vectors.

While these curved radial heat sinks generally had overall system performance slightly inferior to the previous progressions, potential improvements could be made with a more thorough curved fin design study. Even if the curved fin systems were better engineered, the manufacturability and cost concerns would potentially limit them to natural convection applications.

Figure 85 compares the performance of the heat sinks from Progressions 1 – 5 for the fixed shroud slopes of Shroud 2 and Shroud 5. The heat sinks were highly dependent on the fluid flow pattern, and therefore the performance interrelations varied. For example, the Progression 3's heat sink was by far the worst of the five heat sinks when Shroud 2C was used. When Shroud 5C was used, that heat sink was the second best.

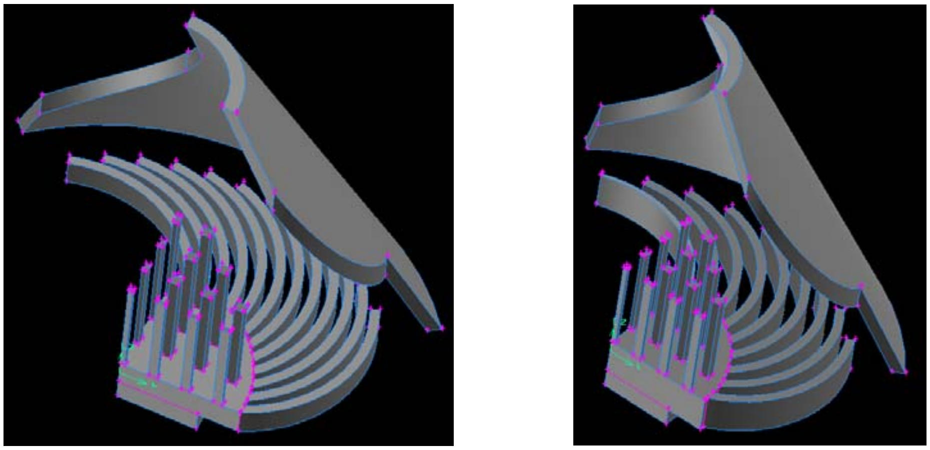

Figure 84. Circular heat sinks with 12 curved 6.35mm-thick radial fins, and 8.5 curved 10mm-thick radial fins.

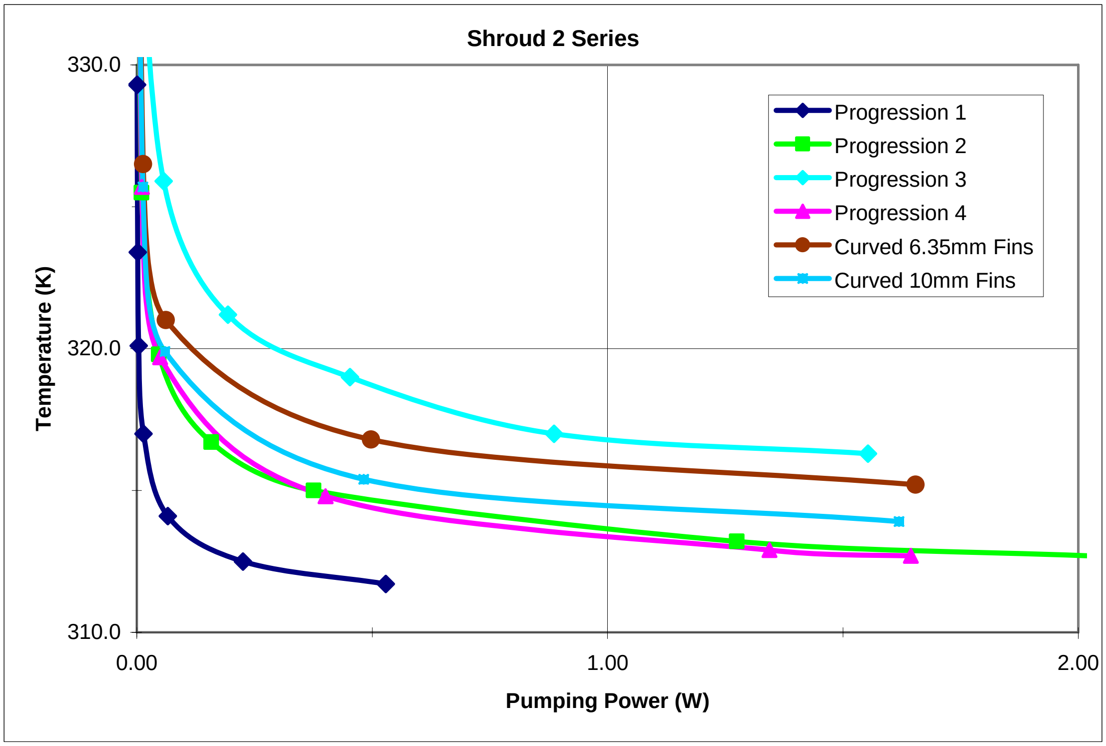

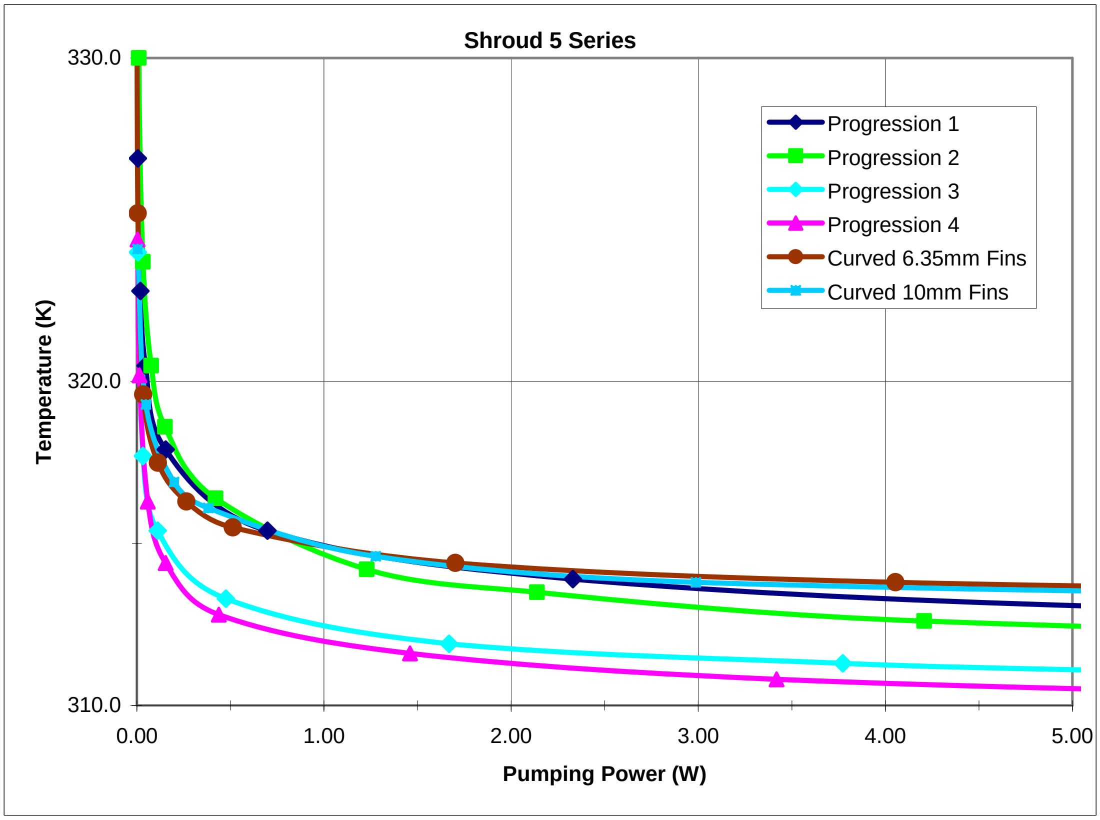

Figure 85. System performance comparisons of Progression 1-5 for fixed shrouds.

5.7 Further Analysis of Straight Radial Fin Circular Sink in Cylinder

Based on overall performance, manufacturing considerations, and cost, the straight radial fin circular sink in cylindrical channel (Progression 2) geometry was one of the most promising of the considered configurations. This section describes further analyses of these sinks, for which the surface area was no longer held constant. For the first part of this progression, the thickness of the heat sinks and radial fins was iteratively increased, as illustrated in Figure 86. The shroud height was reduced to 10 mm since the cylinder walls could tolerate placing the heat sink closer to the active cooling source. Also, the y-axis scale of the temperature graphs has been changed from the previous sections to accommodate the lower temperatures realized by these systems.

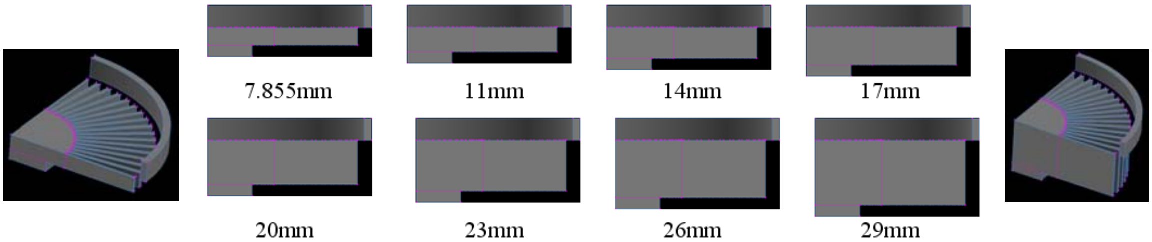

Figure 86. Side profiles of straight radial fin heat sinks for Progression 6.

Figure 87 shows the overall system performance for Progression 6 with a 35 W heat load. For the thinnest heat sink of 7.855 mm thickness, the interface temperature decreased from about 320 K to 311 K as the pumping power was increased from 0.01 W to 3.80 W. As the heat sink and fin thickness increased from 7.855 mm to 29 mm, the temperatures were continually lower for a given pumping power, which signified a continual improvement in overall system performance. During this iterative increase in thickness, the diminishing increases in performance reflected the increase in conduction resistance. If the thickness was further increased such that it went beyond the optimum value for these constraints, the overall system performance would have begun to decrease and the interface temperature would have risen. This would have signified the conduction resistance becoming more critical than the convective resistance. The computational demand for heat sinks thicker than 29 mm was unreasonable for this study.

For the thickest heat sink considered, of 29 mm thickness, the interface temperature decreased from about 313 K to 306 K as the pumping power was increased from 0.02 W to 4.20 W. Extending the shroud down to encase the heat sink slightly improved the performance for all 29 mm cases, while it marginally decreased the performance for high-pumping power 7.855 mm cases.

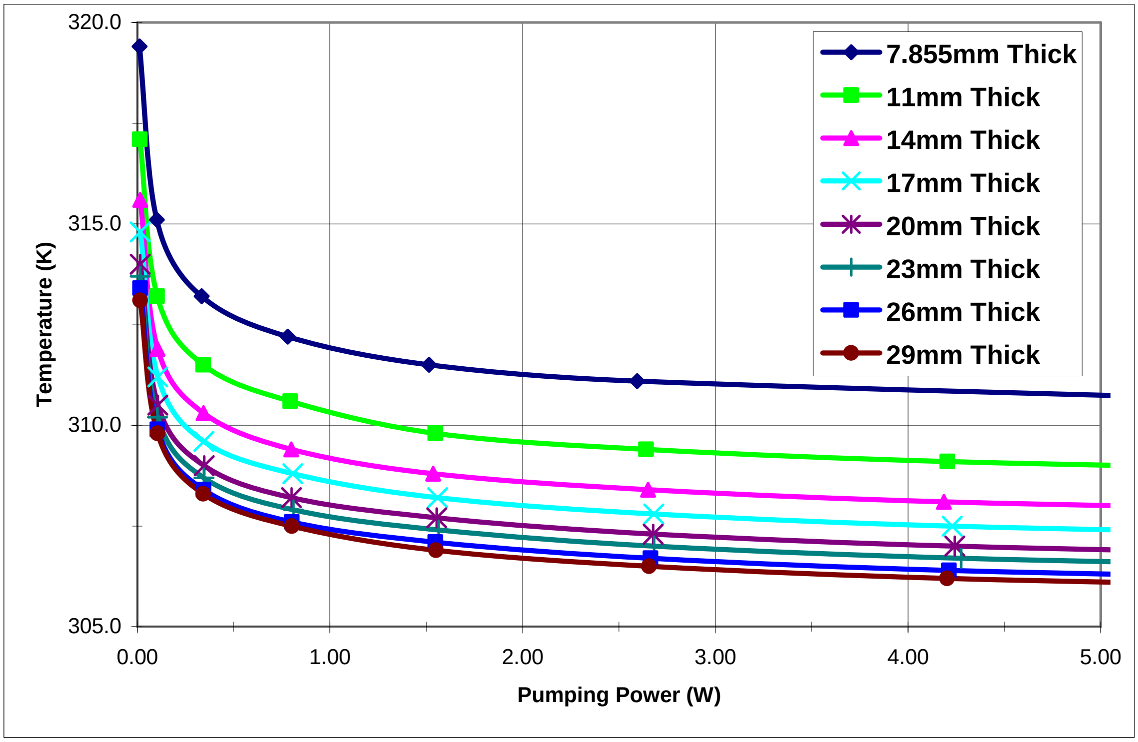

Figure 87. Source/sink interface temperature vs. pumping power for Progression 6 with a 35 W heat load.

The volumetric flow rate vs. pressure drop performance was virtually constant fro this progression. This was expected since the impinging flow approached an identical cross-section for every case. Furthermore, the fin thickness range up to 29 mm was not large enough to cause significant discrepancies in the boundary layer development along the fins. Hence, the temperature vs. volumetric flow rate relationships had very similar trends as those for temperature vs. pressure performance.

The temperature contours for the thinnest heat sink in this progression are shown in Figure 88, while those for the thickest sink are shown in Figure 89. The conduction resistance is dominated by spreading resistance, which is to be expected in small-scale heat sinks. This claim is supported by the thermal gradient lines being nearly vertical.

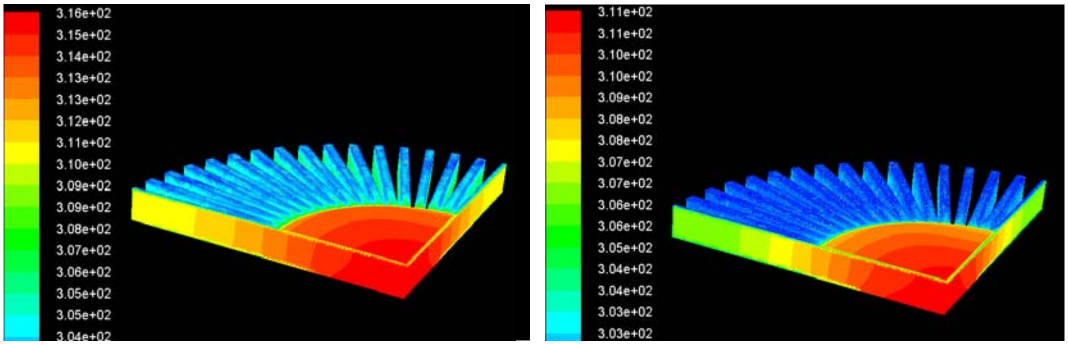

Figure 88. Temperature contours (K) for 7.855mm-thick, 35W heat load. The pumping power for the first image is 0.10 W and for the second image is 6.13 W.

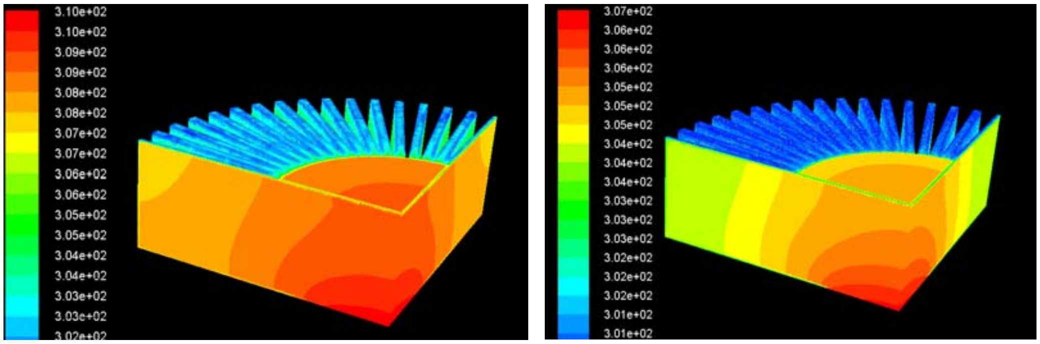

Figure 89. Temperature contours (K) for 29mm-thick, 35W heat load. The pumping power for the first image is 0.10 W and for the second image is 6.22 W.

Increasing the radius of the central hub of the 20mm-thick heat sink from 30mm to 40mm reduced the surface area by almost 20%, as well as decreased performance as shown in Figure 90. This reinforced the importance of surface area in these small-scale shrouded heat sinks.

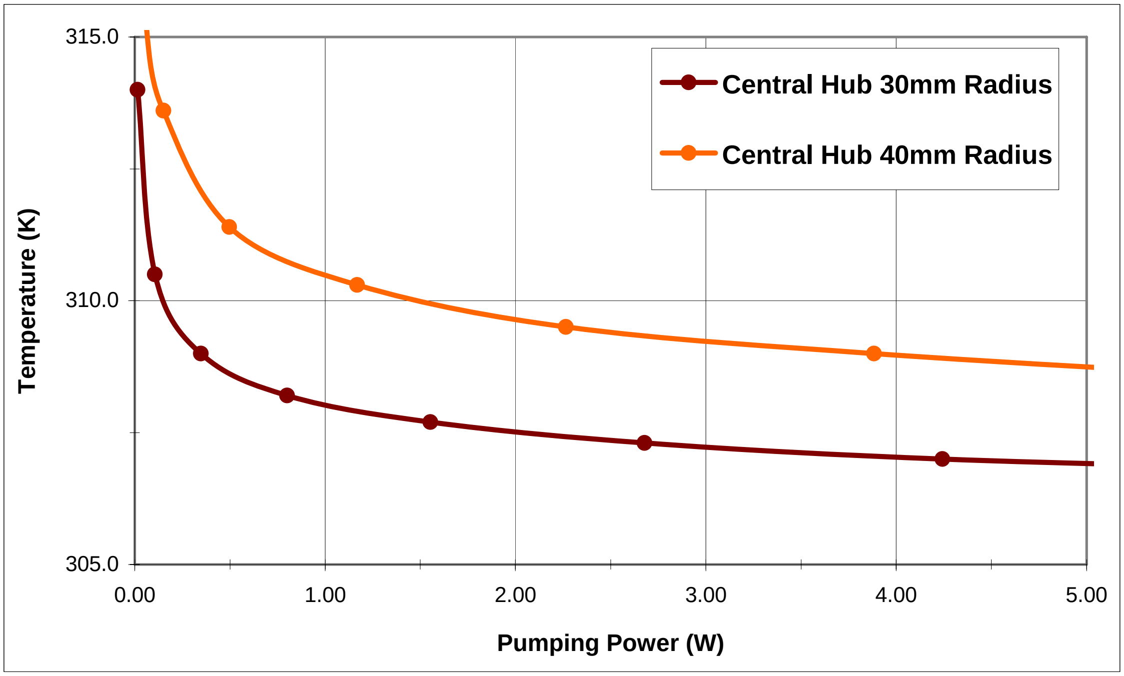

Figure 90. Source/sink interface temperature vs. pumping power for 20mm-thick heat sinks with a 35 W heat load and different hub radii.

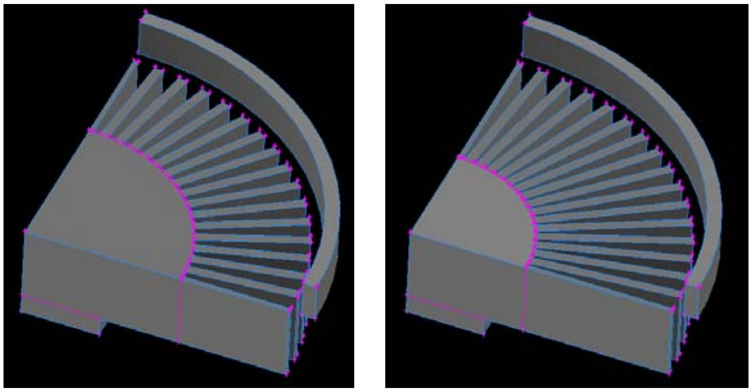

Figure 91. Geometry for the two cases in Figure 90.

5.8 Results Summary and Thermal Resistances

For each progression, the optimal shroud for the design constraints heavily depended on how the heat sink interacted with the fluid flow and utilized the pumping power. When the shroud inlet area was small, the impinging velocity was focused at the central hottest part of the heat sinks. This imposed the impingement flow to be transformed into cross-flow which enhanced the pressure requirement. Also, the fluid heated up as it traveled along the flow path, and therefore a longer flow path entailed diminished thermal dissipation capability of down-stream convective surface area. Furthermore, increasing the inlet cross-section decreased the flow velocity but increased the volumetric flow rate for a given pressure drop. Thus, the pumping power required was also increased.

For Progression 1's pin fin square heat sink, Shroud 4 performed the best with its slope angle of 71.8º. For Progression 2's pin fin circular heat sink, Shroud 3C performed the best with its slope angle of 65.3º. The circular heat sink of Progression 3, which had straight radial fins, performed best for the cylindrical channel shroud. The circular heat sink of Progression 4, which had both pin fins and straight radial fins, also performed best for the cylindrical channel shroud.

Within each progression, there was a considerable range of overall system performance due to the various shroud geometries and pumping powers parametrically studied. The impact of the shroud was more apparent at lower velocities.

When comparing the progressions to each other, the ranking of overall system performance for the heat sinks highly depended on what shroud was applied. Generally, the circular sinks of Progressions 2 – 4 outperformed the square sinks of Progression 1, despite the latter having around 15% more surface area. This indicated the importance of how well the heat sink utilized the fluid flow's pumping power. Out of Progressions 1 – 5, the circular sinks with straight radial fins from Progression 3 had the most promising overall system performance, mainly because they were more appropriately designed aerodynamically than the other heat sinks.

Because the heat sinks in this study were of small-scale, thermal dissipation was essentially convection-limited. In addition, the spreading resistance was a substantial portion of the conduction resistance of these systems.

Figure 92 shows the best-case shrouded system geometry from each progression and the associated thermal resistance for a pumping power of 5 W, solid material of aluminum, and an ambient temperature of 300 K. Progression 5, which was for curved fin geometries, was excluded from Figure 92 since that configuration was neither extensively studied nor the focus of this active cooling analysis.

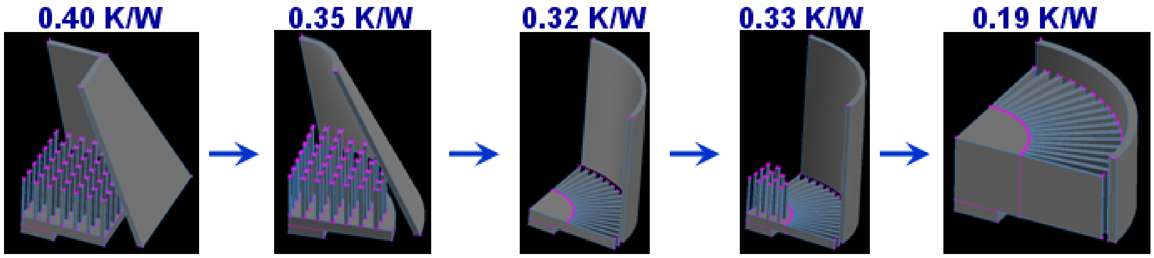

Figure 92. Thermal resistances for systems with 5W pumping power and 300K ambient temperature.

Progression 6's 29mm-thick heat sink had a thermal resistance of 0.183 K/W for a pumping power of 6.23 W. While maintaining this pumping power, the thermal resistance dependency on the solid material's thermal conductivity was studied. The thermal resistance was reduced to 0.161 K/W by changing the solid material from aluminum to copper aluminum. When the core was copper and the fins were aluminum, the thermal resistance was 0.171 K/W. When the effective thermal conductivity of the core was set as 1,000 W/m*K to reflect a vapor chamber, the thermal resistance was 0.167 K/W. Temperature contours for these four scenarios are shown in Figure 93.

All Aluminum

Copper Core, Aluminum Fins

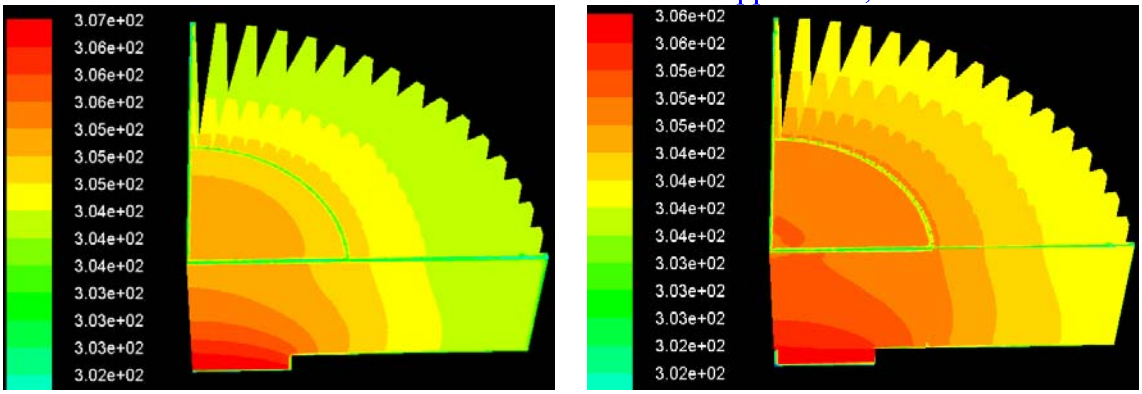

Vapor Chamber Core, Aluminum Fins

All Copper

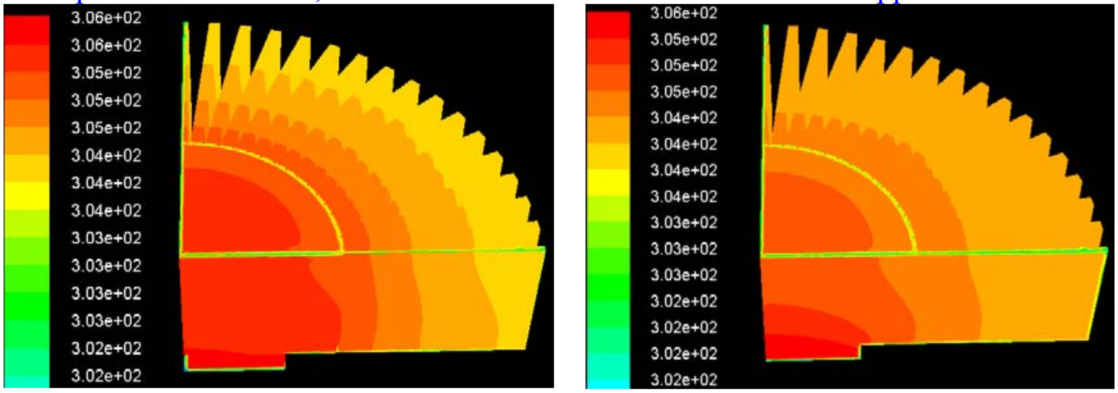

Figure 93. Temperature contours (K) for 29mm-thick heat sinks from Progression 6 with a 35W heat load and 6.23W pumping power

The thermal resistances of this study's heat sinks demonstrated the capability to cool LED down-light sources, although their effectiveness was quite dependent on the aerodynamic performance that was influenced by the shroud. Table 15 contains some of the iterative data for the best-case shroud configurations from each progression, including the thermal resistances along the pressure drop spectrum of this study.

Table 15. Data from the best-case shroud for each progression.

Description	Velocity	Flow Rate	Pressure	Pumping Power	Max Temperature		Flux	Thermal Resistance
	m/s	m^3/s	Pa	W	Kelvin	°C	W	K/W
§5.2 Progression 1 Shroud 4	1.0	0.0041	0.57	0.0023	323.5	50.4	35.015	0.67114
	2.0	0.0081	2.21	0.0179	321.2	48.1	35.015	0.60545
	3.0	0.0122	4.92	0.0598	318.6	45.5	35.010	0.53127
	5.0	0.0203	13.69	0.2772	316.1	43.0	35.015	0.45980
	7.5	0.0304	30.51	0.9268	314.6	41.5	35.011	0.41702
	10.0	0.0405	54.04	2.1886	313.7	40.6	35.016	0.39125
	12.5	0.0506	84.76	4.2910	313.3	40.2	35.016	0.37983
§5.3 Progression 2 Shroud 3C	2.0	0.0038	2.01	0.0077	325.2	52.1	35.011	0.71978
	3.5	0.0067	6.11	0.0412	319.7	46.6	35.013	0.56264
	5.0	0.0096	12.59	0.1211	317.1	44.0	35.006	0.48848
	7.5	0.0144	28.06	0.4050	315.0	41.9	35.001	0.42856
	10.0	0.0192	50.09	0.9638	313.7	40.6	35.010	0.39132
	12.5	0.0241	78.36	1.8850	312.9	39.8	35.012	0.36844
	14.0	0.0269	102.71	2.7672	312.6	39.5	35.011	0.35989
	17.0	0.0327	146.05	4.7779	312.1	39.0	35.011	0.34560
§5.4 Progression 3 Cylinder 1SRO	0.5	0.0079	1.17	0.0091	321.1	48.0	35.011	0.60266
	1.0	0.0157	4.22	0.0663	316.2	43.1	35.013	0.46269
	2.0	0.0314	15.66	0.4921	313.3	40.2	35.013	0.37985
	3.0	0.0471	34.28	1.6154	312.2	39.1	35.009	0.34848
	4.0	0.0628	60.52	3.8025	311.6	38.5	35.015	0.33129
	5.0	0.0785	94.09	7.3894	311.2	38.1	35.012	0.31989
	5.5	0.0864	113.44	9.8000	311.0	37.9	35.008	0.31422
§5.5 Progression 4 Cylinder 1SR	0.5	0.0079	1.14	0.0089	322.5	49.4	35.016	0.64256
	1.0	0.0157	4.07	0.0638	317.1	44.0	35.018	0.48832
	2.0	0.0314	15.07	0.4732	313.8	40.7	35.018	0.39408
	3.0	0.0471	33.33	1.5703	312.5	39.4	35.019	0.35695
	4.0	0.0628	58.58	3.6793	311.8	38.7	35.015	0.33700
	5.0	0.0785	91.07	7.1502	311.4	38.3	35.025	0.32549
§5.6 Progression 5 Shroud Slope 5 12 Curved Fins	1.0	0.0057	0.81	0.0046	325.9	52.8	35.012	0.73975
	2.0	0.0115	2.99	0.0343	320.3	47.2	35.012	0.57979
	3.0	0.0172	6.58	0.1130	318.2	45.1	35.011	0.51984
	5.0	0.0286	17.92	0.5132	316.2	43.1	35.017	0.46263
	7.5	0.0430	39.64	1.7031	315.1	42.0	35.022	0.43116
	10.0	0.0573	70.79	4.0555	314.5	41.4	35.017	0.41408
	12.5	0.0716	109.07	7.8108	314.2	41.1	35.015	0.40554
§5.7 Progression 6 29mm-thick Sink 10mm Cylinder Shroud	0.5	0.0079	2.59	0.0203	311.8	38.7	35.014	0.33701
	0.8	0.0118	5.17	0.0609	310.0	36.9	35.009	0.28564
	1.0	0.0157	8.69	0.1364	309.2	36.1	35.014	0.26275
	1.5	0.0236	18.66	0.4396	308.1	35.0	35.015	0.23133
	2.0	0.0314	29.57	0.9291	307.5	34.4	35.016	0.21419
	2.5	0.0393	50.20	1.9714	307.0	33.9	35.017	0.19990
	3.0	0.0471	71.98	3.3919	306.7	33.6	35.016	0.19134
	3.5	0.0550	98.08	5.3921	306.4	33.3	35.018	0.18276

CHAPTER 6

SUMMARY, OPPORTUNITIES, AND CONCLUSIONS

6.1 Summary

6.1.1 Goals Reviewed

This numerical study utilized FLUENT to accurately predict the overall system performance of the active air cooling of LED-scale aluminum heat sink systems with various pin fin and radial fin arrangements in pyramidal, square, conical, and circular shrouds. Because forced convection was utilized, the effectiveness of the heat sink systems was linked to the energy input. Thus, the overall system performance was defined as the heat-source heat-sink interface temperature vs. inlet pumping power.

The optimization methodology for these systems was to maximize the overall thermal conductance by simultaneously considering thermal resistances, flow characteristics, and convective surface area. This research created a framework for this optimization pursuit for future system designs and laboratory experiments. Also, the results have supported the supposition that the shrouded active cooling systems can achieve thermal resistances low enough for the suitable thermal management of high power LED arrays.

6.1.2 LED Commercialization

Due to their prospective technological superiority and developing public policy, LEDs have a very strong potential to be the standard light source within the next decade. The possibilities of market penetration for solid-state lighting rely predominantly on reducing ownership cost, as well as ensuring device performance/reliability by incorporating effective thermal management. While outdoor applications will generally be easier to implement, indoor down-lighting modules will have to overcome tight design constraints, constricted clearances, elevated ambient temperatures, and building code requirements. These systems may call for forced convection cooling that uses shrouded radial heat sinks to increase the heat transfer while reducing the space utilization. For active cooling mechanisms, the aspects of energy input, cost, footprint, noise, and lifetime must be considered.

6.1.3 Thermal Management Significance for High Power LEDs

Solid-state lighting device lifetime and lumen output are highly dependent on junction temperature. Operating 10ºC above the specified temperature would reduce the average time-to-failure by approximately 50% for most LED applications, while this same increase in temperature would reduce white light lumen output by about 5% [23, 24]. At a fixed pumping power of 5 W, the best-case for Progression 6 was cooler than that for Progression 1 by about 5ºC and 15ºC for a heat load of 25W and 75W, respectively. Within each progression, the pumping power range studied caused the temperature range for a specific shroud to be as high as 40ºC. Thus this kind of analysis could aid in selecting a fan and operating point. A lifetime cost analysis considering capital and operating costs would be utilized to determine the most cost-effective operating pumping power.

For active cooling, the mechanism for generating the flow field is a crucial aspect. The shrouded heat sink system performance would have a role in selecting a fan and determining at what pressure drop to operate. Traditionally, axial fans have been used for microelectronic applications similar to that proposed in this study. Figure 94 contains data and fan curves for six axial fan models. Approximately 3.5 – 7.5 W of power would need to be supplied to provide enough flow for most of the suitable cases in this study. This moderate energy requirement of axial fans is one of the main drivers for developing the more energy-efficient synthetic jet technology. While not commercially established yet, synthetic jet flow generation is more compact than axial fans. It also has a shorter entrainment path and more evenly distributed fluid flow. However, due to severely localized flow and low volumetric flow rates, arrays of jets would be needed [130].

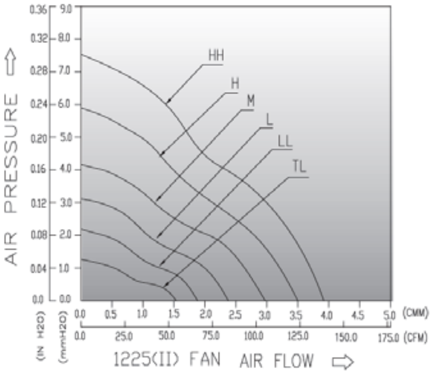

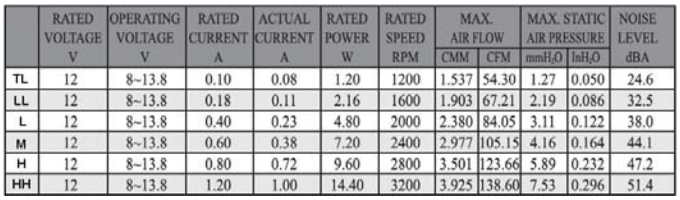

	RATED VOLTAGE V	OPERATING VOLTAGE V	RATED CURRENT A	ACTUAL CURRENT A	RATED POWER W	RATED SPEED RPM	MAX. AIR FLOW		MAX. STATIC AIR PRESSURE		NOISE LEVEL dBA
							CMM	CFM	mmH_2O	InH_2O	
TL	12	8~13.8	0.10	0.08	1.20	1200	1.537	54.30	1.27	0.050	24.6
LL	12	8~13.8	0.18	0.11	2.16	1600	1.903	67.21	2.19	0.086	32.5
L	12	8~13.8	0.40	0.23	4.80	2000	2.380	84.05	3.11	0.122	38.0
M	12	8~13.8	0.60	0.38	7.20	2400	2.977	105.15	4.16	0.164	44.1
H	12	8~13.8	0.80	0.72	9.60	2800	3.501	123.66	5.89	0.232	47.2
HH	12	8~13.8	1.20	1.00	14.40	3200	3.925	138.60	7.53	0.296	51.4

Figure 94. Axial fan data from an example commercial product [135].

6.1.4 Impact of Shroud

Because the heat sinks in this study were of small-scale, thermal dissipation was essentially convection-limited. Thus, how the shroud influenced the aerodynamic characteristics was pivotal for overall system performance. Within each progression, there was a considerable range of overall system performance due to the various shroud geometries and pressure drops parametrically studied. The impact of the shroud was more apparent at lower pumping powers.

For Progression 1's pin fin square heat sink, Shroud 4 performed the best with its slope angle of 71.8º. For Progression 2's pin fin circular heat sink, Shroud 3C performed the best with its slope angle of 65.3º. The circular heat sink of Progression 3, which had straight radial fins, performed best for the cylindrical channel shroud. The circular heat sink of Progression 4, which had both pin fins and straight radial fins, also performed best for the cylindrical channel shroud. For the shrouds considered in this study, the cylindrical channel has the added benefits of easier manufacturing and lower cost.

TAKEAWAY:

Inherently, the housings for many down-lighting LEDs act as shrouds, which may be designed to simultaneously provide sufficient optical and thermal performance. The benefit of having a shroud for active cooling diminished at higher pressure drops, although its presence rarely harmed system performance. For each progression, the shroud's best geometry depended on the heat sink configuration and all other system constraints. Designing the shrouded heat sink to enhance the aerodynamic properties of forced convection can significantly increase the system's overall thermal conductance for a given pumping power.

6.1.5 Curved Fins

Curved fins area often used to increase surface area and/or compactness for a heat sink system. Because of high cost and manufacturing difficulties, they are often reserved for natural convection enhancement. For active cooling with fans, curved fins may help minimize entropy generation by having contours that seamlessly accept the incoming flow. However, trends and research indicate that synthetic jets and microjet arrays are likely to be standard method of flow generation for high power LEDs [63-65]. If future developments of curved fins sufficiently drive down cost, they may be justified for solid-state lighting applications in order to helping device performance for instances in which the active cooling method fails.

6.1.6 Thermal Resistances

This discussion considers each progression's best-case shroud utilizing 5 W of pumping power in an ambient temperature of 300 K. The transition from the square sink in Progression 1 to the circular sink in Progression 2 resulted in a 12.5% reduction in the overall system thermal resistance (0.40 K/W to 0.35 K/W), despite a 13.3% reduction in convective surface area (62,464 mm^2 to 54,172 mm^2). Also, a conical shroud imposes a circular velocity inlet, which is in accordance with many fan and synthetic jet shapes.

Maintaining Progression 2's surface area, Progressions 3 and 4 demonstrated that radial fins may be used to effectively lower the system thermal resistance. Progression 3's circular heat sinks with straight radial fins had thermal resistances as low as 0.32 K/W, which was an 8.6% reduction from Progression 2. Progression 4's circular heat sink with both pin fins and straight radial fins had a thermal resistance of 0.31 K/W, which was a 14.0 % reduction from Progression 2.

The performances of the heat sinks from Progressions 3 and 4 were nearly identical. Due to manufacturing and cost concerns, the sinks from Progression 3 would be preferred over the hybrid sinks from Progression 4 for many active cooling applications. Progression 6 was a further study of the configuration from Progression 3, although the constraint of constant surface area was abandoned. The smallest overall system thermal resistance for aluminum was 0.19 K/W, which was a 40.6% reduction from Progression 3, and a 52.5% reduction from Progression 1.

The thermal resistances reported in this study reflect the thermal resistances from conduction and convection, while the thermal resistances from interfaces and within the LED were neglected. Thus, actual thermal resistances will be significantly higher, and the junction temperature of a high-power LED would likely be at least 25ºC higher than the interface temperatures listed in this report.

The thermal resistances in this study were comparable to those of previous research publications. Jian-Hui and Chun-Xin's radial fin heat sinks had thermal resistances ranging from 0.300 K/W to 0.384 K/W. By reducing the fin thickness and tripling the fin number, the thermal resistances were reduced to a range of 0.169 K/W to 0.200 K/W [118]. Dehoff et al.'s radial folded fin heat sink with an axial fan provided a thermal resistance of 0.3 K/W [126]. For pin fin heat sinks experiencing impingement flow, Khan et al. cited thermal resistances between 0.771 K/W and 1.366 K/W [100]. For various fin geometries in shrouded cross-flow, Kim and Webb observed thermal resistances between 0.266 K/W and 0.401 K/W [92]. Arik et al. reported a thermal resistance of 0.48 K/W for circular heat sinks with extruded, 6 inch fins in natural convection [31].

<u>TAKEAWAY:</u>

System performance should be gauged by overall system thermal resistance vs. pumping power. The best shroud geometry and resulting overall thermal resistance are heavily dependent on the heat sink geometry and other system constraints. Based on thermal resistance considerations, as well as footprint, cost, and manufacturability, shrouded radial fin systems should be considered for air-cooled down-lighting arrays of high power LEDs.

6.2 Opportunities

6.2.1 Further Parametric Analyses

This research utilized geometry that was virtually unrestricted. The only imposed constraint was the size and powers of the applied heat loads. Therefore, many more aspects could be parametrically studied. This study suggests that future work should focus on analyzing radial fin patterns more so than pin fins. Also, it would be interesting to experiment with various shrouds and base openings to investigate the effects of tip clearance. Material properties, such as thermal conductivity, could also be varied.

While the computing power and time requirements would be enormous for a parametric optimization procedure on these types of systems, the design and engineering time would be reduced. Batch computing, combined with an appropriate algorithm, has strong potential for increasing the cooling performance of shrouded LED down-lights. Methodologies such as genetic algorithms can effectively evolve multi-variable problems to the optimum conditions. Programs like iSIGHT and Epogy are process integration and optimization software packages that could be used to engineer the system parameters.

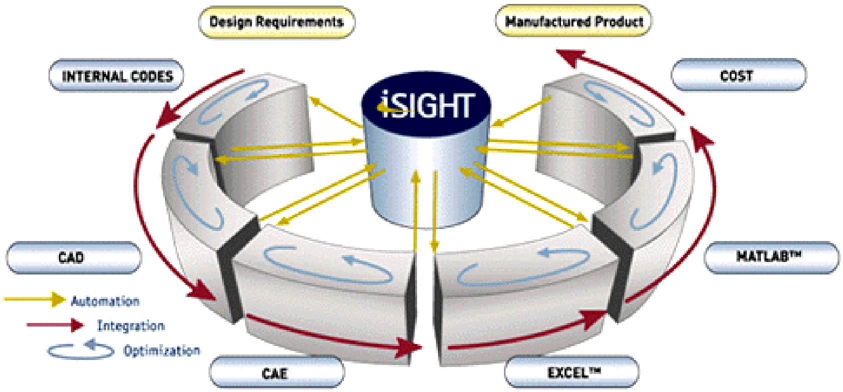

Figure 95. Flowchart for optimization program iSight [136].

6.2.2 Modeling Enhancements

The model used in this study focused on the thermal resistances from convection and within the heat sink from spreading resistance. A more developed model could potentially include the effects of thermal interface materials and inner-device dynamics on the thermal resistance network. By implementing a turbulent model, higher-velocity cases could be studied. Also, FLUENT could be used to apply fan-like velocity conditions to assess the effect of axial fan flow swirling on system performance. Unless extensive computing power is available, using a temperature-dependent density is unreasonable. Likewise, continuing to neglect radiation for forced convection is advised.

6.2.3 Experimental Opportunities

Laboratory experiments could be used to further verify the trends found in this study, as well as gauge the accuracy and precision of the results of the numerical analyses. Physical tests could also help determine the amount of radiation heat transfer involved with these systems, as well as incorporate thermal interface material resistances. The uniform velocity imposed in this research is desirable, and the laboratory provides the means to study ways to obtain that type of flow. Integrating synthetic jets and microjets is an effort worth undertaking.

With active cooling techniques, there is always the risk of failure of forced convection components. Thus, it is important to perform a natural convection analysis to assess system performance if the active cooling device fails. Because of the high computer requirements for natural convection analyses of for these types of shrouded heat sinks, experimental testing would likely be the preferred approach to assessing the active cooling failure.

6.3 Conclusions

Due to technological and political developments, LED lighting is well on its way towards probable widespread implementation within the lighting industry. However, high power LEDs and LED arrays introduce severe thermal loadings for systems with heavily constrained footprints. Innovative and cost-efficient cooling methodologies are needed to help solid-state lighting persevere, especially in down-lighting applications.

Successful thermal engineering of shrouded heat sinks depends on system-level design, with simultaneous consideration of conduction thermal resistance, convective thermal resistance, convective surface area, aerodynamic characteristics, required energy input, and maintenance of optical properties. The goal should be to maximize the overall system conductance, but with consideration of the associated pumping power.

Thermodynamic design provides a significant opportunity to study fluid flow utilization and promote system cooling. This study exemplified that concept by reducing the overall thermal resistance from 0.40 K/W to 0.32 K/W for a constant pumping power of 5 W, despite a 13.3% loss in surface area. Also, by increasing the surface area, the thermal resistance was further reduced to 0.19 K/W.

Due to its superior efficiency, lifetime, reliability, and aesthetic light output, solid-state lighting has strong potential to capture significant market share of the illumination industry and reduce global energy consumption. But first, the major obstacles of high cost and high thermal loading need to be sufficiently dealt with. While economies of scale will significantly reduce cost, innovative engineering must be applied to prevent high device temperatures. Shrouded active cooling systems and radial fins have been investigated as possible thermal management methodologies for high power-density devices that have a limited footprint allocation. In this study, the optimization strategy that was detailed allows for a better understanding of the design space and trade-offs involved with the overall system performance. Results have shown that shrouded aluminum radial fin heat sinks can achieve substantially low thermal resistances and have much promise for the sufficient active air cooling of high power LED light applications.

REFRENCES

[1] "World consumption of primary energy by energy type and selected country groups, 1980-2006," U.S. Department of Energy, 2007; http://www.eia.doe.gov/iea/wec.html.

[2] "DOE report on global energy resources," April, 2005; http://www.nestenergysystems.com/globalenergyresources.htm.

[3] R. Smalley. "Our energy challenge," July 8, 2003; http://www.agci.org/library/presentations/about/presentation_details.php?recordID=16950.

[4] M. Loster. "Total primary energy supply: required land area," 2006; http://www.ez2c.de/ml/solar_land_area/.

[5] A. McKeown. "Strong growth in compact fluorescent bulbs reduces electricity demand," October 27, 2008; http://www.worldwatch.org/node/5920.

[6] "Annual energy review (AER)," Energy Information Administration, 2007; http://www.eia.doe.gov/emeu/aer/contents.html.

[7] B. K. Sovacool, *Energy and american society - thirteen myths*, Dordrecht: Springer, 2007.

[8] C. Morrison. "LEDs: the energy-saving alternative," 2009; http://www.osa.org/aboutosa/default.aspx.

[9] J. Farah. "Congress bans incandescent bulbs," December 19, 2007; http://www.worldnetdaily.com/news/article.asp?ARTICLE_ID=59298.

[10] "Energy indpendence and security act of 2007," 2007; http://energy.senate.gov/public/_files/HR6theEnergyIndependenceandSecurityActof2007.pdf.

[11] L. Gray. "Traditional lightbulbs banned by EU," October 10, 2008; http://www.telegraph.co.uk/news/worldnews/europe/3174452/Traditional-lightbulbs-banned-by-EU.html.

[12] P. Alvarado. "Ban against incandescent bulbs: Argentina joins," Feb. 2, 2009; http://www.treehugger.com/files/2009/01/argentina-bans-incandescent-light-bulbs.php.

[13] "EnLux lighting data specifications R-30 series," 2007; http://www.enluxled.com/datasheets/R-30%20F%20White1.pdf.

[14] "EnLux lighting data specifications DL series," 2008; http://www.enluxled.com/datasheets/DL_DataSheet2.pdf.

[15] "LR6 - The first viable LED downlight for commercial and residential applications," 2007; http://creelighting.com/LR6.htm.

[16] "LightingScience SoL R38 lamp," 2009; http://lsgc.com/downloads/R38_Sheet_FINAL_01-22-09-1.pdf.

[17] C. Bickford. "Typical examples of luminous efficacy," 2007; http://leddev.wordpress.com/2007/09/14/typical-examples-of-luminous-efficacy/.

[18] S. Haque, D. Steigerwald, S. Rudaz *et al.*, "Packaging challenges of high-power LEDs for solid state lighting," *Proceedings of SPIE - The International Society for Optical Engineering.* pp. 881-886.

[19] B. York, "The evolution of solid state lighting: from the laboratory to general lighting."

[20] R. Haitz, F. Kish, J. Tsao *et al.* "The case for a national research program on semiconductor lighting," March 30, 1999; http://lighting.sandia.gov/lightingdocs/hpsnl_long.pdf.

[21] J. Tsao. "Roadmap projects significant LED penetration of lighting market by 2010," May, 2003; http://lighting.sandia.gov/lightingdocs/TsaoJYLaserFocus200303.pdf.

[22] S. Kei. "Schematic diagrams of Light Emitting Diodes (LED)," April, 2006; http://commons.wikimedia.org/wiki/File:PnJunction-LED-E.PNG.

[23] X. Zou, X. Zheng, S. Jin *et al.*, "An integrated measurement system for LED thermal, optical and electrical characteristics," *Proceedings of SPIE - The International Society for Optical Engineering.* p. 66241.

[24] R. F. Babus'Haq, H. E. George, and P. W. O'Callaghan, “Thermal-analysis template,” *International Journal of Computer Applications in Technology,* vol. 5, no. 1, pp. 67-71, 1992.

[25] J. Arnold. "When the lights go out: LED failure modes and mechanisms," November, 2008; http://www.electrical-source.com/062008/articles/led_failure.pdf.

[26] Y. A. Cengel, and P. T. L. Zing, "Enhancement of Natural Convection Heat Transfer from Heat Sinks by Shrouding." pp. 451-457.

[27] P. Lall, *Influence of temperature on microelectronics and system reliability*, Boca Raton :: CRC Press, 1997.

[28] L. R. Trevisanello, M. Meneghini, G. Mura *et al.*, "Thermal stability analysis of high brightness LED during high temperature and electrical aging," *Proceedings of SPIE - The International Society for Optical Engineering.* p. 666913.

[29] S. Bowling, "LEDs thermal concerns in LED lighting," *ECN Electronic Component News,* vol. 52, no. 5, pp. 23-24, 2008.

[30] "Luxeon K2 reliability datasheet," 2007; http://www.philipslumileds.com/pdfs/RD06.pdf.

[31] M. Arik, C. Becker, S. Weaver *et al.*, "Thermal management of LEDs: package to system," *Proceedings of SPIE - The International Society for Optical Engineering.* pp. 64-75.

[32] R. Tummala, *Introduction to system-on-package; miniaturization of the entire system*, New York: McGraw-Hill, 2008.

[33] "Audi: light and design," 2008; http://www.carbodydesign.com/archive/2008/12/02-audi-light-design/.

[34] "LED architecture," 2008; http://www.arkitectrue.com/led-architecture/.

[35] A. McAteer. "Scottish lighting projects: Tidal Weir, Glen Lyon, Skye," 2005; http://www.glasgowarchitecture.co.uk/nva.htm.

[36] "LED high power street light," 2008; http://www.newsunshine.net/high_power_led_street_light.html.

[37] "Traffic signal upgrades," 2009; http://sites.google.com/site/greencentralarkansas/Home.

[38] "Paper with a backlight," 2008; http://gopaultech.com/blog/2008/10/paper-with-a-backlight/.

[39] M. Keferl. "Ear scope TV from Coden - clean your ears with your TV," 2007; http://www.cscoutjapan.com/en/index.php?s=earscope.

[40] "Energy savings calculator," 2008; http://www.creelighting.com/calculator.aspx.

[41] "Friendly's restaurant - Westfield, MA," 2007; http://www.creelighting.com/demos/Friendlys%20Before%20and%20After.pdf.

[42] S. Winder. "High power LED driving," 2006; http://www.emcomp.se/editor/upload/docs/High-Power-LED-Driving.pdf.

[43] J. Petroski, "Spacing of high-brightness LEDs on metal substrate PCB's for proper thermal performance," *Thermomechanical Phenomena in Electronic Systems - Proceedings of the Intersociety Conference.* pp. 507-514.

[44] R. Wilcoxon, and D. Cornelius, "Thermal management of an LED light engine for airborne applications," *Annual IEEE Semiconductor Thermal Measurement and Management Symposium.* pp. 178-185.

[45] M. Berger. "Nanotechnology to the rescue of overheating chips," 2007; http://www.nanowerk.com/spotlight/spotid=1762.php.

[46] "A new system-in-package solution from NeoPac Lighting is capable of dissipating 500 W/cm2 from high-power LED chips," October, 2005; http://www.ledsmagazine.com/features/2/6/3.

[47] J. Petroski, "Thermal challenges facing new generation light emitting diodes (LEDs) for lighting applications," *Proceedings of SPIE - The International Society for Optical Engineering.* pp. 215-222.

[48] S.-J. Hon, C. T. Kuo, T. P. Chen *et al.*, "High-power GaN LED chip with low thermal resistance," *Proceedings of SPIE - The International Society for Optical Engineering.* p. 689411.

[49] A. Christensen, and S. Graham, "Thermal effects in packaging high power light emitting diode arrays," *Applied Thermal Engineering,* vol. 29, no. 2-3, pp. 364-371, 2009.

[50] "Cree XLamp XR-E LED data sheet," 2008; http://www.cree.com/products/pdf/XLamp7090XR-E.pdf.

[51] M. K. Chyu, L. X. Wu, and J. Y. Murthy, "Forced convection heat transfer of a vertical shrouded fin array." p. 86.

[52] "Cree XLamp LED Thermal Management," March 2, 2009; http://www.cree.com/products/pdf/XLampThermalManagement.pdf.

[53] "Thermal Design Using Luxeon Power Light Sources," March 2, 2009; http://www.philipslumileds.com/pdfs/AB05.PDF.

[54] C. Ghiu, "Thermal SOP," Microsystems Packaging Research Center at Georgia Tech, 2008.

[55] F. P. Incropera et al., *Fundamentals of heat and mass transfer*, 6th ed., New York: Wiley & Sons, 2007.

[56] L. Kim, J. H. Choi, S. H. Jang *et al.*, "Thermal analysis of LED array system with heat pipe," *Thermochimica Acta,* vol. 455, no. 1-2, pp. 21-25, 2007.

[57] S. W. Chang, Y. J. Jan, and S. F. Chang, "Heat transfer of impinging jet-array over convex-dimpled surface," *International Journal of Heat and Mass Transfer,* vol. 49, no. 17-18, pp. 3045-59, 2006.

[58] Wei, Y.-J. Han, and Y. Luo, "High-efficiency AlGaInP LED with low thermal resistance fabricated by electroplating," *2007 International Nano-Optelectronics Workshop, iNOW.* pp. 184-185.

[59] A. Kosar, and Y. Peles, “Convective flow of refrigerant (R-123) across a bank of micro pin fins,” *International Journal of Heat and Mass Transfer,* vol. 49, no. 17-18, pp. 3142-3155, 2006.

[60] A. Kosar, and Y. Peles, “Thermal-hydraulic performance of MEMS-based pin fin heat sink,” *Journal of Heat Transfer,* vol. 128, no. 2, pp. 121-131, 2006.

[61] Z. Ma, X. Wang, D. Zhu *et al.*, "Thermal analysis and modeling of LED arrays integrated with an innovative liquid-cooling module," *2005 6th International Conference on Electronics Packaging Technology.* p. 1564677.

[62] A. G. Fedorov, and J. M. Meacham, "Evaporation-enhanced, dynamically-adaptive air (GAS)-cooled heat sink for thermal management of high heat dissipation devices," *2008 11th IEEE Intersociety Conference on Thermal and Thermomechanical Phenomena in Electronic Systems, I-THERM.* pp. 333-340.

[63] X. Luo, W. Chen, R. Sun *et al.*, “Experimental and numerical investigation of a microjet-based cooling system for high power LEDs,” *Heat Transfer Engineering,* vol. 29, no. 9, pp. 774-781, 2008.

[64] X. Luo, and S. Liu, “A microjet array cooling system for thermal management of high-brightness LEDs,” *IEEE Transactions on Advanced Packaging,* vol. 30, no. 3, pp. 475-484, 2007.

[65] S. Liu, J. Yang, Z. Gan *et al.*, “Structural optimization of a microjet based cooling system for high power LEDs,” *International Journal of Thermal Sciences,* vol. 47, no. 8, pp. 1086-1095, 2008.

[66] Z. M. Wang, K. Bao, L. P. Xu *et al.*, “Microfluidic cooling of semiconductor light emission diodes,” *Microelectronic Engineering,* vol. 84, no. 5-8, pp. 1223-1226, 2007.

[67] T. J. Lu, “Heat transfer efficiency of metal honeycombs,” *International Journal of Heat and Mass Transfer,* vol. 42, no. 11, pp. 2031-2040, 1999.

[68] S. Liu, Y. Zhang, and P. Liu, “New analytical model for heat transfer efficiency of metallic honeycomb structures,” *International Journal of Heat and Mass Transfer,* vol. 51, no. 25-26, pp. 6254-6258, 2008.

[69] C. Zweben, "Emerging low cost LED thermal management materials," *Proceedings of SPIE - The International Society for Optical Engineering.* pp. 194-206.

[70] Z. Kai, M. M. F. Yuen, D. G. W. Xiao *et al.*, "Directly synthesizing CNT-TIM on aluminum alloy heat sink for HB-LED thermal management," *Proceedings - Electronic Components and Technology Conference.* pp. 1659-1663.

[71] C.-J. Weng, "Advanced thermal enhancement and management of LED packages," *International Communications in Heat and Mass Transfer,* vol. 36, no. 3, pp. 245-248, 2009.

[72] R. A. Wirtz, R. Sohal, and H. Wang, "Thermal performance of pin-fin fan-sink assemblies," *Transactions of the ASME. Journal of Electronic Packaging,* vol. 119, no. 1, pp. 26-31, 1997.

[73] "Halo LED recessed lighting," 2009; http://www.haloltg.com/.

[74] S. Jang, and M. W. Shin, "Thermal analysis of LED arrays for automotive headlamp with a novel cooling system," *IEEE Transactions on Device and Materials Reliability,* vol. 8, no. 3, pp. 561-564, 2008.

[75] Y. Gu, A. Baker, and N. Narendran, "Investigation of thermal management technique in blue LED airport taxiway fixtures," *Proceedings of SPIE - The International Society for Optical Engineering.* p. 66690.

[76] S. Luger, "The thermal challenge - a physical contradiction," *LED professional Review*, no. 4, 2007.

[77] L.-L. Yuan, S. Liu, M.-X. Chen *et al.*, "Thermal analysis of high power LED array packaging with microchannel cooler," *Bandaoti Guangdian/Semiconductor Optoelectronics,* vol. 27, no. 6, pp. 712-716, 2006.

[78] S. Liu, T. Lin, X. Luo *et al.*, "A microjet array cooling system for thermal management of active radars and high-brightness LEDs," *Proceedings - Electronic Components and Technology Conference.* pp. 1634-1638.

[79] R. Mahalingam, N. Rumigny, and A. Glezer, "Thermal management using synthetic jet ejectors," *IEEE Transactions on Components and Packaging Technologies,* vol. 27, no. 3, pp. 439-444, 2004.

[80] D. Gerty, R. Mahalingam, and A. Glezer, "Design and characterization of a heat sink cooled by an integrated synthetic jet matrix," *Thermomechanical Phenomena in Electronic Systems -Proceedings of the Intersociety Conference.* pp. 356-360.

[81] D. W. Copeland, "Fundamental performance limits of heatsinks," *Journal of Electronic Packaging, Transactions of the ASME,* vol. 125, no. 2 SPEC, pp. 221-225, 2003.

[82] W. B. Krueger, and A. Bar-Cohen, "Optimal numerical design of forced convection heat sinks," *IEEE Transactions on Components and Packaging Technologies,* vol. 27, no. 2, pp. 417-425, 2004.

[83] D. J. De Kock, and J. A. Visser, "Optimal heat sink design using mathematical optimization," *Advances in Electronic Packaging.* pp. 337-347.

[84] T. Aihara, T. Ohara, and A. Sasago, “Overall performance of a heat sink-fan/pump unit and its optimum design,” *Heat Transfer - Japanese Research,* vol. 26, no. 8, pp. 515-527, 1997.

[85] A. Bejan, “Entropy generation minimization: The method and its applications,” *Strojniski Vestnik/Journal of Mechanical Engineering,* vol. 47, no. 8, pp. 345-355, 2001.

[86] A. Bejan, “Optimal internal structure of volumes cooled by single-phase forced and natural convection,” *Journal of Electronic Packaging, Transactions of the ASME,* vol. 125, no. 2 SPEC, pp. 200-207, 2003.

[87] J. G. Maveety, and H. H. Jung, “Heat transfer from square pin-fin heat sinks using air impingement cooling,” *IEEE Transactions on Components and Packaging Technologies,* vol. 25, no. 3, pp. 459-469, 2002.

[88] N. Zheng, and R. A. Wirtz, “Cylindrical pin-fin fan-sink heat transfer and pressure drop correlations,” *IEEE Transactions on Components and Packaging Technologies,* vol. 25, no. 1, pp. 15-22, 2002.

[89] Z. Duan, and Y. S. Muzychka, “Experimental investigation of heat transfer in impingement air cooled plate fin heat sinks,” *Journal of Electronic Packaging, Transactions of the ASME,* vol. 128, no. 4, pp. 412-418, 2006.

[90] Z. Duan, and Y. S. Muzychka, "Impingement air cooled plate fin heat sinks Part I - Pressure drop model," *Thermomechanical Phenomena in Electronic Systems - Proceedings of the Intersociety Conference.* pp. 429-435.

[91] E. M. Sparrow, and E. D. Larson, “Heat transfer from pin-fins situated in an oncoming longitudinal flow which turns to crossflow,” *International Journal of Heat and Mass Transfer,* vol. 25, no. 5, pp. 603-614, 1982.

[92] S. Y. Kim, and R. L. Webb, “Analysis of convective thermal resistance in ducted fan-heat sinks,” *IEEE Transactions on Components and Packaging Technologies,* vol. 29, no. 3, pp. 439-448, 2006.

[93] M. Saini, and R. L. Webb, “Heat rejection limits of air cooled plate fin heat sinks for computer cooling,” *IEEE Transactions on Components and Packaging Technologies,* vol. 26, no. 1, pp. 71-79, 2002.

[94] M. F. Holahan, "Fins, fans, and form: Volumetric limits to air-side heatsink performance," *Thermomechanical Phenomena in Electronic Systems - Proceedings of the Intersociety Conference.* pp. 564-570.

[95] S. Prstic, M. Iyengar, and A. Bar-Cohen, “Bypass effect in high performance heat sinks,” *Strojniski Vestnik/Journal of Mechanical Engineering,* vol. 47, no. 8, pp. 441-448, 2001.

[96] D. Copeland, “Optimization of parallel plate heatsinks for forced convection,” *Annual IEEE Semiconductor Thermal Measurement and Management Symposium*, pp. 266-272, 2000.

[97] R. F. Babus'Haq, S. D. Probert, and C. R. Taylor, “Heat-transfer effectiveness of shrouded, rectangular-fin arrays,” *Applied Energy,* vol. 46, no. 2, pp. 99-112, 1993.

[98] S. Naik, S. D. Probert, and I. G. Bryden, “Heat transfer characteristics of shrouded longitudinal ribs in turbulent forced convection,” *International Journal of Heat and Fluid Flow,* vol. 20, no. 4, pp. 374-384, 1999.

[99] S. El-Sayed, S. M. Mohamed, A. M. Abdel-latif *et al.*, “Investigation of turbulent heat transfer and fluid flow in longitudinal rectangular-fin arrays of different geometries and shrouded fin array,” *Experimental Thermal and Fluid Science,* vol. 26, no. 8, pp. 879-900, 2002.

[100] W. A. Khan, J. R. Culham, and M. M. Yovanovich, “Performance of shrouded pin-fin heat sinks for electronic cooling,” *Journal of Thermophysics and Heat Transfer,* vol. 20, no. 3, pp. 408-414, 2006.

[101] K. Azar, and C. D. Mandrone, “Effect of pin fin density of the thermal performance of unshrouded pin fin heat sinks,” *Transactions of the ASME. Journal of Electronic Packaging,* vol. 116, no. 4, pp. 306-9, 1994.

[102] R. F. Babus'Hag, K. Akintunde, and S. D. Probert, “Thermal performance of a pin-fin assembly,” *International Journal of Heat and Fluid Flow,* vol. 16, no. 1, pp. 50-55, 1995.

[103] M. A. Tahat, R. F. Babus'Haq, and S. D. Probert, “Forced steady-state convections from pin-fin arrays,” *Applied Energy,* vol. 48, no. 4, pp. 335-351, 1994.

[104] K. A. Moores, and Y. K. Joshi, “Effect of tip clearance on the thermal and hydrodynamic performance of a shrouded pin fin array,” *Journal of Heat Transfer,* vol. 125, no. 6, pp. 999-1006, 2003.

[105] H. C. Ryu, D. Kim, and S. J. Kim, "Experimental analysis of shrouded pin fin heat sinks for electronic equipment cooling," *Thermomechanical Phenomena in Electronic Systems -Proceedings of the Intersociety Conference.* pp. 261-266.

[106] A. Dvinsky, A. Bar-Cohen, and M. Strelets, "Thermofluid analysis of staggered and inline pin fin heat sinks," *ITHERM 2000. The Seventh Intersociety*

Conference on Thermal and Thermomechanical Phenomena in Electronic Systems (Cat. No.00CH37069). pp. 157-64.

[107] K. C. Toh, K. C. Leong, T. G. Lim *et al.*, “Forced convection heat transfer from vertically stacked fin arrays with a shrouding wall,” *International Communications in Heat and Mass Transfer,* vol. 19, no. 3, pp. 373-84, 1992.

[108] H. G. Yalcin, S. Baskaya, and M. Sivrioglu, “Numerical analysis of natural convection heat transfer from rectangular shrouded fin arrays on a horizontal surface,” *International Communications in Heat and Mass Transfer,* vol. 35, no. 3, pp. 299-311, 2008.

[109] Y. A. Cengel, and T. H. Ngai, “Cooling of vertical shrouded-fin arrays of rectangular profile by natural convection. An experimental study,” *Heat Transfer Engineering,* vol. 12, no. 4, pp. 27-39, 1991.

[110] S. S. Bahga, A. Bhattacharya, and R. L. Mahajan, "Numerical modeling of buoyancy induced convection in finned heat sinks in presence of unheated and heated shrouds," *American Society of Mechanical Engineers, Heat Transfer Division, (Publication) HTD.* pp. 725-731.

[111] R. L. Lohe, A. Bhattacharya, and R. L. Mahajan, "Longitudinal finned heat sinks with unheated and heated shrouds in buoyancy induced convection," *Advances in Electronic Packaging.* pp. 763-770.

[112] E. M. Sparrow, and S. B. Vemuri, “Orientation effects on natural convection/radiation heat transfer from pin-fin arrays,” *International Journal of Heat and Mass Transfer,* vol. 29, no. 3, pp. 359-68, 1986.

[113] W. W. Thrasher, T. S. Fisher, and K. E. Torrance, “Experiments on chimney-enhanced free convection from pin-fin heat sinks,” *Journal of Electronic Packaging, Transactions of the ASME,* vol. 122, no. 4, pp. 350-355, 2000.

[114] K. Yazawa, "Natural convection enhancement of channel array in conjunction with wall surface," *Thermomechanical Phenomena in Electronic Systems - Proceedings of the Intersociety Conference.* pp. 128-133.

[115] G. Guglielmini, G. Tanda, and E. Nannei, “Effect of shrouding on air natural-convection heat transfer from staggered vertical fins,” *Experimental Heat Transfer,* vol. 2, no. 2, pp. 105-112, 1989.

[116] O. Manca, S. Nardini, and V. Naso, “Effect on natural convection of the distance between an inclined discretely heated plate and a parallel shroud below,” *Journal of Heat Transfer,* vol. 124, no. 3, pp. 441-450, 2002.

[117] C. Hui, Y. Ma, and K. Kitamura, "Natural convective fluid flow and heat transfer over upward-facing horizontal and slightly inclined plate, shrouded by a parallel

cover plate," *Proceedings of the 1st International Conference on Engineering Thermophysics (ICET '99).* pp. 86-93.

[118] Z. Jian-Hui, and Y. Chun-Xin, “Design and simulation of the CPU fan and heat sinks,” *IEEE Transactions on Components and Packaging Technologies,* vol. 31, no. 4, pp. 890-903, 2008.

[119] B. N. Taufiq, H. H. Masjuki, T. M. I. Mahlia *et al.*, “Second law analysis for optimal thermal design of radial fin geometry by convection,” *Applied Thermal Engineering,* vol. 27, no. 8-9, pp. 1363-70, 2007.

[120] M. Almogbel, and A. Bejan, “Cylindrical trees of pin fins,” *International Journal of Heat and Mass Transfer,* vol. 43, no. 23, pp. 4285-4297, 2000.

[121] P. J. Heggs, and T. H. Ooi, “Design charts for radial rectangular fins in terms of performance ratio and maximum effectiveness,” *Applied Thermal Engineering,* vol. 24, no. 8-9, pp. 1341-1351, 2004.

[122] P. Razelos, S. Das, and R. N. Krikkis, “Enhanced boiling heat transfer using radial fins,” *Heat and Mass Transfer/Waerme- und Stoffuebertragung,* vol. 44, no. 6, pp. 705-715, 2008.

[123] P. K. Papadopoulos, and P. M. Hatzikonstantinou, “Numerical study of laminar fluid flow in a curved elliptic duct with internal fins,” *International Journal of Heat and Fluid Flow,* vol. 29, no. 2, pp. 540-4, 2008.

[124] M. Rahnama, and M. Farhadi, “Effect of radial fins on two-dimensional turbulent natural convection in a horizontal annulus,” *International Journal of Thermal Sciences,* vol. 43, no. 3, pp. 255-264, 2004.

[125] T. J. Heindel, A. Campo, S. Ramadhyani *et al.*, “Measurements of heat transfer coefficients between turbulent liquid jets and a radially finned heated disk placed at the bottom of an open vertical circular cavity,” *Heat and Mass Transfer/Waerme- und Stoffuebertragung,* vol. 38, no. 7-8, pp. 577-587, 2002.

[126] B. Dehoff, C.-S. Wang, and D. Fast, "Thermal optimization of a radial folded fin heat sink for desktop computer applications," *Thermomechanical Phenomena in Electronic Systems -Proceedings of the Intersociety Conference.* pp. 341-344.

[127] S. W. Chang, K. F. Chiang, Y. Zheng *et al.*, “Detailed heat transfer measurements of curved fin channels,” *Heat Transfer Engineering,* vol. 29, no. 10, pp. 849-863, 2008.

[128] M. Wilcox. "Helping LEDs keep their cool," November, 2008; http://www.photonics.com/Content/ReadArticle.aspx?ArticleID=35531.

[129] T. M. Crittenden, and A. Glezer, “A high-speed, compressible synthetic jet,” *Physics of Fluids,* vol. 18, no. 1, 2006.

[130] R. L. Mahalingam, S. Heffington, L. Jones *et al.* "Synthetic jets for forced air cooling of electronics," May, 2007; http://www.electronics-cooling.com/articles/2007/may/a1/.

[131] "Nuventix chip/CPU spot cooling, high power LED down light module heat spreading, CPU spot coolers, active thermal management," 2009; http://www.nuventix.com/products/#6.

[132] H. Jonsson, and B. Palm, "Experimental comparison of different heat sink designs for cooling of electronics," *American Society of Mechanical Engineers, Heat Transfer Division, (Publication) HTD.* pp. 27-34.

[133] J. E. Pope, *Rules of thumb for mechanical engineers: a manual of quick, accurate solutions to everyday mechanical engineering problems*, Houston, TX: Gulf Pub. Co., 1997.

[134] "Aavid thermalloy," September 22, 2008; http://www.aavidthermalloy.com/cgi-bin/exdisp_led.pl?Pnum=76620&therm=2.06592946910361&airflow=57.2&ExLength=4.000&LengthUnits=in.

[135] "DC brushless fan," March, 2008; http://www.tranyoung.com.tw/PDF/61-120x120x25mm%20Series.pdf.

[136] "The #1 selling product in the process integration and design optimization market," 2009; http://www.engineous.com/iSIGHT.cfm.